Image processing in vascular computed tomography

Gratama van Andel, H.A.F.

[Link to publication](#)

Citation for published version (APA):
Gratama van Andel, H. A. F. (2010). *Image processing in vascular computed tomography*. [Thesis, fully internal, Universiteit van Amsterdam].

Image Processing
in Vascular Computed
Tomography

Hugo A.F. Gratama van Andel

Image Processing
in Vascular Computed
Tomography

Image Processing in Vascular Computed Tomography

ACADEMISCH PROEFSCHRIFT

ter verkrijging van de graad van doctor
aan de Universiteit van Amsterdam
op gezag van de Rector Magnificus
prof. dr. D.C. van den Boom
ten overstaan van een door het college voor
promoties ingestelde commissie,
in het openbaar te verdedigen in de Agnietenkapel
op woensdag 3 februari 2010, te 14.00 uur

door
Hugo Arthur Freseman Gratama van Andel
geboren te Boskoop

PROMOTIECOMMISSIE

Promotores: *Prof. dr. ir. C.A. Grimbergen*
                  Prof. dr. G.J. den Heeten

Co-promotores: *Dr. H.W. Venema*
                  Dr. ir. G.J. Streekstra

Overige leden: *Prof. dr. W.J. Niessen*
                  Prof. dr. ir. L.J. van Vliet
                  Prof. dr. M.B van Herk
                  Prof. dr. J.A. Reekers
                  Dr. ir. M. van Straten
                  Dr. F.M. Vos

Faculteit der Geneeskunde

CONTENTS

1
General Introduction

I. GENERAL INTRODUCTION

I. ANGIOGRAPHIC IMAGING

Angiography is the term that is used for techniques that visualize the inside, or lumen, of blood vessels. The word originates from the Greek words αγγειον (aggeion), meaning "vessel" or "bucket", and γραφειν (graphein), meaning "to write" or "to record". An image of the blood vessels of a patient, an angiogram, is traditionally made by injecting a radio-opaque contrast agent into a blood vessel and making projection images using X-rays. In 1927 the Portuguese physician and neurologist Egaz Moniz made the first cerebral angiogram of a living patient.[1,2] The technique enabled physicians from that day on, to base their diagnosis on imaging instead of surgery for several kinds of neurological disorders, such as aneurysms, arteriovenous malformations, and tumors.

Although nowadays a number of other imaging techniques have been developed to visualize blood vessels (see Fig. 1), conventional angiography is still daily practice. There has of course been improvement in patient safety and in image quality over the years, but the basic principle of the technique has remained the same: Iodine contrast is injected via a catheter into the artery to be depicted, and projection images are made. The focus of conventional angiography, however, has shifted from diagnosis to interventional procedures, where the direct feedback and the dynamic aspect of the technique play an important role.[3,4] In the diagnostic process conventional angiography has been gradually replaced by other techniques.

With conventional angiography evaluation of blood vessels is limited because of the difficulty of interpreting the three dimensional (3D) reality from two dimensional (2D) images, and overprojection of different vessels. Three dimensional rotational angiography was introduced to solve this problem.[5] However, with both techniques a patient is exposed to a small but not negligible risk of neurological complications [6,7] because of the need for catheterization.

Computed tomography angiography (CTA) and magnetic resonance angiography (MRA) are 3D imaging techniques that nowadays are applied often for imaging of blood vessels. Both techniques are less invasive than conventional angiography as there is no need for catherization of the patient. For a number

of diagnostic questions it has been shown that these techniques can replace conventional angiography.[8,9] MRA has the advantage over CTA that it does not involve the use of X-rays. Disadvantages of MRA are, however, its cost, its limited availability and long acquisition times.[10,11] CTA examinations are considered the primary choice for a number of clinical questions. This thesis will concentrate on CT angiography of the region of head and neck.
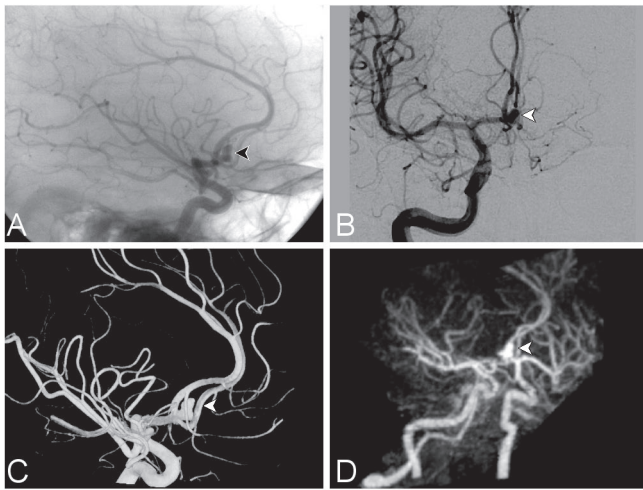
Fig. 1
Four different techniques used to depict an intracranial aneurysm (arrowhead) in the posterior communicating artery of one patient;
A) an angiogram;
B) a digital subtraction angiogram;
C) a volume rendering of three dimensional rotational angiogram and
D) a maximum intensity projection of computed tomography angiography examination with bone removal.

II. CT ANGIOGRAPHY OF THE HEAD & NECK REGION

In 1972 Hounsfield introduced the first head computed tomography (CT) scanner (EMI Mark I, EMI Ltd., London, United Kingdom) that could make cross-sectional images of patients.[12,13] Since then there has been an enormous development in CT technology, for CT angiography the main step in the evolution has been the development of spiral CT with a slip-ring. Before this development, CT angiography had already been introduced but the scan length was limited to approximately 3 cm.[14-16] CT acquisition times were long as cable connections to the gantry prevented continuous rotation. The gantry had to be accelerated in one direction, stopped after one rotation and then accelerated in the opposite direction. As the time that vessels are enhanced after administration of a contrast agent is limited (20-30 s) only a small part of vessels could be visualized. Due to the slip-ring technology it became possible to mount the high-frequency power supplies

on the rotating part of the gantry without the need for a cable connection from the rotating part to the stationary part and continuous rotation became possible. This made conventional acquisitions (slice for slice) faster but it also made a new technique, spiral (or helical) acquisition, possible. In spiral CT the continuous rotation of the gantry is combined with simultaneous patient translation through the gantry which enables fast volumetric imaging of organs without discontinuities.[17] The concept of spiral CT was introduced by W. Kalender in 1989, soon after the slip-ring CT scanners became available.[18]

After the introduction of spiral CT, several early reports on clinical applications of spiral CT dealt with CT Angiography.[19-23] For CTA the spiral CT technique was important as it made it possible to acquire the data for the reconstruction of three dimensional images in the short time (20-30 s) that the injected contrast was present in the arteries or veins (see Fig. 2). Moreover, in this short time a patient could hold his or her breath which largely reduces motion artifacts.
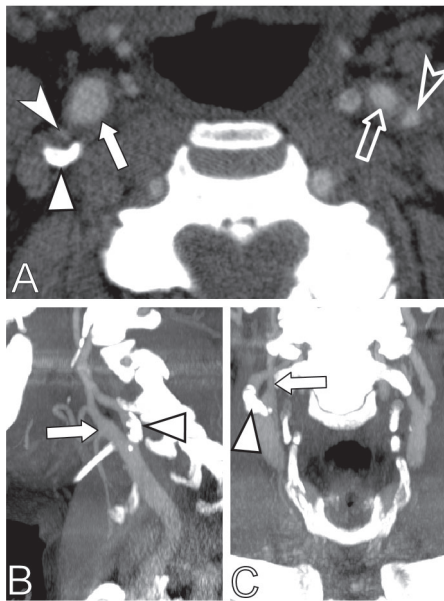
Fig. 2
Images from a CTA examination of the head and neck region of a patient with a stenosis of the right internal carotid artery.
A) A region of interest of an axial image at the site of the most severe stenosis. The stenosed right internal carotid artery (arrowhead), a calcified atherosclerotic plaque (triangle) and the external carotid artery are depicted. The left internal carotid artery (open arrowhead) and the left external carotid artery (open arrow) are also depicted.
B) and C) show a sagittal and coronal maximum intensity projection of a thin slab (20 mm) around the right carotid artery.

Because of the high contrast-to-noise ratio of CT imaging compared with conventional angiography, the contrast agent in CTA can be injected intra-venously instead of arterially, which is less invasive. The contrast agent is normally injected

in an antecubital vein and it passes the heart and the pulmonary circulation before it enters the systemic circulation for the first passage. The time between the start of the injection and the moment that maximal enhancement is reached of the vessels of interest (in the order of 12-27 s for the carotid arteries)[24] will depend on the injection protocol, but also on patient specific factors as weight and cardiac function.[25] To reduce the risk of a scan with sub-optimal enhancement a test-bolus injection[26-28] or bolus-tracking techniques[29-31] can be used.

A CT venography (CTV) scan is made if one is interested in the venous system instead of the arterial system (see Fig. 3). The main difference between a CTA and a CTV scan is the timing.[32] As the contrast will first pass through the arterial system, then through the capillaries and then through the veins and sinuses, the optimal time delay between injection and starting of the scan of a CTV scan will be longer.

To prolong the time that vessels are enhanced, both CTA and CTV scans are made in the main direction of the blood flow; in case of a scan of the head this will be from caudal to cranial for a CTA scan and in the opposite direction for a CTV scan.
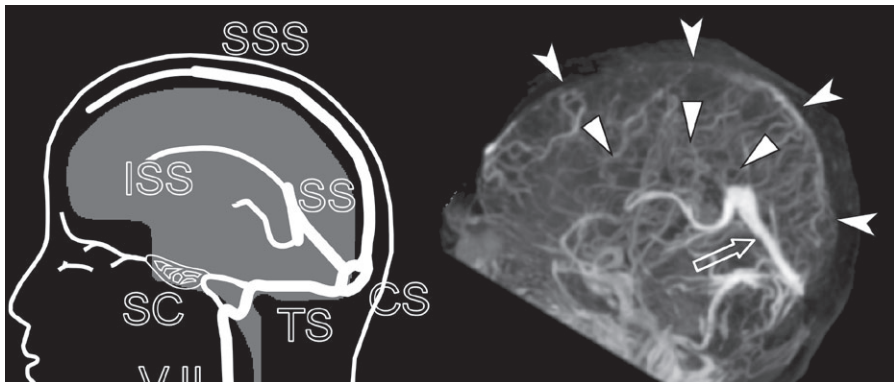
Fig. 3
A) A diagram displaying the larger veins and sinuses in the head & neck region that should be visible in a patient without thrombosis. SSS: superior sagittal sinus; ISS: inferior sagittal sinus; SS: straight sinus; SC: sinus cavernous; TS: transverse sinus; CS: confluence of sinuses and VJI: internal jugular vein.
B) Sagittal maximum intensity projection of a CTV examination (after bone removal) of a patient with a venous thrombosis. No or minimal enhancement is present in the superior sagittal sinus (SSS, arrowheads) and the sagittal sinus inferior (SSI, triangles), while the straight sinus (open arrow) is clearly visible.

An imaging technique closely related to CTA is CT perfusion (CTP) imaging.[33] A CTP examination consists of a time-series of CT scans, during and after injection of a contrast bolus. With post-processing of the images different

functional parameters such as the cerebral blood volume, cerebral blood flow and mean transit time can be determined.[34-36] These parameters enable physicians to distinguish in the brain of a patient with stroke between areas that can benefit from treatment and areas that will not (see Fig. 4). This can be of help in making decisions on treatment of patients.
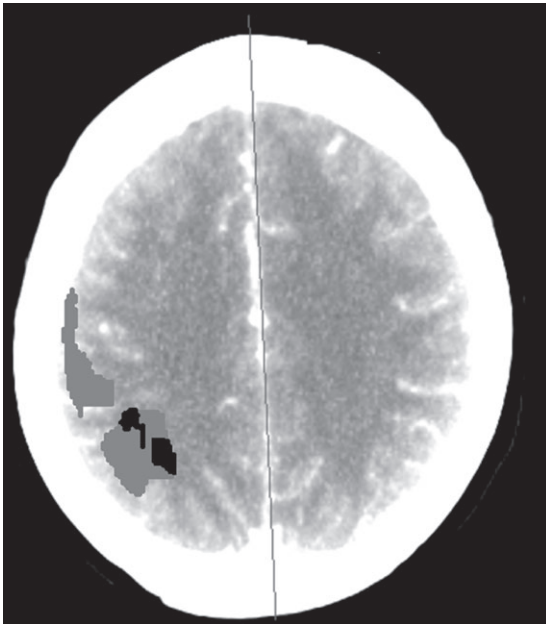
Fig. 4
The result of an analysis of a brain perfusion scan of a patient suffering from a stroke. Areas with a reduced perfusion are indicated with a colour, areas in black do not longer show an active regulation of the perfusion while the grey areas still do have an active regulation and could benefit from treatment.

III. OUTLINE OF THE THESIS

In this thesis a number of topics on image processing of CTA images are treated. The first topic is the visualization of blood vessels in CTA. In chapter 2 a method is described that aids visualization of blood vessels by removing image voxels corresponding to bone. The method described is a modification of a method described previously. Chapter 3 and 4 deal with clinical applications of the original method. The second topic is on quantification of the size of blood vessels in CTA images. Two aspects are treated, the definition of a center lumen line in chapter 5 and the accurate and precise measurements of the diameter of a vessel in chapter 6. In chapter 7 the feasibility is investigated to obtain both CTA images and CTP images from one single examination.

III.A. BONE REMOVAL

A CTA scan made with a modern scanner consists of hundreds of images. Examination of all vessels in all cross-sectional images is a cumbersome task.[37] To facilitate the review of the examination one often tries to get a better overview using images made with three dimensional (3D) visualization techniques such as maximum intensity projection (MIP) or volume rendering (VR).[38] In this way, a physician can examine a whole vascular tree faster for pathologies, will have a better insight in its 3D structure and has to consider only the relevant cross-sectional images.

With 3D visualization techniques, two dimensional (2D) projection images are created from different directions from a 3D volume. MIPs can be used straightforward for the visualization of vessels if they are surrounded by soft tissue. In case bone is present it will hamper the visualization of the vessels in MIP images as the CT value of bone will be higher than that of the enhanced vessels. As a result the bone will overlay the vessels in the MIP images. In VR images a similar problem exists. In this case, the overlap in the ranges of intensity values of vessels and bone makes it impossible to visualize the vessels separately. To make vessels visible in MIP or VR images in areas with bone, like the head and neck region, bone has to be removed from the CTA images.[21,23,39]

Bone removal can be performed manually. Almost all commercially available 3D viewing software supports removal of regions from the volume of interest interactively by drawing contours with a mouse. This manual bone removal, however, is very time consuming and almost impossible in areas like the skull and spine, where vessels are situated close to the bone or are surrounded by bone.[39,40]

Bone removal can also be performed automatically using a masking method, matched mask bone elimination (MMBE).[41,42] This method uses an additional low dose scan in which vessels are not enhanced. From this scan a bone mask is made of all high density voxels. As the bone mask is made from a different scan it can not be used directly to remove bone in the enhanced image because of inevitable patient movements between the two scans. Therefore the two scans are first registered. Subsequently all voxels corresponding to bone in the CTA images are given a low value and vessels can then be visualized without the disturbing effect of bone in VR- or MIP images.

A problem that arises when masking bone in a CT image, is that a thin strip

of adjacent tissue is masked as well, due to unsharpness of the images and the thickness of the imaged slices. When vessels are in close proximity of bone, their integrity is affected as they are eroded by the mask. This problem can in principle be alleviated by using sharper images, because in that case the mask will be more accurate and less erosion of the vessels will take place. Sharper images can be obtained by using sharper reconstruction filters and thinner slices. A problem when using sharper images is that the noise in the images increases as well, which may affect their diagnostic quality. In practice therefore for each protocol a trade-off between sharpness and noise is made to make the images optimal for the diagnostic task at hand. With the following approach in principle both a well defined mask and a clinically acceptable noise level can be obtained: 1) make reconstructions of the CT scan with a higher resolution (and more noise), 2) mask the bone voxels in these higher resolution images (with less erosion of vessels) and 3) restore the desired noise level (by reducing the resolution). A method that follows this approach, multiscale MMBE, is presented in chapter 2 and the results are compared with the original MMBE method.

When the MMBE method was introduced, results were presented of only a limited number of patients. The quality of bone removal was not evaluated in a large group of patients and the diagnostic value of CTA images in combination with MMBE in the diagnostic process was also not investigated. These points are addressed in chapters 3 and 4.

In chapter 3 the diagnostic accuracy of CTA with MMBE is determined for detection of intracranial aneurysms in a large patient population with clinically suspected subarachnoid hemorrhage using digital subtraction angiography and three dimensional rotational angiography as reference standards.

In chapter 4 the interobserver variability in the detection of cerebral venous thrombosis using CT venography with MMBE was investigated and the quality of a fully automatic bone removal was evaluated.

III.B. MEASUREMENTS OF THE DEGREE OF STENOSIS

CT angiography can be used to determine the degree of stenosis in patients that are suspected of carotid artery occlusive disease. These patients often suffer from transient ischemic attacks (TIAs), a neurologic dysfunction that persists for less

than 24 hours. The most common cause of a TIA is an embolus that occludes an artery in the brain. This embolus most frequently arises from an atherosclerotic plaque, that causes a stenosis of one of the carotid arteries. Treatment of the stenosis by endarterectomy (surgical removal) or endovascular stent placement can reduce the risk on reoccurrence of a TIA. Whether a patient will benefit from treatment, depends on the severity of this stenosis.[43-46]

For quantification of carotid artery stenosis the NASCET criteria are often used. According to these criteria the severity of a stenosis is defined as the percentage of the diameter that is obstructed. This can be calculated by measuring the vessel diameter at the place of the stenosis and a vessel diameter at a distal reference site in the same vessel. In large trials it has been shown that patients with stenosis percentage of 70 % and higher benefit from surgical treatment.[47] With lower stenoses percentages the benefit of this treatment does not outweigh the risks involved. Therefore accurate and precise diameter measurements are important.

Digital subtraction angiography (DSA) has historically been the golden standard to assess the severity of stenosis, but it has been shown that it can be replaced by less invasive three dimensional techniques such as MRA and/or CTA.[8,9] CTA is often used for the quantification of carotid stenosis as it is relatively cheap and widely available in comparison to MRA.[10,11]

To measure the diameter of a blood vessel two steps have to be taken: 1) the center lumen line (CLL) has to defined, as measurements have to be performed perpendicular to the vessel and 2) the size of the cross-section of the lumen of the vessel has to be measured. If measurements are performed manually, both steps give rise to inter- and intra-observer variations. Systematic errors may be present as well. As the stenosis percentage is crucial for the decision on treatment there is a potential benefit in automated methods for stenosis quantification as these may reduce these variations and systematic errors.

Many different structures and vessels are present in CTA images and with automatic methods it is often difficult to find which vessel is the one of interest. To overcome this problem, most methods are implemented in a semi-automatic way. An observer places two or more seedpoints in the carotid artery of interest, and next the automated method will try to determine the center lumen line of that specific artery. This automated approach greatly reduces the observer dependency as the variation between observers depends for the largest part on the definition of

where the center of a vessel is annotated and not on which specific carotid artery is the one of interest.

Techniques for automated path tracing typically run into problems when dealing with vessels with abnormalities such as stenoses, aneurysms, and calcifications but also when dealing with bifurcations, vessels of high curvature, and other nearby vessels and bone.[48-50] A promising method was published for the tracing of neurons in microscopic images.[51] This method employed the use of an improved filter for recognition of tubular structures and seemed to be a valid option for the tracing of vessels in CTA images as well. In chapter 5 a method is presented based upon this filter and the resulting CLL tracings are compared with manual tracings of multiple observers and with tracings of another automated method.

When a center lumen line has been defined the measurement of the diameter of the cross-section has to be performed. In this task automated methods still encounter a lot of problems. They show a decreasing accuracy and precision in diameter measurements of smaller vessels,[52,53] are influenced by the convolution kernel used for the reconstructed images,[53] are dependent on the amount of contrast enhancement[54] and tend to have problems with the presence of calcifications.[55,56]

Underlying most of these problems is the blurring of the images, which is inherent in CT imaging. This blurring causes conventional methods that use the full width at half maximum criterion,[57] or the second order derivative zero crossings criterion,[58] to inaccurately locate the vessel boundary leading to a bias in the diameter estimate.[59] One can try to remove this bias by the use of a correction procedure or by a model-based approach.[60-65] In both approaches explicit allowance is made for the blurring of structures in the image. In principle this allows for elimination of the bias in diameter estimates of structures. Until now all methods are applicable only to vessels with circular cross-sections. The advantage of a model-based approach is that it can be readily extended to more general vessel geometries.

With this in mind, a model-based approach for diameter measurements of vessels with a stenosis in CTA images was desired and implemented. To allow for non-circular shapes of the cross-section of vessels, Fourier descriptors were used.[66,67] When calcifications are contiguous to the lumen of the vessel, both the vessel and the calcifications were modeled in an attempt to improve the diameter estimates of the vessel. This method is presented and evaluated in chapter 6.

III.C. CTA & CTP COMBINED

In clinical practice, patients who receive a CT perfusion examination almost always also receive a CTA examination of the cerebral arteries at the same time.[68,69] The similarity of the two examinations led to idea that CTA images might be obtained from CTP image series. In such a scenario one of the examinations could be eliminated, decreasing radiation dose and contrast medium load to the patient.

The main difference between CTP and CTA is the dynamic aspect of a CTP scan and, until recently, the limited region of the brain that was covered in a CTP examination. With the ongoing development of CT-scanner technology coverage has increased while the slice thickness has decreased.[70-73] This opens the possibility to obtain anatomical images from the cerebral vasculature from the same scan that is used to obtain the functional CTP images.

Because of the large number of images of a CTP examination each single image is acquired with a lower mAs value than in a CTA examination to limit the total dose of the CTP scan. Therefore each single CTP image, even at the time of maximal enhancement, has a contrast-to-noise ratio (CNR) that is too low to be useful as a CTA image. In chapter 7 a method for weighted averaging of the whole sequence of CTP images is described in an attempt to create images with sufficient CNR. The resulting images are compared to CTA images.

REFERENCES

1   E. Moniz, "[Subsidies for the history of angiography.]," Medicina contemporanea (Lisbon, Portugal) 73 (7), 329-346 (1955).

2   E. Moniz and M. Guerra, "[Angiographical symptomatology of aneurysms, varices and angiomas of the brain.]," Giornale di psichiatria e di neuropatologia 81 (4), 866-870 (1953).

3   Josef Rösch, Frederick S. Keller and John A. Kaufman, "The Birth, Early Years, and Future of Interventional Radiology," Journal of Vascular and Interventional Radiology 14 (7), 841-853 (2003).

4   Dheeraj Gandhi, Sudhir Kathuria, Sameer A. Ansari, Gaurang Shah and Joseph J. Gemmete, "State of the Art Head and Neck Imaging for the Endovascular Specialist," Neuroimaging Clinics of North America 19 (2), 133-147 (2009).

5   R. Fahrig, A. J. Fox, S. Lownie and D. W. Holdsworth, (1997), Vol. 18, pp. 1507-1514.

6   GJ Hankey, CP Warlow and RJ Sellar, "Cerebral angiographic risk in mild cerebrovascular disease," Stroke 21 (2), 209-222 (1990).

7   K. N. Davies and P. R. Humphrey, "Complications of cerebral angiography in patients with symptomatic carotid territory ischaemia screened by carotid ultrasound," Journal of Neurology, Neurosurgery and Psychiatry 56 (9), 967-972 (1993).

8   M. J. Koelemay, P. J. Nederkoorn, J. B. Reitsma and C. B. Majoie, "Systematic review of computed tomographic angiography for assessment of carotid artery disease," Stroke 35 (10), 2306-2312 (2004).

9   S. M. Debrey, H. Yu, J. K. Lynch, K. O. Lovblad, V. L. Wright, S. J. Janket and A. E. Baird, "Diagnostic accuracy of magnetic resonance angiography for internal carotid artery disease: a systematic review and meta-analysis," Stroke 39 (8), 2237-2248 (2008).

10 I. Kane, W. N. Whiteley, P. A. Sandercock and J. M. Wardlaw, "Availability of CT and MR for assessing patients with acute stroke," Cerebrovascular diseases (Basel, Switzerland) 25 (4), 375-377 (2008).

11 C. L. Sistrom and N. L. McKay, "Costs, charges, and revenues for hospital diagnostic imaging procedures: differences by modality and hospital characteristics," J Am Coll Radiol 2 (6), 511-519 (2005).

12 J. Ambrose and G. Hounsfield, "Computerized transverse axial tomography," The British journal of radiology 46 (542), 148-149 (1973).

13 G. N. Hounsfield, "Computerized transverse axial scanning (tomography). 1. Description of system," The British journal of radiology 46 (552), 1016-1022 (1973).

14 M. Brant-Zawadzki and R. B. Jeffrey, Jr., "CT with image reformation for noninvasive screening of the carotid bifurcation: early experience," AJNR Am J Neuroradiol 3 (4), 395-400 (1982).

15 E. R. Heinz, J. Fuchs, D. Osborne, B. Drayer, A. Yeates, H. Fuchs and S. Pizer, "Examination of the extracranial carotid bifurcation by thin-section dynamic CT: direct visualization of intimal atheroma in man (Part 2)," AJNR Am J Neuroradiol 5 (4), 361-366 (1984).

16 E. R. Heinz, S. M. Pizer, H. Fuchs, E. K. Fram, P. Burger, B. P. Drayer and D. R. Osborne, "Examination of the extracranial carotid bifurcation by thin-section dynamic CT: direct visualization of intimal atheroma in man (Part 1)," AJNR Am J Neuroradiol 5 (4), 355-359 (1984).

17 W. A. Kalender, W. Seissler, E. Klotz and P. Vock, "Spiral volumetric CT with single-breath-hold technique, continuous transport, and continuous scanner rotation," Radiology 176 (1), 181-183 (1990).

18   W. A. Kalender, W. Seissler and P. Vock, "Single-breath-hold spiral volumetric CT by continuous patient translation and scanner rotation," Radiology 173 (P), 414 (1989).

19   P. Costello, D. E. Dupuy, C. P. Ecker and R. Tello, "Spiral CT of the thorax with reduced volume of contrast material: a comparative study," Radiology 183 (3), 663-666 (1992).

20   P. Costello, C. P. Ecker, R. Tello and G. G. Hartnell, "Assessment of the thoracic aorta by spiral CT," Ajr 158 (5), 1127-1130 (1992).

21   S. Napel, M. P. Marks, G. D. Rubin, M. D. Dake, C. H. McDonnell, S. M. Song, D. R. Enzmann and R. B. Jeffrey, Jr., "CT angiography with spiral CT and maximum intensity projection," Radiology 185 (2), 607-610 (1992).

22   G. D. Rubin, S. Napel, M. D. Dake, P. J. Walker, C. H. McDonnell, M. P. Marks and R. B. Jeffrey, Jr., "Spiral CT creates 3-D neuro, body angiograms," Diagnostic imaging 14 (8), 66-74 (1992).

23   R. B. Schwartz, K. M. Jones, D. M. Chernoff, S. K. Mukherji, R. Khorasani, H. M. Tice, R. Kikinis, S. M. Hooton et al., "Common carotid artery bifurcation: evaluation with spiral CT. Work in progress," Radiology 185 (2), 513-519 (1992).

24   C. de Monye, F. Cademartiri, T. T. de Weert, D. A. Siepman, D. W. Dippel and A. van Der Lugt, "Sixteen-detector row CT angiography of carotid arteries: comparison of different volumes of contrast material with and without a bolus chaser," Radiology 237 (2), 555-562 (2005).

25   F. Cademartiri, A. van der Lugt, G. Luccichenti, P. Pavone and G. P. Krestin, "Parameters affecting bolus geometry in CTA: a review," Journal of computer assisted tomography 26 (4), 598-607 (2002).

26   L. van Hoe, G. Marchal, A. L. Baert, S. Gryspeerdt and L. Mertens, "Determination of scan delay time in spiral CT-angiography: utility of a test bolus injection," Journal of computer assisted tomography 19 (2), 216-220 (1995).

27   R. Kaatee, M. S. Van Leeuwen, E. E. De Lange, J. E. Wilting, F. J. Beek, J. J. Beutler and W. P. Mali, "Spiral CT angiography of the renal arteries: should a scan delay based on a test bolus injection or a fixed scan delay be used to obtain maximum enhancement of the vessels?," Journal of computer assisted tomography 22 (4), 541-547 (1998).

28   J. F. Platt, K. A. Reige and J. H. Ellis, "Aortic enhancement during abdominal CT angiography: correlation with test injections, flow rates, and patient demographics," Ajr 172 (1), 53-56 (1999).

29   L. Kopka, J. Rodenwaldt, U. Fischer, D. W. Mueller, J. W. Oestmann and E. Grabbe, "Dual-phase helical CT of the liver: effects of bolus tracking and different volumes of contrast material," Radiology 201 (2), 321-326 (1996).

30   Y. Nakajima, T. Yoshimine, H. Yoshida, K. Sakashita, M. Okamoto, M. Kishikawa, K. Yagi, J. Yokota et al., "Computerized tomography angiography of ruptured cerebral aneurysms: factors affecting time to maximum contrast concentration," Journal of neurosurgery 88 (4), 663-669 (1998).

31   J. Kirchner, R. Kickuth, U. Laufer, M. Noack and D. Liermann, "Optimized enhancement in helical CT: experiences with a real-time bolus tracking system in 628 patients," Clinical radiology 55 (5), 368-373 (2000).

32   S. O. Casey, R. A. Alberico, M. Patel, J. M. Jimenez, R. R. Ozsvath, W. M. Maguire and M. L. Taylor, "Cerebral CT venography," Radiology 198 (1), 163-170 (1996).

33   H. Hacker and H. Becker, "Time controlled computed tomographic angiography," Journal of computer assisted tomography 1 (4), 405-409 (1977).

34   M. Wintermark, "Brain perfusion-CT in acute stroke patients," Eur Radiol 15 Suppl 4, D28-31 (2005).

35   R. Scaroni, N. Tambasco, G. Cardaioli, L. Parnetti, F. Paloni, B. Boranga and G. P. Pelliccioli, "Multimodal use of computed tomography in early acute stroke, part 2," Clin Exp Hypertens 28 (3-4), 427-431 (2006).

36   M. Wintermark, N. U. Ko, W. S. Smith, S. Liu, R. T. Higashida and W. P. Dillon, "Vasospasm after subarachnoid hemorrhage: utility of perfusion CT and CT angiography on diagnosis and management," AJNR Am J Neuroradiol 27 (1), 26-34 (2006).

37   G. D. Rubin, "Data explosion: the challenge of multidetector-row CT," European Journal of Radiology 36 (2), 74-80 (2000).

38   E. K. Fishman, D. R. Ney, D. G. Heath, F. M. Corl, K. M. Horton and P. T. Johnson, "Volume rendering versus maximum intensity projection in CT angiography: what works best, when, and why," Radiographics 26 (3), 905-922 (2006).

39   R. B. Schwartz, H. M. Tice, S. M. Hooten, L. Hsu and P. E. Stieg, "Evaluation of cerebral aneurysms with helical CT: correlation with conventional angiography and MR angiography," Radiology 192 (3), 717-722 (1994).

40   B. K. Velthuis, M. S. van Leeuwen, T. D. Witkamp, S. Boomstra, L. M. Ramos and G. J. Rinkel, "CT angiography: source images and postprocessing techniques in the detection of cerebral aneurysms," American Journal of Roentgenology 169 (5), 1411-1417 (1997).

41   H. W. Venema, F.J.H. Hulsmans, K.P. Van Lienden and G.J. den Heeten, "CT angiography with 0.5 mm collimation of the circle of Willis and the intracranial part of the internal carotid arteries: maximum intensity projection (MIP) with matched mask subtraction.," Radiology 213 (P), 311 (1999).

42   H. W. Venema, F. J. Hulsmans and G. J. den Heeten, "CT angiography of the circle of Willis and intracranial internal carotid arteries: maximum intensity projection with matched mask bone elimination-feasibility study," Radiology 218 (3), 893-898 (2001).

43   "Endarterectomy for asymptomatic carotid artery stenosis. Executive Committee for the Asymptomatic Carotid Atherosclerosis Study," Jama 273 (18), 1421-1428 (1995).

44   "Randomised trial of endarterectomy for recently symptomatic carotid stenosis: final results of the MRC European Carotid Surgery Trial (ECST)," Lancet 351 (9113), 1379-1387 (1998).

45   H. J. Barnett, D. W. Taylor, M. Eliasziw, A. J. Fox, G. G. Ferguson, R. B. Haynes, R. N. Rankin, G. P. Clagett et al., "Benefit of carotid endarterectomy in patients with symptomatic moderate or severe stenosis. North American Symptomatic Carotid Endarterectomy Trial Collaborators," The New England journal of medicine 339 (20), 1415-1425 (1998).

46   A. Halliday, A. Mansfield, J. Marro, C. Peto, R. Peto, J. Potter and D. Thomas, "Prevention of disabling and fatal strokes by successful carotid endarterectomy in patients without recent neurological symptoms: randomised controlled trial," Lancet 363 (9420), 1491-1502 (2004).

47   C. S. Cina, C. M. Clase and R. B. Haynes, "Carotid endarterectomy for symptomatic carotid stenosis," Cochrane Database of Systematic Reviews (2), CD001081 (2000).

48   A. F. Frangi, W. J. Niessen, R. M. Hoogeveen, T. van Walsum and M. A. Viergever, "Model-based quantitation of 3-D magnetic resonance angiographic images," IEEE Transactions on Medical Imaging 18 (10), 946-956 (1999).

49   L. M. Lorigo, O. D. Faugeras, W. E. Grimson, R. Keriven, R. Kikinis, A. Nabavi and C. F. Westin, "CURVES: curve evolution for vessel segmentation," Medical Image Analysis 5 (3), 195-206 (2001).

50   F. K. Quek and C. Kirbas, "Vessel extraction in medical images by wave-propagation and traceback," IEEE Transactions on Medical Imaging 20 (2), 117-131 (2001).

51   E. Meijering, M. Jacob, J. C. Sarria, P. Steiner, H. Hirling and M. Unser, "Design and validation of a tool for neurite tracing and analysis in fluorescence microscopy images," Cytometry 58A (2), 167-176 (2004).

52   H. Scherl, J. Hornegger, M. Prummer and M. Lell, "Semi-automatic level-set based segmentation and stenosis quantification of the internal carotid artery in 3D CTA data sets," Med Image Anal 11

(1), 21-34 (2007).

53 S. Suzuki, S. Furui, T. Kaminaga and T. Yamauchi, "Measurement of vascular diameter in vitro by automated software for CT angiography: effects of inner diameter, density of contrast medium, and convolution kernel," Ajr 182 (5), 1313-1317 (2004).

54 S. Suzuki, S. Furui and T. Kaminaga, "Accuracy of automated CT angiography measurement of vascular diameter in phantoms: effect of size of display field of view, density of contrast medium, and wall thickness," Ajr 184 (6), 1940-1944 (2005).

55 H. M. Silvennoinen, S. Ikonen, L. Soinne, M. Railo and L. Valanne, "CT angiographic analysis of carotid artery stenosis: comparison of manual assessment, semiautomatic vessel analysis, and digital subtraction angiography," AJNR Am J Neuroradiol 28 (1), 97-103 (2007).

56 Z. Zhang, M. H. Berg, A. E. Ikonen, R. L. Vanninen and H. I. Manninen, "Carotid artery stenosis: reproducibility of automated 3D CT angiography analysis method," Eur Radiol 14 (4), 665-672. Epub 2003 Nov 2014. (2004).

57 T. Boskamp, D. Rinck, F. Link, B. Kummerlen, G. Stamm and P. Mildenberger, "New vessel analysis tool for morphometric quantification and visualization of vessels in CT and MR imaging data sets," Radiographics 24 (1), 287-297 (2004).

58 J. Canny, "A computational approach to edge detection," IEEE Trans. Pattern Anal. Mach. Intell. 8 (6), 679-698 (1986).

59 A. F. Frangi, W. J. Niessen, P. J. Nederkoorn, J. Bakker, W. P. Mali and M. A. Viergever, "Quantitative analysis of vascular morphology from 3D MR angiograms: In vitro and in vivo results," Magn Reson Med 45 (2), 311-322 (2001).

60 H. Bouma, J. O. Bescos, A. Vilanova and F. A. Gerritsen, in Medical Imaging 2007: Image Processing (SPIE, San Diego, CA, USA, 2007), Vol. 6512, pp. 65122N-65131N.

61 H. Bouma, A. Vilanova, L. J. van Vliet and F. A. Gerritsen, "Correction for the dislocation of curved surfaces caused by the PSF in 2D and 3D CT images," IEEE transactions on pattern analysis and machine intelligence 27 (9), 1501-1507 (2005).

62 Paulo Mendonça, Dirk Padfield, James Miller and Matt Turek, in Computer Vision - ECCV 2004 (2004), pp. 554-565.

63 S. Worz and K. Rohr, "Cramer-Rao Bounds for Estimating the Position and Width of 3D Tubular Structures and Analysis of Thin Structures with Application to Vascular Images," J. Math. Imaging Vis. 30 (2), 167-180 (2008).

64 Stefan Wörz and Karl Rohr, in Medical Image Computing and Computer-Assisted Intervention – MICCAI 2004 (2004), pp. 491-499.

65 Stefan Wörz and Karl Rohr, in Bildverarbeitung für die Medizin 2006 (2006), pp. 186-190.

66 G.H. Granlund, "Fourier Preprocessing for hand print character recognition," IEEE Trans. Computers C-21 (Febr), 195-201 (1972).

67 C.T. Zahn and R.Z. Roskies, "Fourier descriptors for plane close curves," IEEE Trans. Computers C-21 (March), 269-281 (1972).

68 W. S. Smith, H. C. Roberts, N. A. Chuang, K. C. Ong, T. J. Lee, S. C. Johnston and W. P. Dillon, "Safety and feasibility of a CT protocol for acute stroke: combined CT, CT angiography, and CT perfusion imaging in 53 consecutive patients," AJNR Am J Neuroradiol 24 (4), 688-690 (2003).

69 M. Wintermark, R. Meuli, P. Browaeys, M. Reichhart, J. Bogousslavsky, P. Schnyder and P. Michel, "Comparison of CT perfusion and angiography and MRI in selecting stroke patients for acute treatment," Neurology 68 (9), 694-697 (2007).

70 H. C. Roberts, T. P. Roberts, W. S. Smith, T. J. Lee, N. J. Fischbein and W. P. Dillon, "Multisection dynamic CT perfusion for acute cerebral ischemia: the "toggling-table" technique," AJNR Am J Neuroradiol 22 (6), 1077-1080 (2001).

71 E. Siebert, G. Bohner, M. Dewey, F. Masuhr, K. T. Hoffmann, J. Mews, F. Engelken, H. C. Bauknecht et al., "320-slice CT neuroimaging: initial clinical experience and image quality evaluation," The British journal of radiology (2009).

72 M. Wintermark, M. Reichhart, O. Cuisenaire, P. Maeder, J. P. Thiran, P. Schnyder, J. Bogousslavsky and R. Meuli, "Comparison of admission perfusion computed tomography and qualitative diffusion- and perfusion-weighted magnetic resonance imaging in acute stroke patients," Stroke 33 (8), 2025-2031 (2002).

73 S. W. Youn, J. H. Kim, Y. C. Weon, S. H. Kim, M. K. Han and H. J. Bae, "Perfusion CT of the brain using 40-mm-wide detector and toggling table technique for initial imaging of acute stroke," Ajr 191 (3), W120-126 (2008).

2

Removal of bone in CT angiography by multiscale matched mask bone elimination

Hugo A.F. Gratama van Andel, Henk W. Venema, Geert J. Streekstra, Marcel van Straten, Charles B.L.M. Majoie, Gerard J. den Heeten and Cornelis A. Grimbergen

ABSTRACT

For clear visualization of vessels in CT angiography (CTA) images of the head and neck using maximum intensity projection (MIP) or volume rendering (VR) bone has to be removed. In the past we presented a fully automatic method to mask the bone (matched mask bone elimination, MMBE) for this purpose. A drawback is that vessels adjacent to bone may be partly masked as well. We propose a modification, multiscale MMBE, which reduces this problem by using images at two scales: a higher resolution than usual is used for image processing, and a lower resolution to which the processed images are transformed for use in the diagnostic process. A higher in-plane resolution is obtained by the use of a sharper reconstruction kernel. The out-of-plane resolution is improved by deconvolution or by scanning with narrower collimation. The quality of the mask that is used to remove bone is improved by using images at both scales. After masking, the desired resolution for the normal clinical use of the images is obtained by blurring with Gaussian kernels of appropriate widths. Both methods (multiscale and original) were compared in a phantom study and with clinical CTA data sets. With the multiscale approach the width of the strip of soft tissue adjacent to the bone that is masked can be reduced from 1.0 mm to 0.2 mm without reducing the quality of the bone removal. The clinical examples show that vessels adjacent to bone are less affected and therefore better visible. Images processed with multiscale MMBE have a slightly higher noise level or slightly reduced resolution compared with images processed by the original method and the reconstruction and processing time is also somewhat increased. Nevertheless multiscale MMBE offers a way to remove bone automatically from CT angiography images without affecting the integrity of the blood vessels. The overall image quality of MIP or VR images is substantially improved relative to images processed with the original MMBE method.

I. INTRODUCTION

Computed tomography angiography (CTA) makes it possible to visualize the arteries and veins in a minimally invasive way. Visualization is often performed by means of maximum intensity projection (MIP) or volume rendering (VR) so that the contrast-enhanced vessels can be examined easily. In a CTA data set the maximum value along a line in the direction of projection often belongs to a bone structure, which obscures the vessels in MIP images. In VR images bone may also affect the visualization of the vessels because of an overlap of the CT values of bone and the contrast agent in the vessels. Therefore the voxels that represent bone have to be removed from the data set prior to visualization.[1-3]

Manual removal of bone from CTA images can be very time consuming or virtually impossible when arteries are in close proximity of bone. Automated methods are based on image processing techniques, such as region-growing and thresholding.[4-8] Unfortunately these methods are time-consuming as well, and they are subjective because they require user-interaction. Because it is difficult to find the exact border between bone and contrast-enhanced vessels, the results of these techniques are not optimal, i.e. the bone removal is often incomplete or part of the vasculature is removed.

Matched mask bone elimination (MMBE) is a fully automatic technique and has proven to be a robust method for bone removal.[9-12] For CTA examinations with the MMBE method two scans are made: a low dose scan (a quarter of the dose of the CTA scan) without contrast injection and a normal CTA scan. After registration of the two scans, the nonenhanced scan is converted into a binary mask, which is then used to remove the bone in the CTA scan. A problem that arises when masking a bone in a CT image, is that a thin strip of adjacent tissue is masked as well due to the non-zero width of the point spread function (PSF) (Fig. 1). When arteries or veins are in close proximity of bone this may affect their integrity as they are eroded by the mask. CTA examinations are reconstructed in the clinical routine with a rather smooth reconstruction kernel in order to achieve an acceptable noise level. Therefore the resulting in-plane point spread function is broad and a relatively broad strip adjacent to the bone is masked.
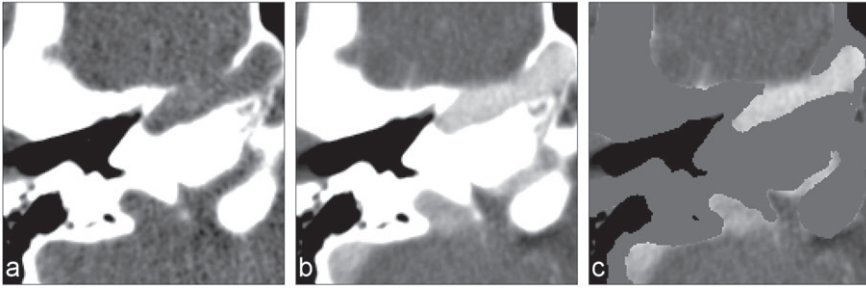
Fig. 1

Illustration of bone removal with the MMBE method on a region of interest (ROI) of 50 x 50 mm2 of axial images of the petrous segment of the right internal carotid artery. Window center: 100 HU. Window width: 500 HU. (a) Registered nonenhanced image, (b) CTA image and (c) CTA image after masking of the bone voxels. The borders of the adjacent vessels are masked as well.

The width of the PSF in the z-direction (the slice width), which is the direction of the table movement is also not negligible. This will also result in a relatively broad strip adjacent to the bone that is masked in the z-direction.

In this paper we present an alternative approach, multiscale MMBE, that addresses the problem of erosion of the vessels. In multiscale MMBE CT images are used that have a higher resolution than usual in image processing and masking. The quality of the mask is improved by combining the information from two versions of the nonenhanced scan, a high resolution and a low resolution image, i.e. at two scales. Because of the higher resolution the bone and the vessels will have less overlap, and therefore the vessels will be less affected in the masking process. Images with less noise, that are desired for the diagnostic process, are obtained in the final step by blurring the processed images.

We compare the performance of the multiscale and the original MMBE method in a phantom study and examples of CTA scans of patients.

II. MULTISCALE MMBE

A flow-diagram of the multiscale MMBE method is shown in Fig. 2 The method consists of the following steps:

1a.   Reconstruction of the nonenhanced scan and the CTA scan with a sharper reconstruction filter than the one that is normally used for CTA examinations.

1b.   Increase the resolution in the z-direction, either by deconvolution[13,14] when

the CT scan can not be made with a smaller slice width, or by scanning with a smaller slice width when this is possible.

2. Registration of the high resolution nonenhanced and CTA images.

3-6. Construction of the mask. The procedure is more involved than in the original MMBE method since the increased noise level in the high resolution images has to be taken into account.

7. Masking of the bone voxels.

8. Blurring of the sharp images to obtain images that can be used in the diagnostic process.

9. Production of MIP or VR images.

The original MMBE method uses smooth images with a relatively large slice width and consists of steps 2, 3, 7 and 9. The different steps of multiscale MMBE are discussed below.
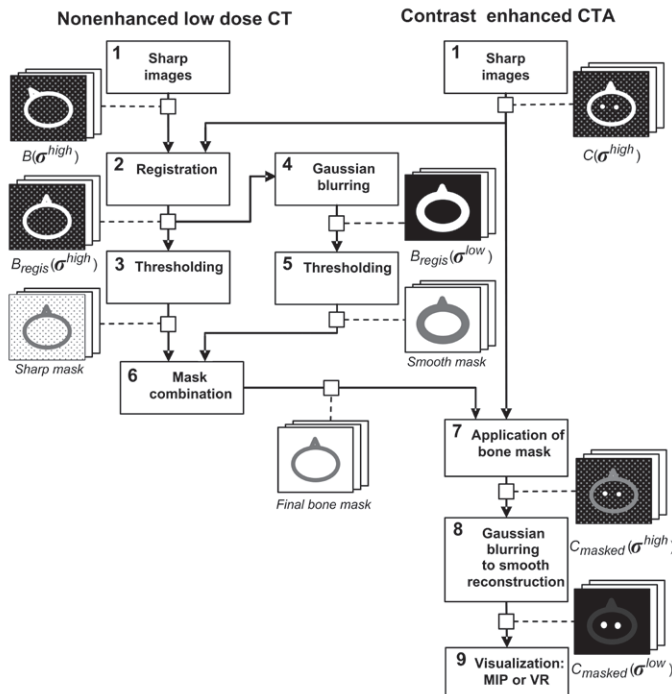

Fig. 2

Flow diagram of the multiscale MMBE method. Below the images the symbolic notations are denoted that are used in the different stages of multiscale MMBE (see Sec. II.A to II.D).

II. A. LOW AND HIGH RESOLUTION CT IMAGES (STEP 1)

In a CT scan all structures are imaged with blurred boundaries with an unsharpness that can be quantified by the point spread function (PSF). We approximate the PSF by a three dimensional (3D) Gaussian:[15]

$$PSF(\boldsymbol{x},\boldsymbol{\sigma}) \approx G(\boldsymbol{x},\boldsymbol{\sigma}) \equiv \frac{1}{(2\pi)^{\frac{3}{2}}\sigma_{xy}^2\sigma_z}\,e^{-\frac{1}{2}\left(\frac{x^2+y^2}{\sigma_{xy}^2}+\frac{z^2}{\sigma_z^2}\right)} \tag{1}$$

with $x=(x,y,z)$, x and y the in-plane coordinates and z the coordinate in the direction of the table movement, and $\boldsymbol{\sigma}=(\sigma_x,\sigma_y,\sigma_z)$ the standard deviation of the Gaussian in three directions. Because of the in-plane symmetry $\sigma_x=\sigma_y=\sigma_{xy}$. The standard deviation ó is in this study also indicated with the term *scale*.

The reconstructed nonenhanced images, $B(\boldsymbol{x},\boldsymbol{\sigma})$ and the contrast-enhanced images, $C(\boldsymbol{x},\boldsymbol{\sigma})$ are the result of the convolution of the corresponding object functions $B_0(x)$ and $C_0(x)$ with the $PSF()$:

$$B(\boldsymbol{x},\boldsymbol{\sigma}) = B_0(x) * PSF(\boldsymbol{x},\boldsymbol{\sigma}) \tag{2}$$

$$C(\boldsymbol{x},\boldsymbol{\sigma}) = C_0(x) * PSF(\boldsymbol{x},\boldsymbol{\sigma}) \tag{3}$$

The object functions represent the distribution of the true CT values in 3D space. In practice $B(\boldsymbol{x},\boldsymbol{\sigma})$ and $C(\boldsymbol{x},\boldsymbol{\sigma})$ are available for discrete voxel coordinates only; they are denoted as $B(\boldsymbol{\sigma})$ and $C(\boldsymbol{\sigma})$.

The in-plane resolution and the resolution in the z-direction depend on different factors. The in-plane resolution depends on factors related to the data acquisition, such as the focal spot size, detector size, geometric factors, integration time in the read-out of the detectors, and on the convolution kernel used in the reconstruction process, which may vary from smooth (low resolution) to sharp (high resolution). The standard deviation of the in-plane PSF of reconstructions made with the smooth and the sharp reconstruction kernel are denoted by σ_{xy}^{low} and σ_{xy}^{high}, respectively.

The resolution in the z-direction is determined by the choice of the slice width. With older scanners, the possibilities for the reduction of the slice width are limited,

because with these scanners a high z-resolution can only be obtained by using narrow collimation which prolongs the scan time. When narrow collimation is not used some improvement in the resolution can be obtained with deconvolution. With state-of-the-art multi-slice CT scanners it is possible to make scans with a very small slice width in a short scan time, and thus the high z-resolution can be obtained straightforward. In the present study we used both scanning with a relatively large slice width followed by deconvolution, and scanning with a narrow slice width, to obtain images with a higher resolution in the z-direction. The standard deviation of the PSF in the z-direction for the images with the lower and the higher resolution are denoted by σ_z^{low} and σ_z^{high}, respectively.

After image processing the smooth images that are required for the final visualization are obtained from the sharp images by means of blurring with a 3D Gaussian kernel with standard deviation $\boldsymbol{\sigma}^{blur}$. This procedure does not *exactly* restore the combination of in-plane resolution and noise of the reconstructions obtained with the smooth kernel. The reason is that the Gaussian kernel is only an approximation to the kernel that is required for the transformation between sharp and smooth images, and because of reasons of noise aliasing.[16] However, the Gaussian approximation is reasonable, as will be shown in this paper. In the z-direction no such problems are expected.

II.B. REGISTRATION (STEP 2)

The nonenhanced images and the CTA images are registered to compensate for patient movements between the two scans. The same method is used as in the original MMBE method.[9]

II.C. CONSTRUCTION OF THE BONE MASK (STEP 3-6)

The basic step of the construction of the bone mask consists of thresholding of the registered nonenhanced images, $B_{regis}(\boldsymbol{\sigma}^{high})$. Thresholding alone, however, produces a bone mask of unacceptable quality. This is caused by the large number of voxels that are erroneously incorporated in the mask due to the noise in the image. To overcome this problem an additional smoothed image $B_{regis}(\boldsymbol{\sigma}^{low})$ is made, which is obtained by convolution of the sharp image $B_{regis}(\boldsymbol{\sigma}^{high})$ with a

Gaussian kernel with standard deviation σ^{blur}. This image is also thresholded.

For both images the same threshold τ is used, which results in two binary masks, the sharp and the smooth mask (Fig. 3b and Fig. 3c). A preliminary mask is obtained by taking all voxels that the smooth and sharp mask have in common (Fig. 3d). This step removes the isolated voxels from the sharp mask that were incorporated due to noise.

In the construction of the preliminary mask also some voxels corresponding to small bone structures are removed because they are below the threshold τ in the smooth version of the nonenhanced images. Most of these bone structures, e.g. in the inner ear, the nasal cavity and the paranasal sinuses, are surrounded by air, which will cause their intensity to decrease substantially in the blurring process. These voxels are identified by making an additional binary mask (the high-decrease mask) by taking the difference of the sharp image and the smooth image, and thresholding this difference image with threshold δ. The voxels that are present in both the high-decrease mask and the sharp mask (Fig. 3e) are added to the preliminary mask to obtain the final bone mask (Fig. 3f).

In the original MMBE method the bone mask is dilated slightly to improve the quality of the bone removal. Dilation will remove structures close to the mask that have intensities below τ, but still may hinder visualization of vessels. In multiscale MMBE this step is less important because the final blurring (see next paragraph) reduces the intensity of any residual bone edge to a considerable amount. Dilation of the mask was therefore investigated as an optional step.
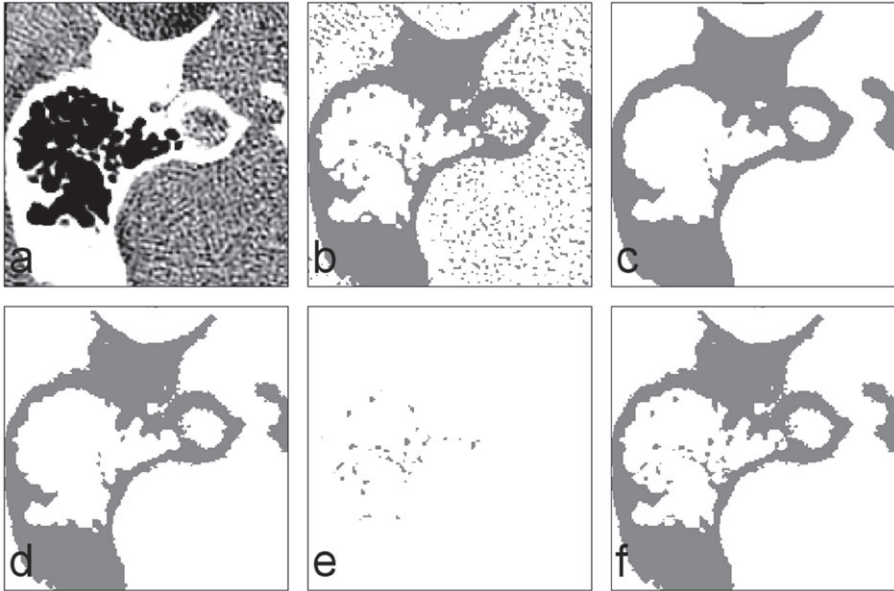
Fig. 3
Construction of the bone mask from a sharply reconstructed nonenhanced image (a) on a ROI of 45 x 45 mm2. Window center: 60 HU. Window width: 400 HU. The sharp mask (b) is obtained by thresholding (a) at 150 HU, the smooth mask (c) is obtained by thresholding a blurred version of (a) at 150 HU and the preliminary mask (d) is obtained by taking all voxels that masks (b) and (c) have in common. Image (e) shows the voxels that are present both in the high-decrease mask (not shown) and in the sharp mask (b). The final bone mask (f) is a obtained by adding the voxels of (e) to those in (d).

II.D. MASKING AND BLURRING (STEP 7 AND 8)

In the masking step the CT values of the voxels in the sharp CTA scan, $C(\sigma^{high})$ that are present in the bone mask are replaced by a value ζ. Next Gaussian blurring is applied with σ^{blur} to obtain the clinically desired noise level. After the Gaussian blurring the images can be visualized by MIP or VR.

II.E. PARAMETERS

Multiscale MMBE has seven parameters, three scale parameters (with two components) and four parameters used in the image processing: (1) σ^{low}, the scale of the images used in clinical practice; (2) σ^{high}, the scale chosen for the processing of the images, (3) σ^{blur}, the scale that is used to convert the high-resolution into the low-resolution images, (4) threshold τ that is used for the preliminary version of

the mask, (5) threshold δ that is used for refinement of the mask, (6) the number of voxels that is used in the (optional) dilation step and (7) the CT value ζ that is given to the masked voxels.

We consider the first parameter $\boldsymbol{\sigma}^{low}$ to be fixed, as this is the resolution used in clinical practice in the radiology department in our hospital. The third parameter, $\boldsymbol{\sigma}^{blur}$, can to a first approximation be derived from $\boldsymbol{\sigma}^{low}$ and $\boldsymbol{\sigma}^{high}$, as will be discussed in the next section. Therefore five main parameters remain that have to be chosen, $\boldsymbol{\sigma}^{high}$ (with two components, σ_{xy}^{high} and σ_z^{high}), τ, δ, the number of voxels dilatation, and ζ. The choice of these parameters is explained in the next section.

III. EXPERIMENTS

III.A. CT SCANS

CT scans were made with a CT scanner with four detector arrays (Mx8000 Quad; Philips Medical Systems; Best; The Netherlands). All scans were made with a tube voltage of 120 kV, head mode, high resolution, 0.75 sec per 360 degrees rotation and a pitch of 0.875 (table feed 4.7 mm/s), unless indicated otherwise. The collimation used was either 4 x 1 mm (nominal slice width 1.3 mm) or 2 x 0.5 mm (nominal slice width 0.6 mm). All reconstructions were made with a field-of-view of 150 mm and a 512 x 512 matrix, resulting in a pixel size of 0.293 x 0.293 mm². For use in multiscale MMBE reconstructions were made with kernel D (sharp), which is the sharpest reconstruction kernel available, and a slice increment of 0.1 mm. A small slice increment was chosen because this is preferable when deconvolution is used.[14] The scans were also reconstructed with kernel B (smooth) and a slice increment of 0.5 mm, which is the routine setting for reconstruction of CTA scans in our hospital, for processing with the original MMBE method. The Fourier transforms of kernels B and D for the head mode and high resolution are shown in Fig. 4 All reconstructions were made using an iterative beam hardening correction (UltraImage option).
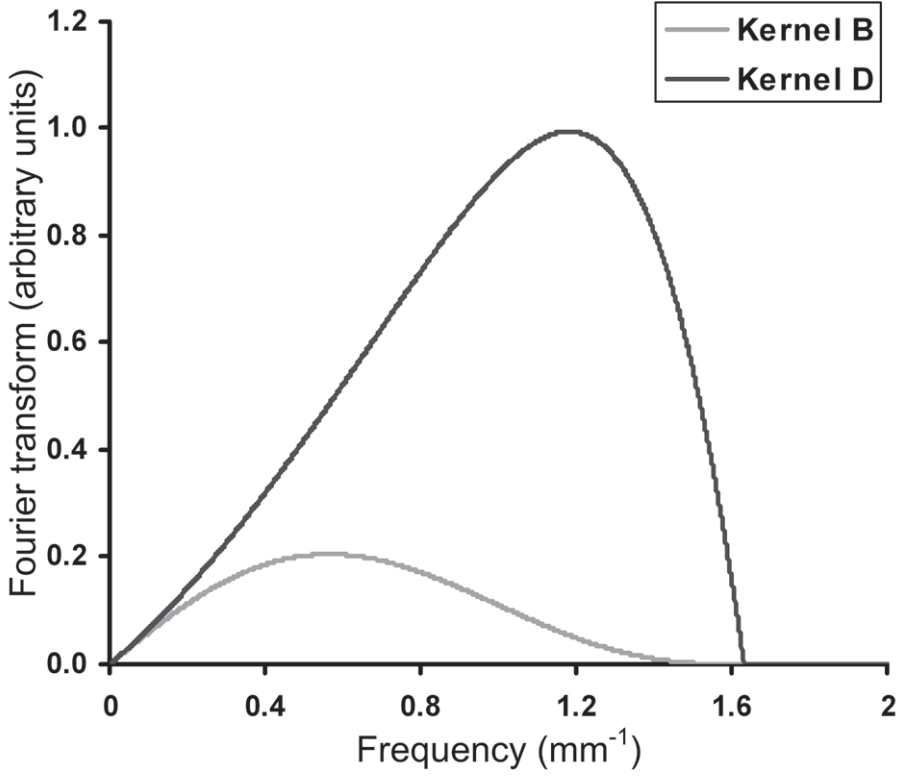
Fig. 4
Fourier transforms of the two reconstruction kernels B (smooth, lower curve) and D (sharp, upper curve).

III.B. REDUCTION OF THE SLICE WIDTH

1. COLLIMATION 4 X 1 MM

The resolution in the z-direction of the images acquired with a collimation of 4 x 1 mm was increased (from σ_z^{low} to σ_z^{high}) with the aid of constrained iterative deconvolution.[13,14] The value of σ_z^{high} that is obtained is determined by the choice of the parameter σ_z^{dcv}, with

$$\sigma_z^{high} = \sqrt{\left(\sigma_z^{low}\right)^2 - \left(\sigma_z^{dcv}\right)^2} \tag{4}$$

The deconvolution consist of a number of steps, each step consisting of improvement of the longitudinal resolution, followed by blurring of the improved

image with σ_z^{dcv}. This procedure is continued until the difference between the blurred improved image and the original image is smaller than a predetermined threshold.

In the deconvolution procedure we choose $\sigma_z^{dcv} = 0.25$ mm. In this way only a limited reduction of the width of the PSF was obtained. This choice was made, however, in order to keep the introduction of edge ringing artifacts in the deconvolved images that are inevitable in a deconvolution procedure to a minimum.[14]

2. COLLIMATION 2 X 0.5 MM

The images acquired with 2 x 0.5 mm already have the desired higher resolution in the z-direction (σ_z^{high}). After image processing and masking the images are blurred to a lower resolution (σ_z^{low}). We choose this lower resolution to be the same as the original z-resolution of the images acquired with a collimation of 4 x 1 mm for reasons of comparison.

III.C. MEASUREMENT OF THE POINT SPREAD FUNCTION

The standard deviation of the in-plane PSF was determined by making a scan of a cylindrical water-filled phantom with a diameter of 20 cm containing three steel wires (diameter 0.15 mm) that were aligned in the z-direction. The scan was made with 250 effective mAs. Reconstructions were made with kernels B and D and a pixel size of 0.1 x 0.1 mm^2. By fitting the convolution of a disk (diameter 0.15 mm) with a two dimensional (2D) Gaussian with a free parameter σ_{xy} to the reconstructed image data, the standard deviation of the in-plane PSF was estimated. This was done for each of the wires in five different images separately and $\bar{\sigma}_{xy}$ was obtained as the average value.

The standard deviation of the PSF in the z-direction was determined from scans of an edge of a cube made of polyvinyl chloride (PVC) with a CT number of approximately 1100 HU, surrounded by water. The scans were made with 250 effective mAs. The reconstructions were made with kernel D and a voxel size of 0.293 x 0.293 x 0.1 mm^3. From a region of 80 by 50 by 70 voxels containing the edge of the cube, 11 sagittal images of 80 by 70 pixels were used to estimate the standard deviation of the PSF in the z-direction by fitting a convolution of a

Gaussian and a step edge to the image data. The estimate of $\bar{\sigma}_z$ was obtained as the average standard deviation of these eleven images.

III.D. DETERMINATION OF $\boldsymbol{\sigma}^{blur}$

In case the PSFs are 3D Gaussian functions, the components of $\boldsymbol{\sigma}^{blur}$, which is used to blur the sharp images to the desired smooth resolution, (see Sec. II.A) are given by:

$$\sigma_{xy}^{blur} = \sqrt{\left(\sigma_{xy}^{low}\right)^2 - \left(\sigma_{xy}^{high}\right)^2} \tag{5}$$

and

$$\sigma_{z}^{blur} = \sqrt{\left(\sigma_{z}^{low}\right)^2 - \left(\sigma_{z}^{high}\right)^2} \tag{6}$$

Because the PSFs are only approximately Gaussian and because of the noise aliasing to be expected, we determined experimentally the value of $\boldsymbol{\sigma}^{blur}$ that has to be used to obtain images with the desired resolution and noise level. The resolution was measured for images blurred with a number of values of $\boldsymbol{\sigma}^{blur}$ as described in the previous section.

The noise level was quantified by measuring the standard deviation of the noise (SD_n) in a homogeneous region of interest, containing water, with an area of approximately 3 cm^2. Each noise measurement was performed in three images and averaged.

III.E. CHOICE OF THE IMAGE PROCESSING PARAMETERS

For the threshold for inclusion in the preliminary mask we used $\tau = 150$ HU. This value is the same as the threshold that was found optimal by Van Straten et al.[11] for the original MMBE method. For the threshold for inclusion in the high-decrease mask it appeared that $\delta = 250$ HU produced satisfactory results. For the CT value of the masked bone voxels we choose $\zeta = 20$ HU, which is approximately the value of brain tissue.

Multiscale MMBE was used both without and with dilation. Two different

amounts of dilation were tried, a kernel of four in-plane adjacent voxels, and a kernel of ten adjacent (eight in-plane and two out-of-plane) voxels. These kernels refer to a in-plane voxel size of 0.293 mm and an out-of-plane voxel size of 0.5 mm. The last kernel is also used in the original MMBE method.

In multiscale MMBE all image-processing was performed with a slice increment of 0.1 mm. One should expect that in this case dilation with five 0.1 mm voxels in the z-direction should be applied to obtain the same amount of dilation as with one 0.5 mm voxel. However in the case of 0.1 mm voxels the position of the border of the mask is slightly shifted as well, and it appeared that the same amount of dilation in the z-direction was obtained using three 0.1 mm voxels.

For the parameter values of the original MMBE method we choose the values that were found optimal by Van Straten et al.[11] apart from one small change: the value of V_{min}, the minimum volume of a connected object to be masked, was set to zero. This choice was made in order not to bias the original MMBE method negatively as further explained in the discussion.

III.F. PHANTOM STUDY

The influence of the bone removal method on the width of the strip of low density material adjacent to bone that is masked was investigated with a phantom. The phantom consists of a small block of PVC of approximately 3 x 4 x 4 cm^3, with a CT value of approximately 1100 HU. In this block three 5.0 mm diameter holes were drilled with angles of ninety and forty-five degrees (Fig. 5a). In these holes three cylinders made of polyoxymethylene (POM), with a diameter of 5.0 mm and a length of 40 mm, and with a CT value of approximately 300 HU can be inserted (Fig. 5b). These POM cylinders can also be placed in a holder of polymethylmethacrylate (PMMA) with the same three directions of the cylinders as in the cube of PVC (Fig. 5c). The block of PVC and the PMMA holder were placed in a water-filled cylinder made of PMMA, with an outer diameter of 5 cm. The phantom was aligned with one of the holes (or one of the cylinders) in the z-direction of the scanner. To obtain a noise level comparable to that in clinical scans, the cylinder containing the phantom was scanned in a ring made of PMMA with an outer diameter of 15 cm.

The three configurations of this phantom represent the different situations of

vessels in a CTA examination: nonenhanced in bone (*a*), contrast-enhanced in bone (*b*), and contrast-enhanced in tissue (as reference) (*c*).

Scans of the phantom were made using both 4 x 1 mm and 2 x 0.5 mm collimation. In both cases scans were made with 65 effective mAs for configuration (*a*), and 250 effective mAs for configuration (*b*) and (*c*). For the scans made with 2 x 0.5 mm collimation, the images that were used in the original MMBE method were obtained by Gaussian blurring of the thin slices in the *z*-direction to obtain the slice width of scans made with 4 x 1 mm collimation. Multiscale MMBE was applied using the scans of configuration (*a*) and (*b*).

The width of the masked strip of low-density material adjacent to bone was estimated by measuring the diameter of the cylinders in the processed images and the reference images. Cross sectional images of the cylinders were obtained by reslicing the 3D dataset. The direction of each cylinder was found by fitting a straight line to the center line points obtained by an automatic method for center line detection.[18] The diameter of the cylinders in two orthogonal directions was measured by fitting an ellipse convolved with two Gaussian functions with different standard deviations in the x- and y-direction to the cross-sectional images of the cylinders. This was done in 30 to 35 different cross sectional images of each cylinder with a spacing of approximately 1 mm, and the average was determined.
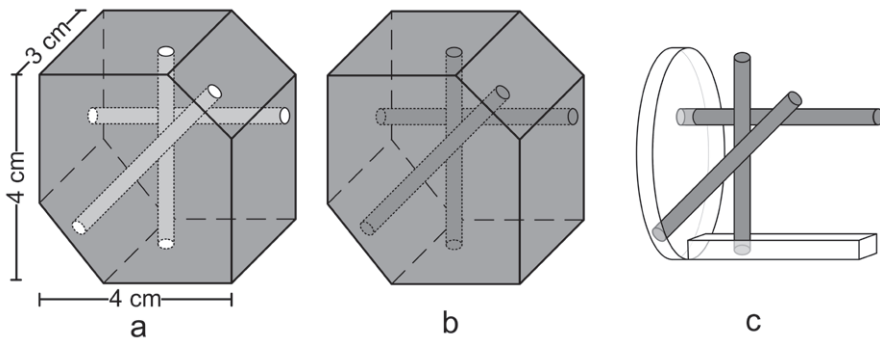

Fig. 5
A diagram of the three configurations of the phantom: (a) the PVC cube with water-filled holes, (b) the PVC cube filled with three POM cylinders and (c) the POM cylinders in a small PMMA holder. This represents three different situations of vessels in a CTA examination: nonenhanced in bone (a), contrast-enhanced in bone (b), and contrast-enhanced in tissue (as reference) (c).

III.G. EXAMPLES OF PATIENT STUDIES

Examples of two CTA examinations of the circle of Willis that were processed with multiscale MMBE, and with the original MMBE method for comparison, are presented. In one examination 4 x 1 mm collimation was used, in the other 2 x 0.5 mm collimation.

In the first patient (collimation 4 x 1 mm) 65 effective mAs was used for the nonenhanced scan, 250 effective mAs for the CTA scan and a tilt of -16°. Images were reconstructed with a nominal slice width of 1.3 mm, and processed using deconvolution.

In the second patient (collimation 2 x 0.5 mm) 100 effective mAs was use for the nonenhanced scan, 175 effective mAs for the CTA scan, a tilt of -12.5° and a pitch of 1.25. Images were reconstructed with a nominal slice width of 0.6 mm. In this case the final resolution in the z-direction (σ_z^{low}) was chosen such that the same slice width was obtained as in the first example, as already mentioned in section IIIb. Images with this same slice width were also processed with multiscale MMBE with deconvolution and the original MMBE method for comparison.

In both examples the quality of bone removal was quantified by measuring the standard deviation in a region of interest in the MIP image of 50 x 70 pixels and 42 x 42 pixels respectively in the MIP image where (almost) no vessels are present. For purposes of comparison all MIP-images were made using a slice increment of 0.5 mm.

IV. RESULTS

IV.A. MEASUREMENT OF THE POINT SPREAD FUNCTION

The values of the estimated σ_{xy} for the smooth and sharp kernel are shown in Table I. Also shown are the values of σ_z for 4 x 1 mm collimation before and after deconvolution and for 2 x 0.5 mm collimation.

Table I
Measured values of σ_{xy} for the kernel B and D, σ_z for 4 x 1 mm collimation before and after deconvolution, and σ_z for 2 x 0.5 mm collima

		symbol	σ (mm)	fwhm (mm)*
in-plane	kernel B (smooth)	σ_{xy}^{low}	0.431	1.015
	kernel D (sharp)	σ_{xy}^{high}	0.271	0.638
z-direction	4 x 1 collimation	σ_z^{low}	0.559	1.316
	4 x 1 collimation after deconvolution	σ_z^{high}	0.498	1.172
	2 x 0.5 collimation	σ_z^{high}	0.301	0.708

* fwhm (full width at half maximum) $= \sigma \times \sqrt{8\ln 2}$

IV.B. DETERMINATION OF σ^{blur}

The relation between σ_{xy} and the standard deviation of the noise (SD_n) after Gaussian blurring with for a number of values of σ_{xy}^{blur} is shown in Fig. 6. Using the values in Table I and formula (5) one calculates that for Gaussian PSFs blurring with a $\sigma_{xy}^{blur} = 0.335$ mm should restore the resolution of the smooth images (kernel B). As expected slight deviations occur: the resolution is restored with $\sigma_{xy}^{blur} = 0.404$ mm, the noise level with $\sigma_{xy}^{blur} = 0.451$ mm. Restoring the resolution results in a noise penalty of 18 %; restoring the noise level results in a 9 % increase in width of the PSF. We choose for this last option, for reasons mentioned in the discussion.
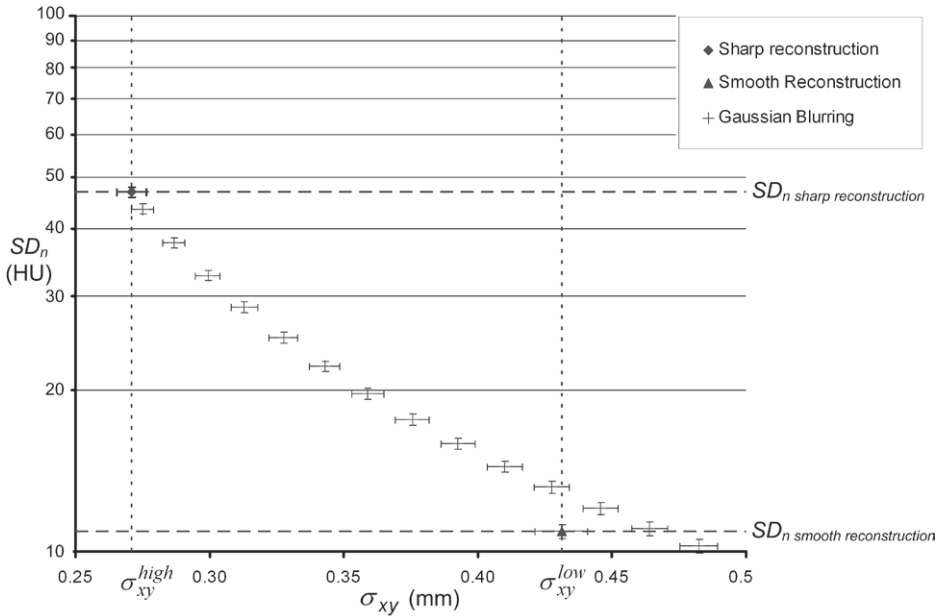
Fig. 6

Relation of σ_{xy} and the standard deviation of the noise (SDn) after Gaussian blurring with a number of values of σ_{xy}^{blur}. The two reconstruction filters; sharp, and smooth are denoted with a ♦ and ▲ marker, respectively. The resulting σ_{xy} and SDn after blurring with different values of σ_{xy}^{blur} are denoted with + markers. The standard deviation of the measurements are shown as horizontal en vertical bars.

For the blurring in the z-direction we found that the calculated values using Table I and formula (6), and the experimentally determined values of σ_z^{blur} are in good agreement. For the deconvolved scans made with 4 x 1 mm collimation, blurring in the z-direction with the calculated value $\sigma_z^{blur} = 0.254$ mm produced images with a slice width within 1 % of the desired slice width. Blurring with this calculated value of $\sigma_z^{blur} = 0.254$ mm did also restore the noise level within 1 %.

For scans made with 2 x 0.5 mm collimation blurring with the calculated value of $\sigma_z^{blur} = 0.471$ mm produced images within 1 % of the desired slice width. The noise level of these images was 4 % higher than the noise level of images acquired with 4 x 1 mm. This is a satisfactory agreement considering all the approximations involved.

IV.C. PHANTOM STUDY

The effect of the bone removal method on the profile of the CT values on a line through the center of a cross-section of the cylinder is shown in Fig. 7. Each line is an average of lines in 35 images with a spacing of 1 mm. From this figure the gain of multiscale MMBE is clear. The profile after application of multiscale MMBE resembles the 'true' profile (cylinder in water) much closer than when the original MMBE method is used. When dilation is performed the gain is somewhat reduced, but is still present. We note that one should expect the CT values in the center of the cylinder to be the same in the reference situation and after processing with MMBE. The small differences in CT-value were probably caused by residual errors in the beam-hardening correction, or by slight calibration errors of the CT-scanner.
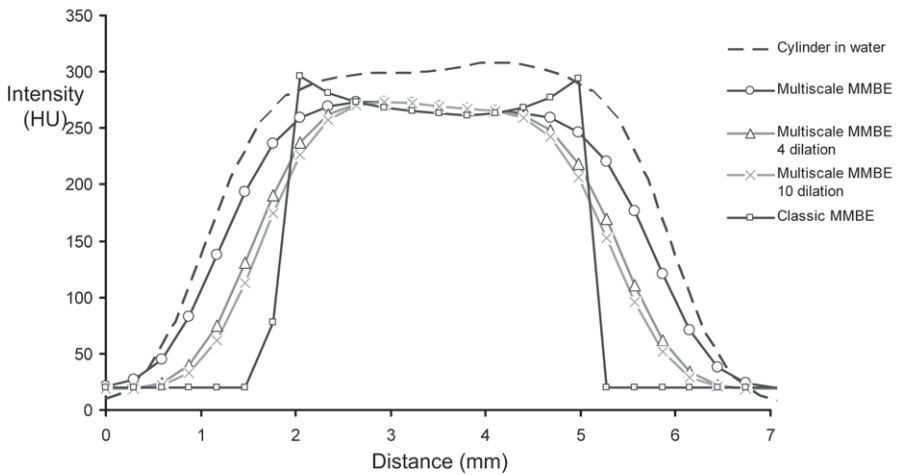
Fig. 7
The averaged intensity profiles through the cylinder (diameter 5.0 mm) orientated in the z-direction and scanned with 2 x 0.5 mm collimation. The profile in the reference situation is the dashed line without markers. The profiles after application of multiscale MMBE without, with 4 voxels and with 10 voxels of dilation are the solid lines with O, △ and × markers respectively. The profile after application of the original MMBE method is the solid black line with □ markers.

The estimated diameters of the cylinders with different orientations in the scans processed with multiscale MMBE and original MMBE are listed in Table II. For multiscale MMBE also dilation of the mask with four and ten voxels was used. For comparison the estimated diameters in the reference situation, the 5.0 mm cylinders in water, are also shown.

The widths of the strip adjacent to the bone that are masked with the different methods are shown in Table III. These values were obtained as the half of the difference of the reference diameter and the diameter in the processed images.

The estimated values in the xy-plane and in the plane with an angle of 45° are virtually the same for scans with a collimation of 4 x 1 mm and 2 x 0.5 mm. For 2 x 0.5 mm collimation the values for the cylinder with an angle of 90° with the z-axis are also comparable to those determined in the other orientations. For 4 x 1 mm collimation some anomalies are present in the measured diameters in the processed images in this last orientation. The estimated diameter in the x-direction appears to be somewhat low, and in the z-direction too high. Moreover in the measurements in the z-direction a trend was present, the diameter in the center of the cylinder being in the order of 0.15 to 0.25 mm higher than the average value and in the periphery up to 0.5 mm lower. These anomalies are probably due to interpolation artifacts in the z-direction at the high-contrast interface of the cylinder and the PVC surrounding, which appear to be more severe for 4 x 1 mm then for 2 x 0.5 mm collimation.

The standard deviations of the measurements were in the order of 0.05 mm for all reference diameters. In the processed images the standard deviation was in the order of 0.1 - 0.15 mm, with exception of the measurements in the z-direction in scans with a collimation of 4 x 1 mm. In this case the standard deviation was 0.24 mm due to the trend mentioned above.

Table II
The estimated diameters of the POM cylinders (diameter 5.0 mm) after application of multiscale MMBE, multiscale MMBE with 4 and 10 voxels dilation and original MMBE (with 10 voxels dilation). For comparison the estimated reference diameters are shown in the last column.

4 x 1 collimation		estimated diameter (mm)				
angle with the z-axis	diameter direction	multiscale MMBE	multiscale MMBE 4 dilation	multiscale MMBE 10 dilation	original MMBE	reference situation
0°	x	4.47	3.87	3.68	2.98	4.90
	y	4.59	3.94	3.72	3.07	5.05
45°	x	4.48	3.89	3.68	3.14	5.00
	y/z	4.49	3.87	3.58	3.03	4.97
90°	x	4.24	3.70	3.63	2.46	4.93
	z	4.86	4.36	3.92	3.15	5.16

2 x 0.5 collimation		estimated diameter (mm)				
angle with the z-axis	diameter direction	multiscale MMBE	multiscale MMBE 4 dilation	multiscale MMBE 10 dilation	original MMBE	reference situation
0°	x	4.61	3.94	3.72	3.10	5.02
	y	4.58	3.88	3.64	3.09	5.06
45°	x	4.64	3.92	3.72	3.23	4.99
	y/z	4.56	3.98	3.72	3.04	5.02
90°	x	4.51	4.01	3.87	3.37	5.00
	z	4.60	4.15	3.80	2.96	5.05

Table III
The calculated width of the masked strip adjacent to bone in multiscale MMBE, multiscale MMBE with 4 and 10 dilation, and in the original MMBE method.

4 x 1 collimation		masked strip adjacent to bone (mm)			
angle with the z-axis	diameter direction	multiscale MMBE	multiscale MMBE 4 dilation	multiscale MMBE 10 dilation	original MMBE
0°	x	0.21	0.51	0.61	0.96
	y	0.23	0.55	0.67	0.99
45°	x	0.26	0.56	0.66	0.93
	y/z	0.24	0.55	0.69	0.97
90°	x	0.35	0.62	0.65	1.24
	z	0.15	0.40	0.62	1.01

2 x 0.5 collimation		masked strip adjacent to bone (mm)			
angle with the z-axis	diameter direction	multiscale MMBE	multiscale MMBE 4 dilation	multiscale MMBE 10 dilation	original MMBE
0°	x	0.20	0.54	0.65	0.96
	y	0.24	0.59	0.71	0.98
45°	x	0.18	0.54	0.64	0.88
	y/z	0.23	0.52	0.65	0.99
90°	x	0.25	0.50	0.57	0.81
	z	0.22	0.45	0.62	1.04

IV.D. PATIENT EXAMPLES

The difference between multiscale MMBE and the original MMBE method is illustrated in Fig. 8 on axial images of the first patient. The first column shows a sharp CTA image masked using multiscale MMBE without and with dilation of the bone mask with four adjacent in-plane voxels. The middle column shows the same images after blurring to the desired resolution. The last column of Fig. 8 shows the image masked using the original MMBE method without dilation and with dilation of the bone mask with 8 in-plane and 2 out-of-plane voxels. In the images processed with multiscale MMBE (middle row) less erosion of vessels is visible in proximity of bone in comparison with original MMBE (bottom right), which confirms the results of the phantom study.
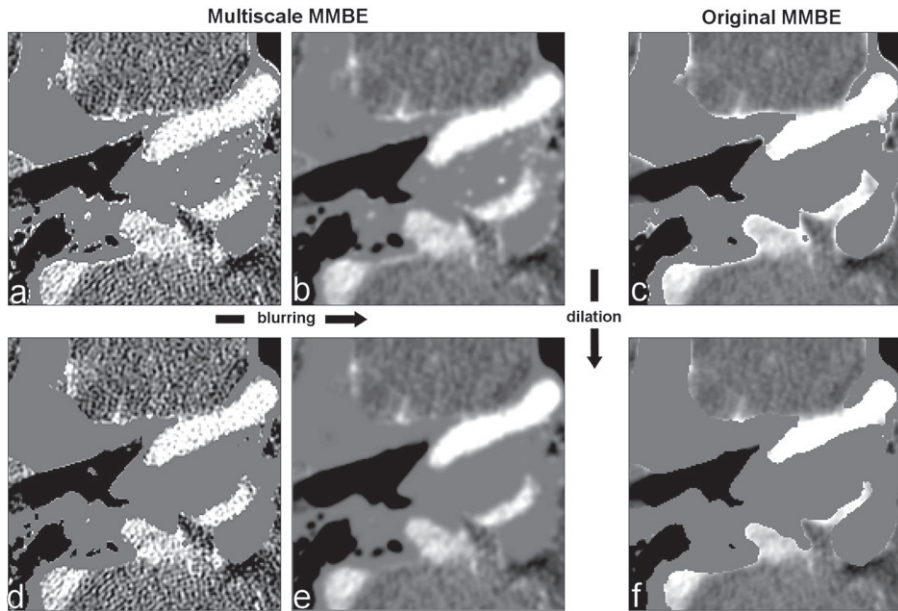
Fig. 8
 The effect of blurring and dilation illustrated with a ROI (50 x 50 mm2) of an axial image of the petrous segment of the internal carotid artery processed by multiscale MMBE (left and middle column) and the original MMBE method (right column). Window center: 50 HU. Window width: 300 HU. The first column shows the masked sharp CTA image without (a) and with (d) dilation by four adjacent in-plane voxels. The second column shows the same images after blurring (b and e). The third column shows the result of the original MMBE method without (c) and with dilation (f).

In Fig. 9 MIP images of the CTA examination of the circle of Willis of the first patient are shown (4 x 1 mm collimation). The quality of the bone removal of multiscale without dilation (Fig. 9a) is comparable with the quality of the original MMBE method (Fig. 9d). In both images some small bone remnants remain in the inner ear and the nasal cavity. Bone removal is more complete when dilation is used (Fig. 9 b and c) The standard deviation in the ROIs (see Fig. 9) where the skull base is masked are listed in Table IV.

Table IV
Quality of bone removal in two patients quantified by the standard deviation in a ROI without vessels after multiscale MMBE, multiscale MMBE with 4 and 10 voxels dilation, and the original MMBE method.

	SD ROI (HU)
Patient 1 (Fig. 9; 4 x 1 mm collimation)	
multiscale MMBE	27
multiscale MMBE (4 dilation)	20
multiscale MMBE (10 dilation)	19
original MMBE	27
Patient 2 (Fig. 11; 2 x 0.5 mm collimation)	
multiscale MMBE (thin slices, no dilation)	26
multiscale MMBE (thick slices, no dilation)	33
original MMBE	36

With multiscale MMBE less erosion of the vessels is present when they are close to bone. This can be observed in more detail in Fig. 10 where a region of interest (ROI) is shown of the location where the internal carotid artery passes through the skull base. Fig. 10 b and c show the trade-off of the quality of bone removal and the erosion of the vessels when dilation is used.

Fig. 9
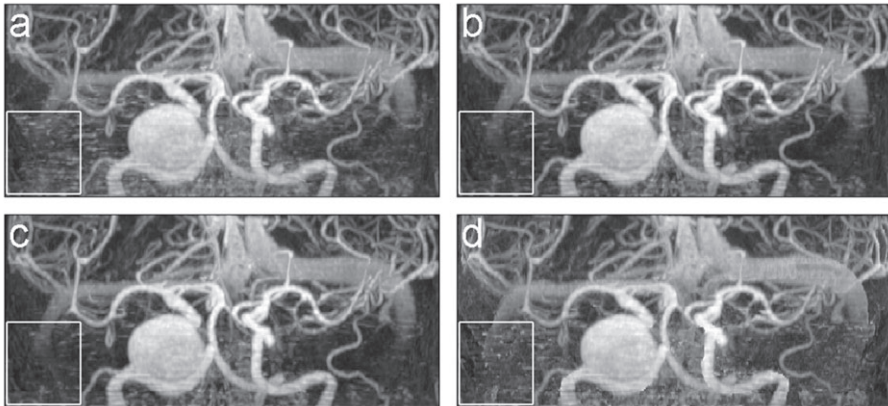Coronal MIP images (130 x 58 mm2) of a CTA examination of the circle of Willis. Window center: 50 HU. Window width: 300 HU. Bone was removed in (a) with multiscale MMBE without dilation, (b) with four voxels dilation and (c) with 10 voxels dilation. Image (d) was processed with the original MMBE method. The ROI where the SD is measured to quantify the bone removal is shown in the lower left.
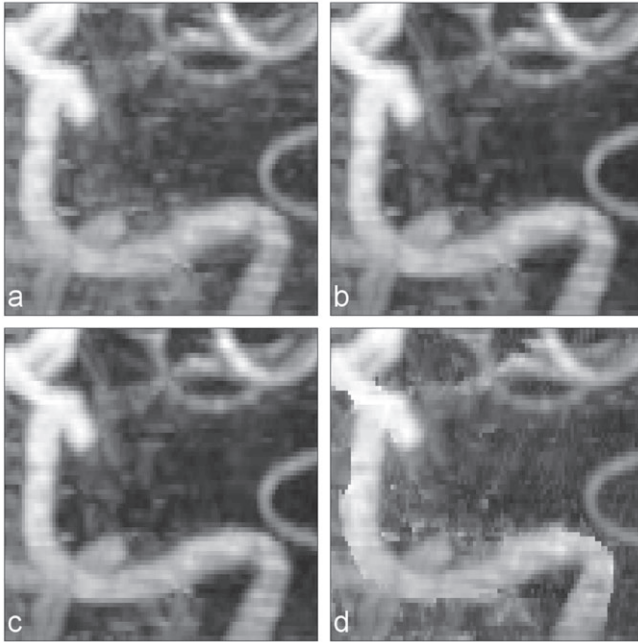
Fig. 10

Images of a ROI (30 x 30 mm2) of the left internal carotid artery from **Fig. 9**. Window center: 50 HU. Window width: 300 HU. Bone was removed with (a) multiscale MMBE without dilation, (b) with four voxels dilation and (c) with 10 voxels dilation. Image (d) was processed with the original MMBE method.

MIP images of the second patient (2 x 0.5 mm) are shown in Fig. 11. The result of multiscale MMBE using the original images is shown in Fig. 11a and b. The result of multiscale MMBE using the images with the same slice width as in the 4 x 1 mm scan, and deconvolution, is shown in Fig. 11c and d. In both approaches no dilation was used. The results of original MMBE method is shown in Fig. 11e and f. The standard deviation in the ROIs at the lower right in Fig. 11(a, c and e) are listed in Table IV.

In this example the main difference between multiscale MMBE using the thin slices (2 x 0.5 mm collimation) and the thicker slices followed by deconvolution, appears to be the more effective bone removal of the first method. No substantial differences can be seen in the integrity of the vessels. In both respects the multiscale method performs better than the original MMBE method.
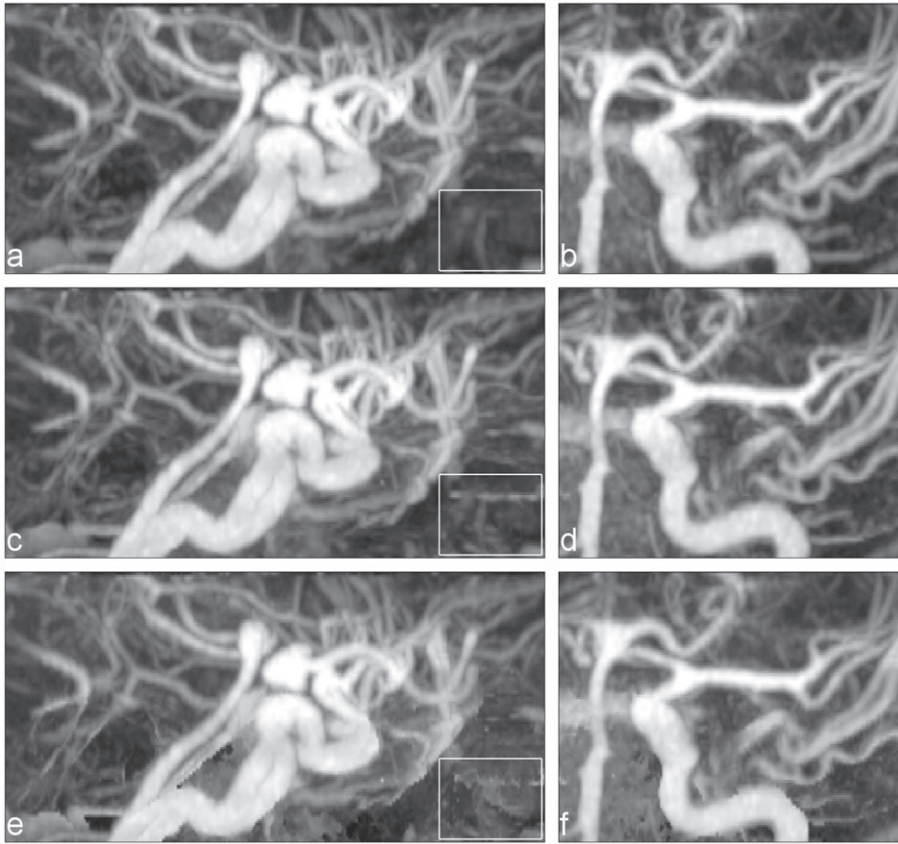
Fig. 11
Sagital (80 x 40 mm2) and coronal (50 x 40 mm2) MIP images of a CTA examination of the circle of Willis. Window center: 200 HU. Window width: 400 HU. Bone was removed with (a and b) multiscale MMBE with narrow collimation, (c and d) multiscale MMBE with deconvolution and (e and f) classic MMBE. The ROI where the SD is measured to quantify the bone removal (in the region of the nasal cavity) is shown in the lower right (a, c and e).

V. DISCUSSION

In this study multiscale MMBE is presented which is a modification of a method for automated bone removal from CTA scans. The main advantage of the multiscale approach over the original MMBE method is that the width of the strip of soft tissue adjacent to bone that is sacrificed in the masking process is substantially reduced, while the quality of the bone removal is retained or even improved.

In the phantom study the thickness of the strip of low density material adjacent to the bone, that is masked erroneously, was measured. The width of this strip is a measure for the maximum erosion of blood vessels adjacent to bone when MMBE is applied. In the original MMBE method the width of this strip is approximately 1.0 mm. With multiscale MMBE, the width of this strip was only 0.2 mm. When the mask was dilated with four voxels the width of the strip increased to 0.5 mm, dilation with 10 voxels increased it to 0.6 - 0.7 mm.

The gain that is obtained by using the sharper reconstruction kernel alone, can be observed by comparing the results of multiscale MMBE and the original method with the same amount of dilation of 10 voxels. In this case the erroneously masked strip is reduced from 1.0 to 0.6 - 0.7 mm. An additional advantage in multiscale MMBE is, however, that less dilation of the mask is needed than in the original MMBE method for the same quality of bone removal. This is because the final blurring step, required to reduce the noise to an acceptable level, has the positive side effect that the residual unmasked bone edges are reduced to a considerable extent.

From patient examples it is clear that removal of bone with multiscale MMBE is as effective as in the original MMBE, even when multiscale MMBE is used without dilation. With dilation of four voxels the quality of bone removal was even better than in the original MMBE. With the parameter settings used in the present study, one could therefore use either no dilation or dilation with four voxels to obtain a good trade-off between the quality of the bone removal and the preservation of the vessels, depending on the preference of the observer.

In our study we changed the setting of one parameter of the original MMBE method that we used for purposes of comparison.[11] This parameter is the minimum volume of connected voxels, V_{min}, that is included in the mask. This parameter was

introduced to eliminate spurious voxels due to noise in the mask. The use of the original value of V_{min} of 40 mm3 appeared to be counterproductive, however, as small bones or bone fragments remain unmasked, and noise did not appear to be a problem. Therefore in order not to bias the original MMBE method negatively, we decided not to use this criterion.

We compared two methods to improve the resolution in the z-direction: deconvolution in case the CTA examination was made with the usual collimation (4 x 1 mm), or scanning with narrower collimation (2 x 0.5 mm). Scanning with narrow collimation is more effective and thus preferable. With deconvolution the resolution can only be improved by a modest amount, otherwise edge ringing artifacts are introduced. Deconvolution has the further drawback that it is computational somewhat more expensive and that a small reconstruction increment has to be used, which prolongs the image reconstruction time. In the present study an increment of 0.1 mm was used, instead of an increment of 0.5 mm for 4 x 1 mm collimation. For a CT-scan with a length of 80 mm, for example, this means that an additional 640 images have to be reconstructed, which takes in the order of 10 tot 15 minutes for the CT-scanner used in the present study.

Scanning with sub-mm slice width, 2 x 0.5 mm instead of 4 x 1 mm collimation, to improve the z-resolution with the CT-scanner used in the present study, increases the scan time fourfold, all other things being equal. Therefore this last setting is not used routinely for CTA examinations. With state-of-the-art multislice CT-scanners, however, CTA examinations can be performed with sub-mm slice width (in the order of 0.5 to 0.7 mm) in a very short scan time. In this case scanning with very thin slices is a viable option, and processed images with a somewhat greater slice width and reduced noise level can be used in the final visualization step.

As mentioned in section II.E the value of four parameters have to be chosen for the processing of the high-resolution images: thresholds τ and δ that are used for the preliminary version and the refinement of the mask, respectively, the number of voxels that is used in the (optional) dilation step, and the value ζ that is given to the masked voxels. The optimal value τ for the main thresholding step depends primarily on the CT-values of soft tissue and of bone, respectively, and as these values are approximately constant in CTA examinations of the head and neck consistent results of the thresholding step are to be expected. We note that a higher value of τ has to be used when scans are made with a lower tube voltage,

as the CT-values of bone will then be systematically higher.[10] It appeared in some test experiments that the choice of the threshold δ is not critical, which is to be expected as it is used in the refinement of a bone mask that has already acceptable quality. The choice of the number of voxels used in the (optional) dilation of the mask was discussed above. The value ζ that is given to the masked voxels, was formally introduced as a parameter; it is an obvious choice, however, as in the masking process the bone voxels are replaced by voxels representing soft tissue, and therefore we used $\zeta = 20$ HU which is approximately the CT-value of soft tissue in the brain and neck. We finally note that in this study we have used images at the two scales $\boldsymbol{\sigma}^{high}$, and $\boldsymbol{\sigma}^{low}$, in the construction of the mask. Strictly spoken the lower scale that is used in this step should also be considered as a parameter, as it can be choosen freely. Because the high and the low scale were already considerably different, which is the main point in using two scales, we considered this to be an issue of minor importance, and we have not done so.

In the present implementation the final blurring step is performed with a Gaussian kernel. This approximation appears to be adequate for the z-direction. For the in-plane situation, we have shown that when the high-resolution images are blurred with a Gaussian kernel, an acceptable approximation of the images reconstructed with a smooth kernel can be obtained. Because of the approximation involved and because of noise aliasing, restoration of the PSF increases the noise level slightly, and restoration of the noise level increases the width of the PSF slightly. We choose for this last option, as radiologists appear to be relatively insensitive for small variation in resolution when judging CTA images of the brain.

The use of a Gaussian kernel in the final blurring step is computational efficient, as the kernel is separable. An exact transformation of the sharp to smooth images in the spatial domain is also feasible,[16] allbeit at the cost of efficiency, as the separability of the kernel is then lost. We are currently investigating this possibility.

In addition to the approach of the present study other approaches to improve the image quality are also feasible. Recently, Van Straten et al.[19] presented another modification, called soft MMBE, in which a combination of masking and local subtraction was applied. Application of subtraction at the bone-vessel interface does also reduce the erosion of vessels by the mask. Subtraction, however, inevitable leads to increase of noise in the subtracted region. It has the further drawback that the continuity needs to be restored between the original and the subtracted areas,

and that errors in the estimated offset value may show up as artifacts in the final images. Moreover, high-quality subtraction images are required, which can only be obtained when no significant interpolation artifacts are present. Therefore only scans can be used that are made at a low pitch,[20] which is only feasible in CT-scanners with a large number of detector arrays.

Another approach is the local adjustment of the threshold value above which the bone is masked.[21] By increasing the threshold value at the bone-vessel interface, less vessel will be masked. A drawback of this method is that the intensity profile of the vessel will still be influenced by the presence of the bone and will increase at the edges. When the original MMBE method is used this artifact is also present (see Fig. 7). In multiscale MMBE the intensity profile of the vessel decreases slowly at the edges due to smoothing step after the masking of the bone. This will resemble the true intensity profile of the vessel, only without the drawbacks of soft MMBE mentioned above.

A drawback of all masking methods in which an additional CT-scan is used is the additional radiation dose for the patient. This argument applies to multiscale MMBE, the original MMBE-method, and the above mentioned alternative approaches[19,21] as well. The increase in radiation dose with multiscale MMBE is only 25%, however, and the benefit of the masking of bone in the clinical routine is considerable.[10,12,22,23]

We conclude that the multiscale MMBE method is a substantial improvement over the original MMBE method and offers a way to remove bone from a CT angiography scan in a fully automatic and accurate way.

REFERENCES

1   R. B. Schwartz, K. M. Jones, D. M. Chernoff, S. K. Mukherji, R. Khorasani, H. M. Tice, R. Kikinis, S. M. Hooton et al., "Common carotid artery bifurcation: evaluation with spiral CT. Work in progress," Radiology 185 (2), 513-519 (1992).

2   R. B. Schwartz, H. M. Tice, S. M. Hooten, L. Hsu and P. E. Stieg, "Evaluation of cerebral aneurysms with helical CT: correlation with conventional angiography and MR angiography," Radiology 192 (3), 717-722 (1994).

3   S. Napel, M. P. Marks, G. D. Rubin, M. D. Dake, C. H. McDonnell, S. M. Song, D. R. Enzmann and R. B. Jeffrey, Jr., "CT angiography with spiral CT and maximum intensity projection," Radiology 185 (2), 607-610 (1992).

4   S. O. Casey, R. A. Alberico, M. Patel, J. M. Jimenez, R. R. Ozsvath, W. M. Maguire and M. L. Taylor, "Cerebral CT venography," Radiology 198 (1), 163-170 (1996).

5   M. Fiebich, C. M. Straus, V. Sehgal, B. C. Renger, K. Doi and K. R. Hoffmann, "Automatic bone segmentation technique for CT angiographic studies," J. Comput. Assist. Tomogr. 23 (1), 155-161 (1999).

6   E. K. Fishman, C. C. Liang, B. S. Kuszyk, S. E. Davi, D. G. Heath, D. Hentschel, S. V. Duffy and A. Gupta, "Automated bone editing algorithm for CT angiography: preliminary results," Am. J. Roentgenol. 166 (3), 669-672 (1996).

7   S. G. Wetzel, E. Kirsch, K. W. Stock, M. Kolbe, A. Kaim and E. W. Radue, "Cerebral veins: comparative study of CT venography with intraarterial digital subtraction angiography," Am. J. Roentgenol. 20 (2), 249-255 (1999).

8   B. K. Velthuis, M. S. van Leeuwen, T. D. Witkamp, S. Boomstra, L. M. Ramos and G. J. Rinkel, "CT angiography: source images and postprocessing techniques in the detection of cerebral aneurysms," Am. J. Roentgenol. 169 (5), 1411-1417 (1997).

9   H. W. Venema, F. J. Hulsmans and G. J. den Heeten, "CT angiography of the circle of Willis and intracranial internal carotid arteries: maximum intensity projection with matched mask bone elimination-feasibility study," Radiology 218 (3), 893-898 (2001).

10 C. B. Majoie, M. van Straten, H. W. Venema and G. J. den Heeten, "Multisection CT venography of the dural sinuses and cerebral veins by using matched mask bone elimination," AJNR. Am. J. Neuroradiol. 25 (5), 787-791 (2004).

11 M. van Straten, H. W. Venema, G. J. Streekstra, C. B. Majoie, G. J. den Heeten and C. A. Grimbergen, "Removal of bone in CT angiography of the cervical arteries by piecewise matched mask bone elimination," Med. Phys. 31 (10), 2924-2933 (2004).

12 M. Romijn, H. Gratama van Andel, M. A. van Walderveen, M.E. Sprengers, J.C. van Rijn, W.J. van Rooij, H. W. Venema, C. A. Grimbergen et al., "Diagnostic accuracy of CT Angiography with matched mask bone elimination for detection of intracranial aneurysms: comparison with digital subtraction angiography and 3D rotational angiography," AJNR. Am. J. Neuroradiol. 29 (1), in press (2008).

13 D. L. Snyder, M. I. Miller, L. J. Thomas and D. G. Politte, "Noise and Edge Artifacts in Maximum-Likelihood Reconstructions for Emission Tomography," IEEE Trans. Med. Imaging MI-6 (3), 228-238 (1987).

14 F. J. Schlueter, G. Wang, P. S. Hsieh, J. A. Brink, D. M. Balfe and M. W. Vannier, "Longitudinal image deblurring in spiral CT," Radiology 193 (2), 413-418 (1994).

15 G. Wang, M. W. Vannier, M. W. Skinner, M. G. Cavalcanti and G. W. Harding, "Spiral CT image

deblurring for cochlear implantation," IEEE Trans. Med. Imaging 17 (2), 251-262 (1998).

16 S. Schaller, J. E. Wildberger, R. Raupach, M. Niethammer, K. Klingenbeck-Regn and T. Flohr, "Spatial domain filtering for fast modification of the tradeoff between image sharpness and pixel noise in computed tomography," IEEE Trans. Med. Imaging 22 (7), 846-853 (2003).

17 P. M. Joseph and R. D. Spital, "A method for correcting bone induced artifacts in computed tomography scanners," J. Comput. Assist. Tomogr. 2 (1), 100-108 (1978).

18 G. J. Streekstra, R Van den Boomgaard and A. W. Smeulders, "Scale Dependency of Image Derivatives for Feature Measurement in Curvilinear Structures," International Journal of Computer Vision 42 (3), 177-189 (2001).

19 M. Van Straten, C. B. Majoie, H. W. Venema, L. Ciancibello and K. Subramanyan, "Automatic bone removal in CT angiography," Medica Mundi 49 (1), 4-8 (2005).

20 M. van Straten, H. W. Venema, J. Hartman, G. J. den Heeten and C. A. Grimbergen, "Reproducibility of multi-slice spiral computed tomography scans: an experimental study," Med. Phys. 31 (10), 2785-2786 (2004).

21 B. F. Tomandl, T. Hammen, E. Klotz, H. Ditt, B. Stemper and M. Lell, "Bone-subtraction CT angiography for the evaluation of intracranial aneurysms," Am. J. Roentgenol. 27 (1), 55-59 (2006).

22 M. Lell, K. Anders, E. Klotz, H. Ditt, W. Bautz and B. F. Tomandl, "Clinical evaluation of bone-subtraction CT angiography (BSCTA) in head and neck imaging," Eur. Radiol. 16 (4), 889-897 (2006).

23 M. Lell, B. F. Tomandl, K. Anders, U. Baum and E. Nkenke, "Computed tomography angiography versus digital subtraction angiography in vascular mapping for planning of microsurgical reconstruction of the mandible," Eur. Radiol. 15 (8), 1514-1520 (2005).

3

Diagnostic accuracy of CT angiography with matched mask bone elimination for detection of intracranial aneurysms: comparison with digital subtraction angiography and 3D rotational angiography

Marieke Romijn, Hugo A.F. Gratama van Andel, Marianne A. van Walderveen, Marieke E. Sprengers, Jeroen C. v Rijn, Willem Jan van Rooij, Henk W. Venema, Cornelis A. Grimbergen, Gerard J. den Heeten and Charles B.L.M. Majoie

ABSTRACT

The purpose of this study is to determine diagnostic accuracy of multislice computed tomography angiography combined with matched mask bone elimination (CTA-MMBE) for detection of intracranial aneurysms compared to digital subtraction angiography (DSA) with three-dimensional rotational angiography (3DRA).

Between January 2004 and February 2006, 108 patients that presented with clinical suspicion of subarachnoid hemorrhage underwent both CTA-MMBE and DSA for diagnosis of an intracranial aneurysm. Two neuroradiologists, independently, evaluated 27 predefined vessel locations in the CTA-MMBE images for the presence of an aneurysm. After consensus, diagnostic accuracy of CTA was calculated per predefined location and per patient. Interobserver agreement was calculated with κ statistics.

In 88 patients (81%) 117 aneurysms (82 ruptured, 35 unruptured) were present on DSA. CTA-MMBE detected all ruptured aneurysms but one. Overall specificity, sensitivity, positive predictive value and negative predictive value of CTA-MMBE was 0.99, 0.90, 0.98 and 0.95 per patient and 0.91, 1.00, 0.97 and 0.99 per location, respectively. Sensitivity was 0.99 for aneurysms ≥ 3 mm and 0.38 for aneurysms < 3 mm. Interobserver agreement for aneurysm detection was excellent (κ value 0.92 per location and 0.80 per patient).

CTA-MMBE is accurate in detecting intracranial aneurysms in any projection without overprojecting bone. CTA-MMBE has limited sensitivity in detecting very small aneurysms. Our data suggest that, after detection of a ruptured aneurysm with CTA, DSA and 3DRA can be limited to the vessel harboring the ruptured aneurysm prior to endovascular treatment.

I. INTRODUCTION

In current clinical practice, computed tomography angiography (CTA) is the most frequently used noninvasive diagnostic tool for detection of intracranial aneurysms in the acute setting.[1-8] However, detection of intracranial aneurysms by CTA is limited because axial source slice evaluation is tedious and three-dimensional (3D) visualization is hampered by overprojecting bone, especially in the region of the skull base.[2,9-13] Several methods to remove bone, such as subtraction and manual or automated bone editing have been developed.[7,8,14-19] Drawbacks of these methods are complexity in use, user dependency or high radiation dose.

Matched mask bone elimination (MMBE) is a relatively new technique to remove bone from CTA source images (CTA-MMBE) in an automatic and user independent way with little additional radiation dose.[20-22] In CTA-MMBE, a second nonenhanced low-dose scan (about a quarter of the radiation dose of a regular CTA) is used to identify bony structures that can subsequently be masked in the CTA scan.

Digital subtraction angiography (DSA) is the gold standard for detection of intracranial aneurysms. Extension of DSA with 3D rotational angiography (3DRA) can further improve detection of intracranial aneurysms, that may be obscured by overprojecting vessels.[23-25] Advantages of DSA over CTA are superior spatial and contrast resolution, no interference of bony structures and the possibility to perform direct endovascular interventions.[26,27] However, DSA is an invasive technique with a small but significant risk of neurologic complications, estimated to occur in $0.3 - 1.8\%$ of cases.[28,29]

The purpose of this study is to determine the diagnostic accuracy of CTA-MMBE for detection of intracranial aneurysms in a large patient population with clinical suspicion of subarachnoid hemorrhage (SAH) with DSA and 3DRA as reference standard.

II. METHODS

II.A. PATIENTS

Between January 2004 and February 2006, 108 patients that presented with clinical suspicion of SAH underwent both CTA-MMBE and DSA for diagnosis of an intracranial aneurysm. Of 108 patients, 102 had SAH confirmed by CT scan or lumbar puncture. There were 81 women and 27 men with a mean age of 56 years (median 53, range 19-92 years). In general, when one or more aneurysms were found on CTA or DSA, additional 3DRA was performed for pre-treatment planning. Approval from the institutional review board for review of the patient's medical records and images was obtained. Since CTA-MMBE and DSA / 3DRA were part of routine clinical practice no approval was required to perform these imaging modalities in the patient group.

II.B. IMAGING

The technique of CTA-MMBE has been published before.[20] Parameters settings were used as found optimal by Van Straten et al.[22] Briefly, in MMBE an additional nonenhanced low dose spiral CT (65 mAs) is used to identify bony structures that are subsequently masked on CTA images (Fig 1 a-c). These scans were made on a 4-slice spiral CT scanner (Philips MX8000; Philips Medical Systems, Best, The Netherlands or Siemens Sensation 4, Siemens Medical Solutions, Erlangen, Germany). Following parameters were used: 120kV, 250 mAs, 4 x 1 mm detector collimation; pitch 0.875; slice thickness 1.3 mm; increment 0.5 mm; 150 mm field of view; 512^2 matrix; reconstruction-kernel B (Philips) and H30f (Siemens). Eighty to 100 ml of non-ionic contrast material was injected in a cubital vein at a rate of 4 ml/s. Scan delay was automatically adjusted by a bolus-tracking technique.

CT and CTA images were sent to a workstation and bone was removed automatically within three minutes using the MMBE technique. CTA scans with masked bone were further processed in standardized MIP images: 40 images of different viewing angles rotated in a vertical and horizontal axis (Fig. 1d).[8,30]

After creation of a volume of interest, additional MIP images were made without venous structures.
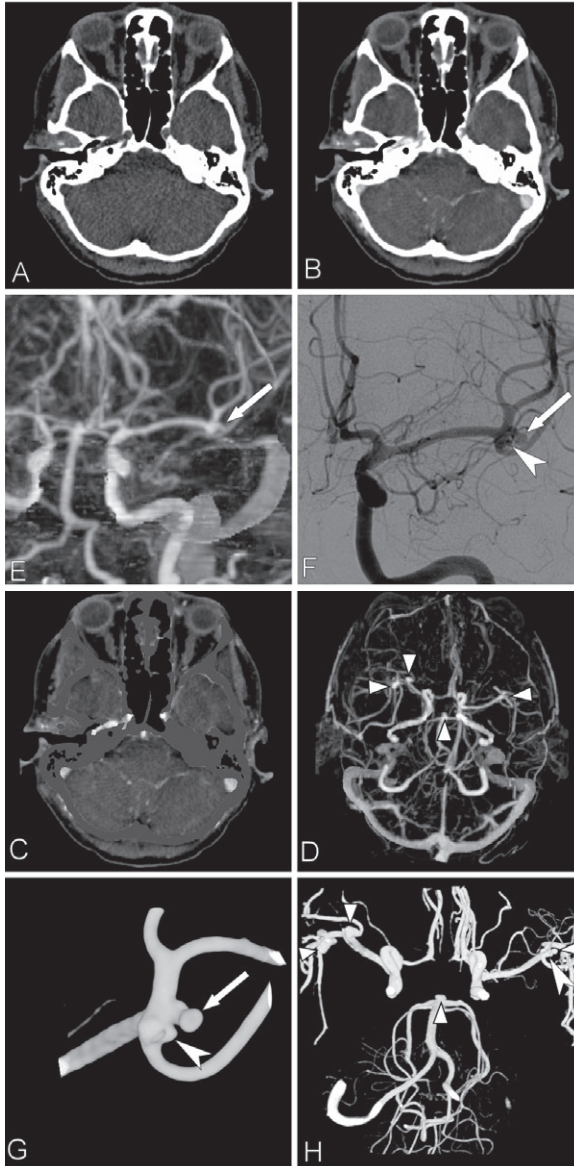
Fig. 1

Illustration of a MMBE procedure in a 44-year-old woman with a ruptured right middle cerebral artery (MCA) aneurysm.

A, B and **C**, Axial images of nonenhanced low-dose CT , CTA and CTA after MMBE.

D, Axial maximum intensity projection (MIP) obtained after MMBE shows two right MCA aneurysms, one left MCA aneurysm and a basilar tip aneurysm (triangles).

E, Coronal MIP image of left MCA shows 2.8 mm MCA aneurysm (arrow) and deceptive thickening of MCA bifurcation.

F, DSA shows the same aneurysm (arrow) as in **E**, with an additional, 1.6 mm MCA aneurysm (arrowhead).

G, 3DRA more clearly shows both MCA aneurysms (arrow and arrowhead).

H, Composite image of three 3DRA of both internal carotid arteries and right vertebral artery shows all 5 aneurysms (triangles and arrowhead).

DSA and 3DRA was performed by an experienced neuroradiologist on a single-plane angiographic unit (Integris Allura Neuro; Philips Medical Systems, Best, The Netherlands). Most angiograms were performed with the patient under general anaesthesia prior to coiling. Through a 6F catheter positioned in an internal carotid artery (ICA) or vertebral artery, 6-8 ml non-ionic contrast was injected and filming was done in 2-3 projections at a frame rate of 2/sec. For 3DRA, 100 images were acquired during a 240º rotational run in 8 seconds with 15-21 ml contrast medium at 3 ml/sec. On a dedicated workstation, 3D images were constructed and evaluated. Screen shots in multiple projections of volume rendered 3D images were stored.

III. IMAGE EVALUATION

III.A. CTA-MMBE

For the purpose of this study, CTA source images and MIP images were anonymized and evaluated, independently, by two neuroradiologists, blinded to clinical data, diagnostic CT and DSA results. CTA-MMBE image quality was rated as "good", "fair", "moderate" or "poor" and extent of bone removal as "complete", "near complete" or "incomplete". Near complete bone removal was defined as presence of tiny bone remnants or small calcifications (Fig. 2a and b). Bone removal was incomplete when large bone remnants were present. Both readers recorded reasons for moderate or poor image quality. Twenty-seven predefined locations, subdivided into four subgroups needed to be observed by each observer (Table I). These 27 predefined locations were evaluated in all patients, resulting in the observation of 2916 locations in total. For interobserver discrepancies in detection of aneurysms, consensus was reached.
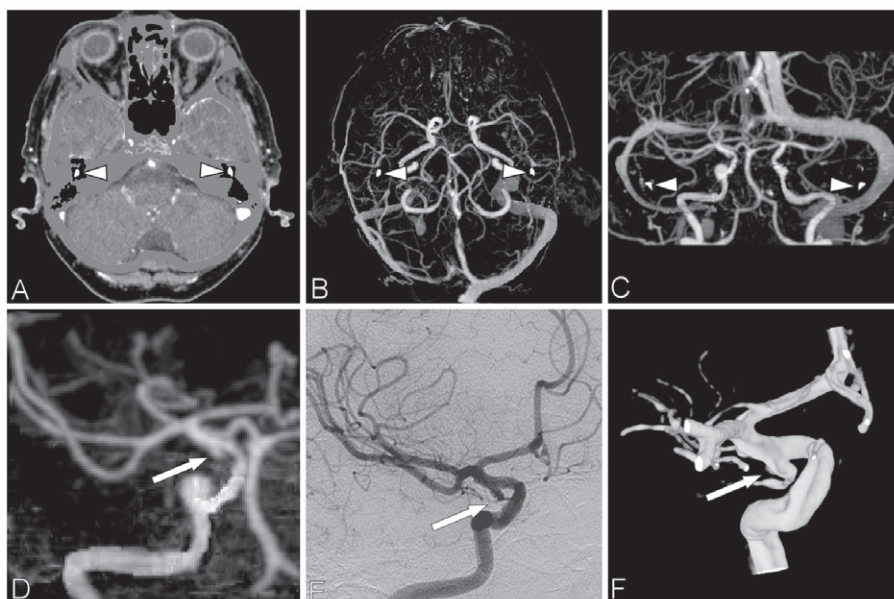
Fig. 2

77-year-old woman with subarachnoid hemorrhage and false-positive aneurysm finding on CTA.

A, Axial CTA-MMBE image shows complete bone removal of skull base structures, except from the auditory ossicles (triangles).

B and C, Axial maximum intensity projection (MIP) and coronal MIP with small bone remnants of auditory ossicles (triangles), which do not hinder evaluation.

D, Coronal MIP of a volume of interest with a small bulge of the right internal carotid interpreted as a small aneurysm (arrow). This infundibulum was mistaken for an aneurysm, because the posterior communicating artery is not visible.

E and F, DSA and 3DRA show infundibulum of small posterior communicating artery (arrow).

III.B. DSA AND 3DRA

DSA images in combination with screen shots of 3DRA, if available, were used as reference standard.[26,27] Images were re-evaluated by an experienced interventional neuroradiologist. The observer needed to evaluate all visible locations from the 27 predefined locations, which depended on the number of vessels catheterized. Aneurysm size as measured on 3DRA was recorded. If 3DRA was not available, aneurysm size was estimated from comparison with the internal carotid artery (4 mm) or basilar artery (3 mm). Finally, rupture status of the aneurysm, derived from all image modalities was assessed.

With DSA, 2188 of 2916 possible predefined aneurysm locations (75 %) in 108 patients could be re-evaluated. 3DRA was available in 784 of 2188 locations (36%).

III.C. STATISTICAL ANALYSIS

Diagnostic accuracy of CTA-MMBE was calculated for 2188 locations observed with both DSA and CTA. Sensitivity, specificity, positive predictive value (PPV), negative predictive value (NPV) and exact two-sided 95% confidence intervals (CI) were calculated for aneurysm detection.[31] Diagnostic accuracy was also calculated per patient, per aneurysm size, per observed location and per aneurysm location in four subgroups. Interobserver variability with percentages of agreement was calculated with κ statistics with κ ≥ 0.80 defined as excellent agreement, κ 0.60-0.79 as good agreement, κ 0.40-0.59 as moderate agreement, κ 0.20-0.39 as fair agreement and κ 0-0.19 as slight agreement. McNemar test was used to verify whether significant differences between observers and consensus of CTA-MMBE were present on aneurysm detection.

IV. RESULTS

IV.A. DSA AND 3DRA EVALUATIONS

In 88 of 108 patients (81%), 117 aneurysms (82 ruptured, 35 unruptured) were detected on DSA and 3DRA. In 20 patients no aneurysms were found. A single aneurysm was detected in 66 patients, two aneurysms in 17 patients, three aneurysms in four patients and five aneurysms in one patient. Aneurysm locations are listed in Table I. Mean aneurysm size was 5.9 mm (median 5, range 1-16 mm). Of 117 detected aneurysms, 16 were < 3 mm, 50 were 3-5.9 mm, 36 were 6-10 mm and 15 were > 10 mm.

Table I
Number of detected aneurysms on DSA and 3DRA on 27 predefined aneurysm locations in 4 subgroups.

Subgroup	Location	Number of aneurysms
Anterior cerebral artery	Anterior communicating artery	32
	Pericallosal artery	4
Internal carotid artery	Internal carotid artery tip	3
	Internal carotid artery other locations	8
	Posterior communicating artery	20
Middle cerebral artery	M1 segment	7
	M2 segment	3
	Bifurcation	21
Posterior circulation	Anterior inferior cerebellar artery	0
	Basilar tip	8
	Basilar trunk	2
	Posterior cerebral artery	1
	Posterior inferior cerebellar artery	4
	Superior cerebellar artery	3
	Vertebral artery	1
Total		117

Note.– DSA indicates digital subtraction angiography; 3DRA three dimensional rotational angiography; All locations were left and right, except for the anterior communicating artery, basilar trunk and basilar tip, resulting in 27 predefined locations.

IV.B. CTA EVALUATIONS

Overall CTA-MMBE image quality and extent of bone removal evaluation for both observers is listed in Table II. Reasons for poor or moderate image quality or incomplete bone removal (15 patients) were patient movement during scanning (8 patients) and insufficient arterial contrast combined with overprojecting venous structures (7 patients).

Overall diagnostic performance of CTA-MMBE for detection of intracranial aneurysms is listed in Table III, diagnostic performance per aneurysm subgroup location in Table IV and diagnostic performance according to aneurysm size in Table V.

With CTA-MMBE, observer A detected 102 of 117 aneurysms (87%) (79 ruptured, 23 unruptured) and observer B 103 (88%) (80 ruptured, 23 unruptured). After consensus, 11 aneurysms (9%) (1 ruptured, 10 unruptured) remained undetected. Observer A found one false-positive finding and observer B found five false-positive findings: after consensus three false-positive findings remained. The false-positive finding of observer A proved to be cavernous sinus enhancement, the five false-positive findings of observer B were three infundibula (Fig. 2c and d), one internal carotid artery loop and one local thickening of the pericallosal artery. Sensitivity for detecting aneurysms ≥ 3 mm was 0.99 and for aneurysms < 3 mm sensitivity was 0.38.

Characteristics of 11 aneurysms undetected after consensus with reasons for missing are listed in Table VI. Ten of 11 missed aneurysms were ≤ 2.5 mm and were additional unruptured aneurysms in patients harboring multiple aneurysms (see example in Fig. 1d-h). One missed aneurysm was a 4 mm ruptured dissecting posterior inferior cerebellar artery aneurysm on a poor quality CTA-MMBE due to patient movement. Another missed aneurysm was an 2.5 mm ophthalmic aneurysm, in direct contact with anterior clinoid process, which appeared smaller on MIP as compared to the non-masked CTA source images due to the applied MMBE technique and was therefore evaluated as irregularity of the ICA. Most missed aneurysms were located on the internal carotid artery (5 of 11) and consequently sensitivity for detection of aneurysms located on the internal carotid artery was significantly lower than for other subgroup locations (Table IV).

Interobserver agreement per aneurysm location and per patient was excellent (κ = 0.92 with 99% agreement per location and κ = 0.80 with 94% agreement per patient). Due to the high number of negative aneurysm locations, observer agreement per patient is the most representative value. McNemar's test showed no significant differences between observers for aneurysm detection per patient and per location and for observers and consensus.

Table II
Overall CTA image quality and quality of bone removal in 108 patients

Overall CTA image quality

	Observer A	Observer B
Good	80	92
Fair	22	11
Moderate	4	4
Poor	2	1

Quality of CTA-MMBE

	Observer A	Observer B
Complete	3	5
Near complete	98	101
Incomplete	7	2

Note.—CTA indicates CT angiography; MMBE matched mask bone elimination

Table III
Overall comparative diagnostic performance of CTA-MMBE

	Sensitivity	Specificity	PPV	NPV
Per patient				
Observer A	0.94 (83/88)	0.95 (19/20)	0.99 (83/84)	0.79 (19/24)
95% CI	0.87-0.98	0.75-1.00	0.93-1.00	0.59-0.91
Observer B	0.99 (87/88)	0.90 (18/20)	0.98 (87/89)	0.95 (18/19)
95% CI	0.93-1.00	0.69-0.98	0.92-1.00	0.74-1.00
Consensus	0.99 (87/88)	0.90 (18/20)	0.98 (87/89)	0.95 (18/19)
95% CI	0.93-1.00	0.69-0.98	0.92-1.00	0.74-1.00
Per location				
Observer A	0.87 (102/117)	1.00 (2070/2071)	0.99 (102/103)	0.99 (2070/2085)
95% CI	0.80-0.92	1.00-1.00	0.94-1.00	0.99-1.00
Observer B	0.88 (103/117)	1.00 (2066/2071)	0.95 (103/108)	0.99 (2066/2080)
95% CI	0.81-0.93	0.99-1.00	0.89-0.98	0.99-1.00
Consensus	0.91 (106/117)	1.00 (2068/2071)	0.97 (106/109)	0.99 (2068/2079)
95% CI	0.84-0.95	1.00-1.00	0.92-0.99	0.99-1.00

Note.– numbers between parentheses are aneurysms or locations. With DSA, 117 aneurysms were detected in 88 patients on 2188 predefined observed locations. CTA indicates CT angiography; MMBE matched mask bone elimination; PPV positive predictive value; NPV negative predictive value; CI confidence interval.

Table IV
Diagnostic performance of CTA according to aneurism location in subgroups

Location	Sensitivity	Specificity	PPV	NPV
Anterior cerebral artery	0.97 (35/36)	1.00 (81/81)	1.00 (35/35)	0.99 (81/82)
95% CI	0.81-0.99	0.95-1.00	0.88-1.00	0.93-1.00
Internal carotid artery	0.81 (25/31)	0.97 (83/86)	0.89 (25/28)	0.93 (83/89)
95% CI	0.63-0.91	0.90-0.99	0.72-0.97	0.86-0,97
Middle cerebral artery	0.90 (28/31)	1.00 (86/86)	1.00 (28/28)	0.97 (86/89)
95% CI	0.74-0.97	0.95-1.00	0.86-1.00	0.90-0.99
Posterior circulation	0.95 (18/19)	1.00 (98/98)	1.00 (18/18)	0.99 (98/99)
95% CI	0.74-1.00	0.95-1.00	0.79-1.00	0.94-1.00

Note.—numbers between parentheses are aneurysms. CTA indicates CT angiography; PPV positive predictive value; NPV negative predictive value; CI confidence interval.

Table V
Diagnostic performance of CTA according to aneurysm size.

Size	Sensitivity	PPV
< 3 mm	0.38 (6/16)	0.86 (6/7)
95% CI	0.18-0.61	0.57-0.99
3-5.9 mm	0.98 (49/50)	0.98 (49/50)
95% CI	0.89-1.00	0.89-1.00
6-10 mm	1.00 (36/36)	0.97 (36/37)
95% CI	0.89-1.00	0.85-1.00
> 10 mm	1.00 (15/15)	1.00 (15/15)
95% CI	0.76-1.00	0.76-1.00

Note.—numbers between parentheses are aneurysms; CTA indicates CT angiography.

Table VI
Retrospective evaluation of 11 aneurysms not detected with CTA-MMBE

Aneurysm location	Size (mm)	Visible in retrospect on CTA	main reason for missing aneurysm
Ophthalmic artery	2.5	Yes	Very small, in direct contact with bony structure (anterior clinoid process) and evaluated as irregularity of the ICA
ICA cavernous segment	2.0	Yes	Very small and poor quality of CTA
ICA supraclinoid segment	2.0	Yes	Very small and evaluated as part of multi lobulated aneurysm
ICA tip	1.8	No	Very small and poor quality of CTA
ICA tip	2.2	Yes	Very small
MCA	1.5	No	Very small and presence of vasospasm
MCA	2.0	Yes	Very small and only visible on one MIP image
MCA	1.6	Yes	Very small and evaluated as thickening of middle cerebral artery bifurcation
Pericallosal artery	2.0	Yes	Very small
PICA	4.0	Yes	Dissecting aneurysm, vasospasm and incomplete bone removal due to patient movement
PcomA	2.0	No	Very small and low arterial contrast

Note.— All except one were smaller than 3 mm. One 4 mm aneurysm was undetected due to poor quality CTA-MMBE. CTA indicates CT angiography; MMBE matched mask bone elimination; ICA internal carotid artery; MCA middle cerebral artery; PcomA posterior communicating artery; PICA posterior inferior cerebellar artery.

V. DISCUSSION

In this study, we found high sensitivities and specificities of CTA-MMBE for detection of intracranial aneurysms with excellent interobserver agreement. Only one small dissecting aneurysm out of 82 ruptured aneurysms was not detected due to poor quality CTA-MMBE by patient movement. Other undetected aneurysms were very small unruptured aneurysms additional to a detected ruptured aneurysm. As in other studies, several shortcomings of CTA-MMBE and MIP images leading to misinterpretation were apparent like difficulties in differentiating arterial loops or infundibula from aneurysms, (Fig. 2c and d), cavernous sinus contrast enhancement sometimes simulating or obscuring an aneurysm, and lack of depiction of very small aneurysms, especially located on the internal carotid artery.[9,10]

Our study design differs in some aspects from earlier published reports comparing CTA and DSA.[2,3,32-34] Since DSA and 3DRA do not necessarily include all vascular territories, analysis of results was performed per predefined anatomic aneurysm location and not per detected aneurysm. To minimize verification bias, we also included patients with no aneurysm found on DSA and CTA. To resemble clinical practice, low quality CTA studies were not discarded. We used high quality DSA and 3DRA as reference standard (most angiograms were performed in patients under general anaesthesia) and consequently aneurysms as small as 1-2 mm were easily detected (Fig. 1g). This may partly explain the relatively low sensitivity in this study for these very small intracranial aneurysms.

Since our study design differs in analysis and calculation methods, comparison with other studies is of limited value. For instance, in another study with comparable number of patients, higher sensitivity for detection of aneurysms was reported (0.95 versus 0.91), but small aneurysms located on the internal carotid artery were excluded.[4] In general, results of this study are in concordance with two meta-analyses.[26,27]

One could suspect that the relatively low sensitivity for small aneurysms could be attributed to the MMBE technique. However, of 11 missed aneurysms, only one 2.5 mm (ophthalmic) aneurysm was directly adjacent to a bony structure. This aneurysm appeared smaller on MIP as compared to the non-masked CTA source

images due to the applied MMBE technique. All other missed aneurysms were not directly adjacent to bone, so MMBE could be excluded as a cause of missing.

Our results and those of others suggest that complete DSA is no longer mandatory as a diagnostic tool in patients with good quality CTA. Only in patients with confirmed SAH and poor quality CTA, complete diagnostic DSA should be performed. Detection of a ruptured aneurysm with CTA can be followed by selective DSA of the vessel harboring the aneurysm prior to endovascular treatment, thereby reducing complication risk and procedural time. If this strategy would be applied to the present study population, only very small additional unruptured aneurysms would go undetected. The rupture risk of very small additional aneurysms is extremely low.[35]

Since undetected small aneurysms may grow with time, however, a follow up strategy in patients with coiled intracranial aneurysms should consist of after 6 months DSA of the vessel harboring the aneurysm and MRA at a later date, for example after 12-18 months and possibly yearly thereafter. With this strategy, growing initially undetected small aneurysms or de novo aneurysms will be timely detected. Patients with clipped aneurysms can be followed with CTA, especially when titanium clips were used.[36-38]

Manual bone editing in CTA is time-consuming (approximately 20 minutes), user dependent and requires knowledge of vascular anatomy.[8,18] In contrast, MMBE for bone removal is fully automatic and user independent. MMBE removed bone adequately in all patients with good or fair quality CTA examinations with only insignificant small remnants of bone or calcifications (Fig. 2a and b). When CTA examinations were of moderate or poor quality, also CTA-MMBE and MIP images were of lower quality. Main causes for reduced CTA image quality were patient movement during scanning, insufficient arterial contrast and overprojection of veins.

In case of patient movement during scanning, the incomplete bone removal was restricted to slice positions at which movement occurred.

The question whether MMBE has additional value in aneurysm detection remains unanswered in this study since we did not compare CTA-MMBE with a standard CTA technique. Subjectively however, MMBE offers easier and quicker viewing of reconstructed images without hindering bony structures. Average reading-time per case was approximately 10 minutes, which is shorter than other

CTA reading-times reported (15-20 minutes).[39,40]

The use of 16- or 64-slice CT scanners with shorter scan times, thinner slices and volume rendered image display, will improve image quality of CTA. This may lead to higher sensitivity for detection of very small aneurysms and improved evaluation of aneurysm characteristics to assess the mode of treatment (surgery or endovascular).

VI. CONCLUSION

CTA-MMBE is an accurate imaging technique for detection of intracranial aneurysms allowing rapid aneurysm visualization on MIP images in any projection without overprojecting bone, in a fully automatic and operator independent way. CTA-MMBE has limited sensitivity in detecting aneurysms < 3 mm with the use of 4-slice CT scanners. Our data suggest that, after detection of a ruptured aneurysm with CTA, DSA and 3DRA can be limited to the vessel harboring the ruptured aneurysm prior to endovascular treatment.

REFERENCES

1   C.Kouskouras, A. Charitanti, C. Giavroglou, N. Foroglou, P. Selviaridis, V. Kontopoulos, and A. S. Dimitriadis "Intracranial aneurysms: evaluation using CTA and MRA. Correlation with DSA and intraoperative findings", Neuroradiology 46 (10), 842-850 (2004).

2   D.Y.Yoon, K. J. Lim, C. S. Choi, B. M. Cho, S. M. Oh, and S. K. Chang "Detection and Characterization of Intracranial Aneurysms with 16-Channel Multidetector Row CT Angiography: A Prospective Comparison of Volume-Rendered Images and Digital Subtraction Angiography", AJNR Am J Neuroradiol 28 (1), 60-67 (2007).

3   M.T.Karamessini, G. C. Kagadis, T. Petsas, D. Karnabatidis, D. Konstantinou, G. C. Sakellaropoulos, G. C. Nikiforidis, and D. Siablis "CT angiography with three-dimensional techniques for the early diagnosis of intracranial aneurysms. Comparison with intra-arterial DSA and the surgical findings", Eur.J.Radiol. 49 (3), 212-223 (2004).

4   B.L.Hoh, A. C. Cheung, J. D. Rabinov, J. C. Pryor, B. S. Carter, and C. S. Ogilvy "Results of a prospective protocol of computed tomographic angiography in place of catheter angiography as the only diagnostic and pretreatment planning study for cerebral aneurysms by a combined neurovascular team", Neurosurgery 54 (6), 1329-1340 (2004).

5   M.Teksam, A. McKinney, S. Casey, M. Asis, S. Kieffer, and C. L. Truwit "Multi-section CT angiography for detection of cerebral aneurysms", AJNR Am J Neuroradiol 25 (9), 1485-1492 (2004).

6   M.Matsumoto, M. Sato, M. Nakano, Y. Endo, Y. Watanabe, T. Sasaki, K. Suzuki, and N. Kodama "Three-dimensional computerized tomography angiography-guided surgery of acutely ruptured cerebral aneurysms", J.Neurosurg. 94 (5), 718-727 (2001).

7   S.Imakita, Y. Onishi, T. Hashimoto, S. Motosugi, S. Kuribayashi, M. Takamiya, N. Hashimoto, T. Yamaguchi, and T. Sawada "Subtraction CT angiography with controlled-orbit helical scanning for detection of intracranial aneurysms", AJNR Am J Neuroradiol 19 (2), 291-295 (1998).

8   B.K.Velthuis, M. S. van Leeuwen, T. D. Witkamp, S. Boomstra, L. M. Ramos, and G. J. Rinkel "CT angiography: source images and postprocessing techniques in the detection of cerebral aneurysms", AJR Am J Roentgenol 169 (5), 1411-1417 (1997).

9   E.K.Fishman, D. R. Ney, D. G. Heath, F. M. Corl, K. M. Horton, and P. T. Johnson "Volume rendering versus maximum intensity projection in CT angiography: what works best, when, and why", Radiographics 26 (3), 905-922 (2006).

10 B.F.Tomandl, N. C. Kostner, M. Schempershofe, W. J. Huk, C. Strauss, L. Anker, and P. Hastreiter "CT angiography of intracranial aneurysms: a focus on postprocessing", Radiographics 24 (3), 637-655 (2004).

11 M.V.Jayaraman, W. W. Mayo-Smith, G. A. Tung, R. A. Haas, J. M. Rogg, N. R. Mehta, and C. E. Doberstein "Detection of intracranial aneurysms: multi-detector row CT angiography compared with DSA", Radiology 230 (2), 510-518 (2004).

12 J.P.Villablanca, N. Martin, R. Jahan, Y. P. Gobin, J. Frazee, G. Duckwiler, J. Bentson, M. Hardart, D. Coiteiro, J. Sayre, and F. Vinuela "Volume-rendered helical computerized tomography angiography in the detection and characterization of intracranial aneurysms", J.Neurosurg. 93 (2), 254-264 (2000).

13 J.P.Villablanca, R. Jahan, P. Hooshi, S. Lim, G. Duckwiler, A. Patel, J. Sayre, N. Martin, J. Frazee, J. Bentson, and F. Vinuela "Detection and characterization of very small cerebral aneurysms by using 2D and 3D helical CT angiography", AJNR Am.J.Neuroradiol. 23 (7), 1187-1198 (2002).

14 E.K.Fishman, C. C. Liang, B. S. Kuszyk, S. E. Davi, D. G. Heath, D. Hentschel, S. V. Duffy, and A. Gupta "Automated bone editing algorithm for CT angiography: preliminary results", AJR Am J Roentgenol 166 (3), 669-672 (1996).

15 M.Fiebich, C. M. Straus, V. Sehgal, B. C. Renger, K. Doi, and K. R. Hoffmann "Automatic bone segmentation technique for CT angiographic studies", J.Comput.Assist.Tomogr. 23 (1), 155-161 (1999).

16 S.O.Casey, R. A. Alberico, M. Patel, J. M. Jimenez, R. R. Ozsvath, W. M. Maguire, and M. L. Taylor "Cerebral CT venography", Radiology 198 (1), 163-170 (1996).

17 J.Beier, H. Oellinger, C. S. Richter, E. Fleck, and R. Felix "Registered image subtraction for CT-, MR- and coronary angiography", Eur.Radiol. 7 (1), 82-89 (1997).

18 R.B.Schwartz, H. M. Tice, S. M. Hooten, L. Hsu, and P. E. Stieg "Evaluation of cerebral aneurysms with helical CT: correlation with conventional angiography and MR angiography", Radiology 192 (3), 717-722 (1994).

19 S.Sakamoto, Y. Kiura, M. Shibukawa, S. Ohba, K. Arita, and K. Kurisu "Subtracted 3D CT angiography for evaluation of internal carotid artery aneurysms: comparison with conventional digital subtraction angiography", AJNR Am J Neuroradiol 27 (6), 1332-1337 (2006).

20 H.W.Venema, F. J. Hulsmans, and G. J. den Heeten "CT angiography of the circle of Willis and intracranial internal carotid arteries: maximum intensity projection with matched mask bone elimination-feasibility study", Radiology 218 (3), 893-898 (2001).

21 C.B.Majoie, M. van Straten, H. W. Venema, and G. J. den Heeten "Multisection CT venography of the dural sinuses and cerebral veins by using matched mask bone elimination", AJNR Am J Neuroradiol 25 (5), 787-791 (2004).

22 M.van Straten, H. W. Venema, G. J. Streekstra, C. B. Majoie, G. J. den Heeten, and C. A. Grimbergen "Removal of bone in CT angiography of the cervical arteries by piecewise matched mask bone elimination", Med.Phys. 31 (10), 2924-2933 (2004).

23 R.Anxionnat, S. Bracard, X. Ducrocq, Y. Trousset, L. Launay, E. Kerrien, M. Braun, R. Vaillant, F. Scomazzoni, A. Lebedinsky, and L. Picard "Intracranial aneurysms: clinical value of 3D digital subtraction angiography in the therapeutic decision and endovascular treatment", Radiology 218 (3), 799-808 (2001).

24 T.Sugahara, Y. Korogi, K. Nakashima, S. Hamatake, S. Honda, and M. Takahashi "Comparison of 2D and 3D digital subtraction angiography in evaluation of intracranial aneurysms", AJNR Am J Neuroradiol 23 (9), 1545-1552 (2002).

25 S.Tanoue, H. Kiyosue, H. Kenai, T. Nakamura, M. Yamashita, and H. Mori "Three-dimensional reconstructed images after rotational angiography in the evaluation of intracranial aneurysms: surgical correlation", Neurosurgery 47 (4), 866-871 (2000).

26 E.T.Chappell, F. C. Moure, and M. C. Good "Comparison of computed tomographic angiography with digital subtraction angiography in the diagnosis of cerebral aneurysms: a meta-analysis", Neurosurgery 52 (3), 624-631 (2003).

27 P.M.White, J. M. Wardlaw, and V. Easton "Can noninvasive imaging accurately depict intracranial aneurysms? A systematic review", Radiology 217 (2), 361-370 (2000).

28 R.A.Willinsky, S. M. Taylor, K. TerBrugge, R. I. Farb, G. Tomlinson, and W. Montanera "Neurologic complications of cerebral angiography: prospective analysis of 2,899 procedures and review of the literature", Radiology 227 (2), 522-528 (2003).

29 H.J.Cloft, G. J. Joseph, and J. E. Dion "Risk of cerebral angiography in patients with subarachnoid hemorrhage, cerebral aneurysm, and arteriovenous malformation: a meta-analysis", Stroke 30 (2), 317-320 (1999).

30 S.Napel, M. P. Marks, G. D. Rubin, M. D. Dake, C. H. McDonnell, S. M. Song, D. R. Enzmann, and R.

B. Jeffrey, Jr. „CT angiography with spiral CT and maximum intensity projection", Radiology 185 (2), 607-610 (1992).

31 A.Agresti and B. A. Coull „Approximate is better than „exact" for interval estimation of binomial proportions", The American Statistician 52 (2), 119-126 (1998).

32 J.P.Villablanca, A. Achiriolaie, P. Hooshi, N. Martin, G. Duckwiler, R. Jahan, J. Frazee, P. Gobin, J. Sayre, and F. Vinuela „Aneurysms of the posterior circulation: detection and treatment planning using volume-rendered three-dimensional helical computerized tomography angiography", J.Neurosurg. 103 (6), 1018-1029 (2005).

33 C.Y.Chen, S. C. Hsieh, W. M. Choi, P. Y. Chiang, J. C. Chien, and W. P. Chan „Computed tomography angiography in detection and characterization of ruptured anterior cerebral artery aneurysms at uncommon location for emergent surgical clipping", Clin.Imaging 30 (2), 87-93 (2006).

34 Y.Korogi, M. Takahashi, K. Katada, Y. Ogura, K. Hasuo, M. Ochi, H. Utsunomiya, T. Abe, and S. Imakita „Intracranial aneurysms: detection with three-dimensional CT angiography with volume rendering--comparison with conventional angiographic and surgical findings", Radiology 211 (2), 497-506 (1999).

35 M.J.Wermer, d. S. van, I, A. Algra, and G. J. Rinkel „Risk of rupture of unruptured intracranial aneurysms in relation to patient and aneurysm characteristics: an updated meta-analysis", Stroke 38 (4), 1404-1410 (2007).

36 I.Sakuma, N. Tomura, H. Kinouchi, S. Takahashi, T. Otani, J. Watarai, and K. Mizoi „Postoperative three-dimensional CT angiography after cerebral aneurysm clipping with titanium clips: detection with single detector CT. Comparison with intra-arterial digital subtraction angiography", Clin. Radiol. 61 (6), 505-512 (2006).

37 H.J.Steiger and J. J. van Loon „Virtues and drawbacks of titanium alloy aneurysm clips", Acta Neurochir.Suppl 72 , 81-88 (1999).

38 I.van der Schaaf, B. K. Velthuis, M. J. Wermer, N. J. Frenkel, C. B. Majoie, T. D. Witkamp, G. de Kort, N. J. Freling, and G. J. Rinkel „Multislice computed tomography angiography screening for new aneurysms in patients with previously clip-treated intracranial aneurysms: Feasibility, positive predictive value, and interobserver agreement", J.Neurosurg. 105 (5), 682-688 (2006).

39 M.El Khaldi, P. Pernter, F. Ferro, A. Alfieri, N. Decaminada, L. Naibo, and G. Bonatti „Detection of cerebral aneurysms in nontraumatic subarachnoid haemorrhage: role of multislice CT angiography in 130 consecutive patients", Radiol.Med.(Torino) 112 (1), 123-137 (2007).

40 M.Wintermark, A. Uske, M. Chalaron, L. Regli, P. Maeder, R. Meuli, P. Schnyder, and S. Binaghi „Multislice computerized tomography angiography in the evaluation of intracranial aneurysms: a comparison with intraarterial digital subtraction angiography", J.Neurosurg. 98 (4), 828-836 (2003).

4

Interobserver variability in the detection of cerebral venous thrombosis using CT venography with matched mask bone elimination

Hugo A.F. Gratama van Andel, Leonard J. van Boven , Marianne A. van Walderveen,
Henk W. Venema, Jeroen C. van Rijn, Jan Stam, Cornelis A. Grimbergen,
Gerard J. den Heeten and Charles B.L.M. Majoie

ABSTRACT

Computed tomography venography (CTV) has proven to be a reliable imaging method in the evaluation of cerebral venous thrombosis with good correlation to magnetic resonance (MR) imaging and digital subtraction angiography (DSA). It is fast and widely accessible, especially in the emergency setting. For better visualization of vascular structures bone is often removed from the images. The purpose of this study was to evaluate the quality of a fully automatic bone removal method, matched mask bone elimination (MMBE), and to asses the interobserver variability of the CTV technique.

Fifty patients with clinical suspicion of cerebral venous thrombosis underwent multislice CTV with MMBE postprocessing. Axial source images and maximum intensity projections were retrospectively evaluated by two neuroradiologists for quality of bone removal and for the presence or absence of thrombosis in 9 dural sinuses and 5 deep cerebral veins. A per sinus/vein and a per patient analysis (thrombosis in at least one sinus or vein) was performed and interobserver agreement was assessed.

Both observers considered bone removal good in all patients (100%). Interobserver agreement per patient was excellent ($\kappa = 0.83$), with a full agreement in 47 of 50 patients (94%). The interobserver agreement per sinus or vein was good ($\kappa = 0.76$), with a full agreement in 679 of 700 sinuses or veins (97%).

CTV aided with MMBE is a robust technique for visualization of the intracranial venous circulation, removing bone effectively. CTV has high interobserver agreement for presence or absence of cerebral venous thrombosis.

I. INTRODUCTION

Thrombosis of cerebral veins and sinuses is a rare condition, comprising less than 1% of all strokes,[1] that most often affects young woman.[2] The symptoms and clinical course are highly variable, and, despite improvements in diagnosis and treatment, it may still cause death or permanent disability.[3] Prompt accurate diagnosis is essential to determine the need for antithrombotic therapy or local thrombolysis.[2,4]

Magnetic resonance imaging (MRI) together with magnetic resonance venography (MRV) is considered a sensitive non-invasive examination technique for the diagnosis of cerebral venous thrombosis.[5] However, MRI has limited application in the evaluation of cerebral venous thrombosis due to its infrequent availability in the acute care setting, longer imaging time, and technique related artifacts leading to spurious interpretation.[6,7]

Previous reports have noted that CT venography (CTV) has a high sensitivity for detection of cerebral venous thrombosis as compared to digital subtraction angiography (DSA).[7,8] CTV is superior in the identification of cerebral veins and dural sinuses and is at least equivalent in establishing the diagnosis of dural sinus thrombosis as compared to MRV.[8-10] CTV can provide a rapid and reliable diagnosis in the acute setting allowing prompt therapy.[7-12]

Since the seminal article of Casey et al in 1996,[11] who introduced CTV as a diagnostic tool, bone removal techniques have been used in most studies to obtain three dimensional (3D) views on the venous vasculature without hindrance of bone.[6,7,13] Nearly all studies have used the 'graded subtraction' technique,[11] that removes bone by interactive thresholding and region growing.[8,10,12,14] A drawback of this technique is that it is operator dependent and time consuming. Other techniques without these drawbacks have been developed, using an additional low-dose nonenhanced scan.[15-18]

In the present study, matched mask bone elimination (MMBE) was chosen for bone removal, because of its user-independent and fully automatic nature.[15,19-21] The interobserver variability is of course an important characteristic of a diagnostic tool. The number of studies that report on the interobserver agreement in CTV is limited, however, and in these studies only a restricted number of patients (10 to less than twenty) were included.[9,11,12]

The purpose of the present study was therefore to determine quality of bone

removal with MMBE and to evaluate interobserver variability in detection of cerebral venous thrombosis of CTV using MMBE in a large number of patients.

II. PATIENTS AND METHODS

II.A. PATIENTS AND IMAGING

All patients with clinical suspicion of cerebral venous thrombosis that underwent multislice CTV with MMBE post-processing from March 2003 until February 2006 were identified with a database search. Fifty patients, 16 men and 34 women, were identified with a mean age of 36 years, in the range of 17 months to 82 years. In all patients, two spiral CT scans, the first one low-dose and nonenhanced and the second contrast-enhanced, of the head were made from the vertex to C1, resulting in a scan length of approximately 15 cm.

Twelve patients were scanned with the Mx8000 (Philips Medical Systems, Best, Netherlands) and 38 patients with the Sensation 4 (Siemens Medical Solutions, Erlangen, Germany), both with 4 x 1 mm collimation. With the Mx8000 90 kV was used; 100 and 360 effective mAs, a rotation time of 0.75 s and a pitch of 0.875. With the Sensation 4 120 kV was used; 65 and 250 effective mAs, a rotation time of 0.5 s and a pitch of 0.85. Scans were reconstructed with a nominal field of view of 220 mm, an effective slice thickness of 1.3 mm, and a slice increment of 0.5 mm, 180° interpolation and reconstruction-kernel B (Philips) or H30f (Siemens).

Non-ionic contrast material (Omnipaque [Iohexol] containing 300 mg of iodine per milliliter; Nycomed, Oslo, Norway) was injected in a cubital vein at 4 ml/s for a total of 120 ml. Scanning was started after a delay time of 25 s. In most scans the gantry was angulated. The duration of one helical CT scan was approximately 22 seconds with the Sensation 4 and approximately 32 seconds with the Mx8000.

II.B. POST-PROCESSING

After acquisition, MMBE was applied. The principle of the MMBE method is that bone voxels are identified in the nonenhanced scan, and that corresponding

voxels in the enhanced scan are given an arbitrarily low value[19] (Fig. 1). Key step in the MMBE procedure is compensation for movements of the patient in between the two scans. Even minimal movements lead to serious artifacts in the processed images if not compensated. This compensation was achieved by registration of the nonenhanced CT scan with the contrast-enhanced CT scan. After registration, a threshold was applied to identify bone voxels in the nonenhanced scan. In scans made at 90 and 120 kV these threshold were 200 HU and 150 HU, respectively.[15] The mask was slightly dilated by means of 1 voxel to allow for partial volume effects and slight amounts of mismatch. Processing for the complete MMBE procedure took slightly more than 10 minutes. Post-processing of the scans with MMBE was performed fully automatic on a framework for automatic image processing and routing using GRID-computing.[22] After processing the images were cached and routed to a workstation (MxView; Philips Medical Systems, Best, Netherlands), where 40 maximum intensity projection (MIP) images free from overprojecting bone were made from standardized angles.
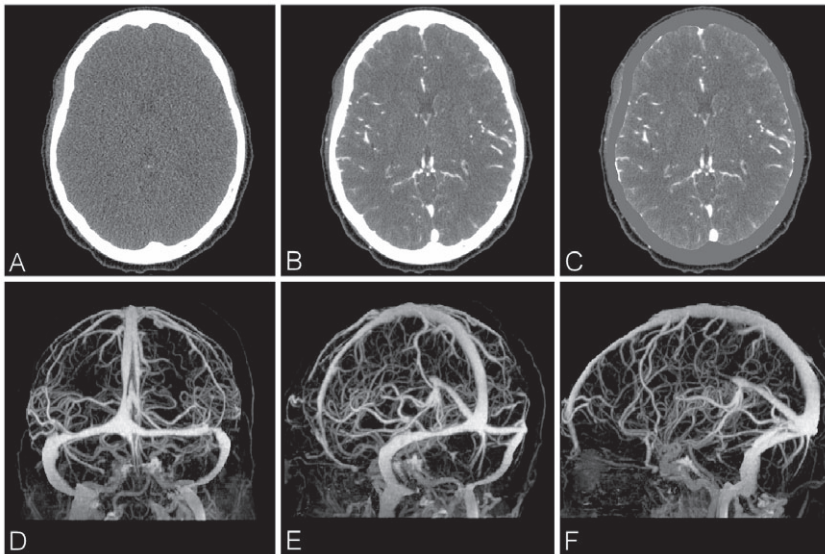
Fig. 1
CT Venography of a 34-year old woman with clinical suspicion of cerebral venous thrombosis demonstrates complete bone removal and normal appearance of the intracranial venous circulation. The scan was made at 90 kV and the enhancement in the confluence of sinuses and superior sagittal sinuses was 500 HU and 381 HU, respectively. The ratio SSS-CFS was 0.76. (A) (B) and (C) axial images of nonenhanced low-dose CT, CTV and CTV after MMBE. (D), (E) and (F) MIPs of the CTV dataset after MMBE in anteroposterior, left-posterior oblique and lateral direction.

II.C. IMAGE EVALUATION

Measurements were made on the images by a medical physicist to quantify contrast enhancement in the veins. The CTV examinations were evaluated by two neuroradiologists on quality of the scan, quality of bone removal and for presence or absence of thrombosis. The observers were blinded from the findings of each other and from previous patient findings except from the fact that the CTV examination was performed because of suspicion of cerebral venous thrombosis. The observers were provided with original CTV images, nonenhanced images, processed CTV images with masked bone and standardized MIP images.

II.D. MEASUREMENTS OF CONTRAST ENHANCEMENT

The contrast enhancement of the scans was quantified by determining the maximal CT-value in two regions of interest (ROIs), one containing the superior sagittal sinus (SSS) and the other containing the confluence of sinuses (CFS). The measurements were performed in masked CTV scans. To reduce the influence of noise all the CT-values were averaged over a volume of 3 x 3 x 3 voxels. The first ROI consisted of a sphere with a diameter of 3 cm centered at the confluence of sinuses; the other ROI was a disk-shaped volume with a diameter of 6 cm centered at the vertex of the skull, with a depth of 8 mm in the brain contiguous to the crown of the skull. The enhancement, i.e., the difference in CT-values between the enhanced and nonenhanced scan, was obtained by subtracting 50 HU, the average CT-value of a nonenhanced vein, from the measured maximal CT values.

To quantify the distribution of the contrast agent throughout the scan we computed also the ratio of the enhancement in the superior sagittal sinus and the confluence of sinuses (ratio SSS-CFS). This ratio is an indication of the timing of the scan after bolus injection. A ratio SSS-CFS substantially larger than one indicates that the delay time may have been too long, as the enhancement appears to be maximal at the start of the scan at the vertex and is considerably reduced when the level of the confluence of sinuses is reached. A ratio SSS-CFS substantially lower than one indicates that the delay time may have been too short, or that an extensive thrombus is present in the region of the superior sagittal sinus.

II.E. QUALITY OF IMAGES AND BONE REMOVAL

Quality of CTV-images was categorized as excellent, moderate or poor. The quality of the scan was moderate if some movement of the patient had occurred that did not interfere with image interpretation. The quality was poor if either patient movement or technical problems (e.g. poor contrast) interfered with interpretation of the images. For statistical analysis, data were dichotomized as good quality (excellent or moderate) and poor quality.

Quality of bone removal was categorized as complete, nearly complete or incomplete. If small osseous structures or calcifications (e.g. auditory ossicles, bone lamellae of mastoid or nasal sinus and falx, pineal gland or choroid plexus calcifications) were visible not interfering with interpretation of the venous structures, bone removal was judged as nearly complete. If many osseous structures were still visible, interfering with interpretation, the bone removal was considered as incomplete. For statistical analysis, data were dichotomized as good bone removal (complete or nearly complete) and poor bone removal (incomplete).

II.F. ASSESSMENT OF THROMBOSIS

A total of 9 dural sinuses (superior sagittal sinus, bilateral transverse, sigmoid and cavernous sinuses, inferior sagittal sinus and straight sinus) and 5 cerebral veins (bilateral internal cerebral veins and basal veins and vein of Galen) were evaluated for thrombosis. Other small venous structures such as the petrosal veins were not evaluated, because they were considered as less relevant. A sinus or vein could be evaluated as visualized, non-visualized, hypoplastic, completely thrombosed or partially thrombosed. A sinus or vein was considered as being non-visualized if neither a thrombus nor a sinus or vein was visualized. A patient was considered to have a cerebral venous thrombosis if at least one dural sinus or cerebral vein was partially or completely thrombosed.

A per sinus/vein and a per patient analysis was performed. To demonstrate interobserver variability κ statistics between observers and percentages of agreement were calculated. A κ value of $>= 0.80$ indicated excellent agreement; 0.60 -0.79 good agreement; 0.40-0.59 moderate agreement and 0.39-0.20 fair agreement and 0.0 -0.19 slight agreement.[23]

After the individual assessments, a consensus reading was performed in

which the scans of patients with sinuses and veins with disagreement between the observers were examined. Follow-up imaging and clinical follow-up information of these patients, if available, was used to assist the observers in the making of their final judgement.

III. RESULTS

III.A. CONTRAST ENHANCEMENT

The mean and range of contrast enhancement in the CTV scans at two locations and their ratio is shown for the forty patients without thrombosis (see below) in Table I. As expected enhancement at 90 kV is higher than at 120 kV.[24] At both kVs the ratio SSS-CFS is slightly less than one. In Fig. 2 the ratio is shown as a function of age. The results of scans at 90 and 120 kV are taken together as the ratio does not depend on the absolute enhancement. It can be seen that the ratio is lower in older patients. In addition in Fig. 2 the ratio is also shown for the ten patients with thrombosis (see below).

Table I
Enhancement at two locations and the ratio of the enhancements in 40 patients without thrombosis

Tube voltage (kV)	N	CFS (HU)	SSS (HU)	ratio SSS-CFS
120	29	281 (109-455)	233 (26-540)	0.88 (0.10-2.55)
90	11	413 (199-531)	345 (252-422)	0.88 (0.58-1.51)

Data are represented as mean (range). N, number of patients; CFS, confluence of sinuses; SSS, superior sagittal sinus; ratio SSS-CFS, the enhancement of the superior sagittal sinus divided by the enhancement of the confluence of sinuses
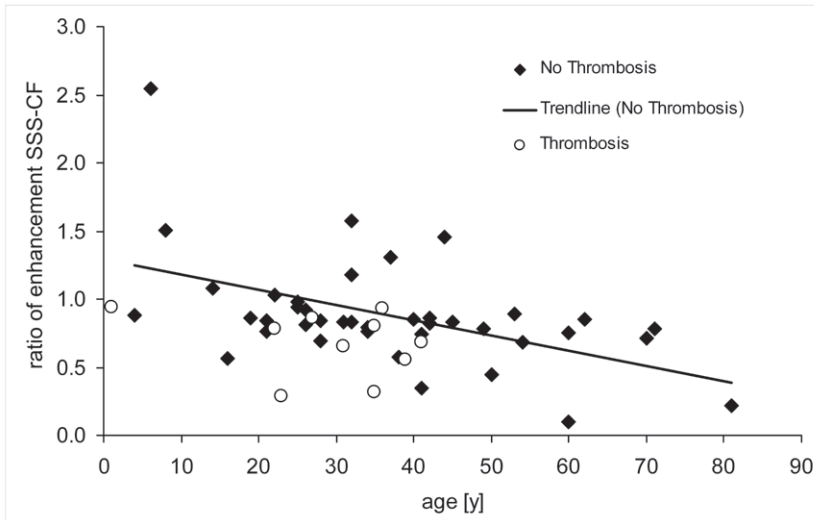
Fig. 2

This figure shows the ratio of the enhancement at two sites for 50 patients as a function of age. The ratio of enhancement is the contrast of the superior sagittal sinus (SSS), divided by the contrast the confluence of sinuses (CFS). For young patients this ratio is approximately 1 or higher, which means that the SSS has the same enhancement as the CFS or a higher enhancement. For older patients the opposite is the case. For patients with thrombosis (open symbols) the enhancement tends to be lower than for patients without thrombosis (closed symbols). A ratio higher than one is an indication that the scan is too late relative to the time of the contrast injection (the maximum enhancement of the CFS is already past at the moment the scan starts), a ratio lower than one indicates the opposite (enhancement of the CFS has not yet reached the maximal value at the time of the scan).

III.B. QUALITY OF IMAGES AND BONE REMOVAL

Observer I considered the quality of the CT scan excellent in 41 patients, moderate in 8 patients and poor in 1 patient. Observer II considered quality excellent in 28 patients, moderate in 21 patients and poor in 1 patient. The difference in categorizing a scan as good or as moderate between the observers was mainly caused by a more critical appraisal of the scans by observer II concerning the uniformity of contrast enhancement. The two scans that were rated "poor" were of different patients and both concerned scans in which the contrast had not yet reached the SSS when the scan was started. Overall quality of the CT scan was considered as "good" by both observers in 48 of 50 patients (96%). Artifacts caused by metal objects as clips or coils were present in only two patients and did not hinder the visualization of veins and sinuses.

Observer I considered bone removal to be complete in 38 patients and nearly

complete in 12 patients. Observer II considered bone removal also to be complete in 38 patients and nearly complete in 12 patients. In two patients one observer judged the bone removal as complete, the other as nearly complete. Overall bone removal was considered as "good" in all patients (100%) by both observers.

III.C. PER SINUS/VEIN ANALYSIS

CTV findings in the 50 patients are listed in Table II. A total number of 700 sinuses and veins were evaluated (14 sinuses/veins per patient, 50 patients). Interobserver agreement on presence or absence of thrombosis per sinuses or veins was good ($\kappa = 0.76$, 95% confidence interval (CI): 0.67-0.86; full agreement 97%: 679/700). The observers agreed on presence of thrombosis in 37 of 700 sinuses or veins (5.3%) (Table III; Fig. 3). There was disagreement in 21 sinuses or veins (3.0%). In 18 out of the 21 sinuses or veins (in 7 patients) with disagreement, no change in final diagnosis was observed. In these patients, the observers already agreed on 1 or more (partially) thrombosed sinuses or veins, so that the patient was considered as having cerebral venous thrombosis. Disagreement of 1 or more other sinuses or veins in these patients did not change the diagnosis. In most cases the superior sagittal sinus was considered as being thrombosed (Table II). Observer I scored 40 sinuses or veins (5.7%) as thrombosed and observer II 55 (7.9%). There was disagreement in presence or absence of thrombosis in 10 sinuses or veins of the deep venous system (all the veins and the straight sinus and inferior sagittal sinus) and in 11 larger dural sinuses (either superior sagittal, transverse or sigmoid sinuses). In these cases, disagreement was due to difference in interpretation, e.g., judged as hypoplastic vs. partially thrombosed or non-visualized vs. completely thrombosed, or to poor quality of the CT-scan. All patients with disagreement in judgment of deep venous system patency had also a thrombosed superior sagittal, transverse and/or sigmoid sinus.

Table II
CTV findings in 50 patients suspected of cerebral venous thrombosis

Vessel	Observer I		Observer II		Disagreement
	Normal	Thrombosis	Normal	Thrombosis	
Superior Sagittal Sinus	41	9	42	8	3
Left Transverse Sinus	47	3	44	6	3
Right Transverse Sinus	45	5	43	7	4
Left Sigmoid Sinus	47	3	46	4	1
Right Sigmoid Sinus	45	5	45	5	0
Straight Sinus	45	5	44	6	1
Inferior Sagittal Sinus	49	1	49	1	0
Left Cavernous Sinus	50	0	50	0	0
Right Cavernous Sinus	50	0	50	0	0
Vein of Galen	46	4	44	6	2
Left Internal Cerebral Vein	49	1	47	3	2
Right Internal Cerebral Vein	48	2	47	3	1
Left Basal Vein	49	1	47	3	2
Right Basal Vein	49	1	47	3	2
Total:	660	40	645	55	21

Data are dichotomized: visualized, non-visualized and hypoplastic are rated as normal; partially or completely thrombosed are rated as thrombosis. CTV, CT venography
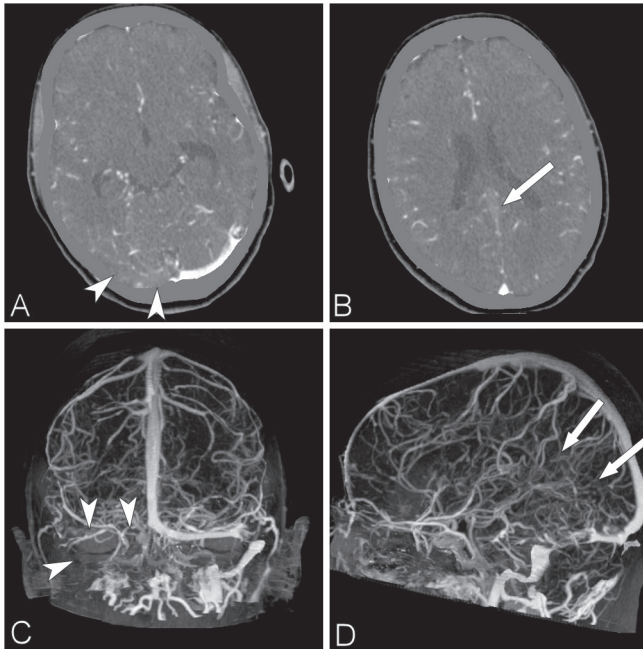
Fig. 3

CT Venography of a 39-year old woman with clinical suspicion of cerebral venous thrombosis demonstrates nearly complete bone removal and show a thrombosis of right transverse and sigmoid sinus (arrowheads) and the deep venous system (arrows). In the left distal transverse/proximal sigmoid sinus also an archnoid granulation can be seen. The scan was made at 120 kV and the enhancement in the confluence of sinuses and superior sagittal sinuses was 320 HU and 178 HU, respectively. The ratio SSS-CFS was 0.56. (A) and (B) axial contrast-enhanced images with masked bone at the level of the transverse sinus and deep venous system. (C) and (D) MIPs of the CTV dataset after MMBE in antero-posterior and left-lateral direction.

Table III
Interobserver results of CTV per sinus or vein

	Observer II		
Observer I	Thrombosis	No Thrombosis	Total
Thrombosis	37	3	40
No Thrombosis	18	642	660
Total	55	645	700

Data are dichotomized: visualized, non-visualized and hypoplastic are rated as normal; partially or completely thrombosed are rated as thrombosis. CTV, CT venography

III.D. PER PATIENT ANALYSIS

Interobserver agreement for the presence or absence of thrombosis per patient was excellent ($\kappa = 0.83$; 95% CI: 0.65-1.00), with an agreement in presence or absence of thrombosis in 47 of 50 patients (94%) (Table IV). In 3 of 50 patients (6%) the observers disagreed on final diagnosis (thrombosis in at least one sinus or vein). In 2 patients one observer found a complete thrombosis in the superior sagittal sinus while the other judged the sinus to be non-visualized. In the first patient additional imaging with MRA and DSA (Fig. 4) did not demonstrate a sinus thrombosis, while in the second patient the clinical follow up disqualified suspicion of sinus thrombosis. These 2 patients (60 years and 81 years) both had poor cardiac output and the contrast medium probably had not yet reached the superior sagittal sinus when the scan was started. In both patients the ratio SSS-CFS was very low (0.10 and 0.21 respectively, see also Fig. 2). The first scan of these two patients was rated to be 'poor' by one of the observers because of this technical problem. This observation was not made by the other observer, neither was the quality of the scan of the other patient rated as 'poor' by any observer, as it should have been. We return to this point in the discussion.

The third patient in whom there was a disagreement on the final diagnosis was a 6-year-old boy who had a traumatic head injury after being hit by a car. Because of deteriorating neurological condition, a sinus thrombosis had to be ruled out. One observer found that the superior sagittal sinus and the right transverse sinus were partial thrombosed, while the other judged them to be visualized normally. In the consensus reading when axial images were evaluated in the brain and bone setting, a fracture of the occipital bone with a focal epidural haematoma was seen which displaced and compressed this sinus medially. Both observers agreed that there was no thrombosis.

Table IV
Interobserver results of CTV per patient

	Observer II		
Observer I	Thrombosis	No Thrombosis	Total
Thrombosis	10	0	10
No Thrombosis	3a	37	40
Total	13	37	50

Data are dichotomized: visualized, non-visualized and hypoplastic are rated as normal; partially or completely thrombosed are rated as thrombosis.; CTV, CT venography

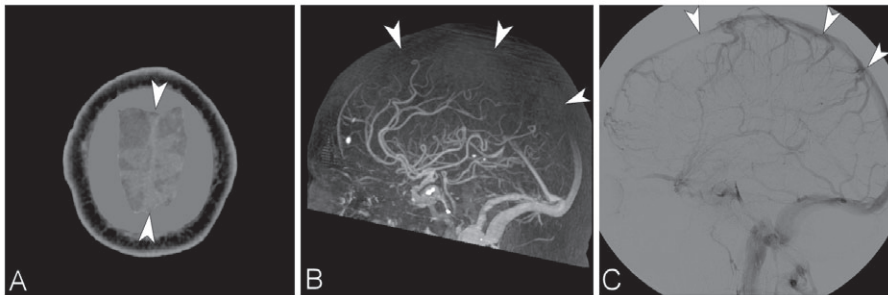a In consensus reading and in follow-up, these 3 patients were found to have no thrombosis

Fig. 4
CT Venography and angiography of a 60-year-old man with clinical suspicion of cerebral venous thrombosis demonstrate a pitfall of CTV (too early scanning due to poor cardiac output). The scan was made at 120 kV and the enhancement in the confluence of sinuses and superior sagittal sinuses was 255 HU and 26 HU, respectively. The ratio SSS-CFS was 0.10. (A) axial contrast-enhanced CT image with masked bone at the level of the vertex. The superior sagittal sinus is not enhanced (arrowheads). (B) right lateral MIP of the CTV dataset after MMBE. The superior sagittal sinus is not visualized (arrowheads) due too early scanning in cranial to caudal direction while the contrast agent has not reached this sinus yet. Small carotid, falcine and tentorial calcifications and auditory ossicles on the right side were not removed but this did not interfere with image interpretation. (C) additional angiography (two days after CTV) does not show thrombosis in the superior sagittal sinus (arrowheads).

IV. DISCUSSION

Our data demonstrate that CTV with MMBE is a robust technique for automatic removal of bone structures from CTV datasets. We found good interobserver agreement for the presence or absence of thrombosis.

The MMBE bone removal technique used in this study was described in detail previously.[15,19] The present study was designed to assess efficacy of bone removal and interobserver variability in CTV examinations in a large patient cohort. In all patients the quality of bone removal was considered to be good, i.e., complete or nearly complete. In some patients the quality of bone removal was only nearly complete because the patient moved during acquisition of the nonenhanced or enhanced CT scan. Because in MMBE each contrast-enhanced image is registered separately with the nonenhanced images,[19] these artifacts were restricted to slice positions at which movement occurred. Some other patients had moved their mandible in between the two scans, which caused the mandible to be not completely removed. In these patients better bone removal can be obtained by using piecewise registration.[25] However, the overall bone removal was still good, and the remaining bone did not interfere with the diagnosis.

In 47 out of 50 patients the observers agreed on the final diagnosis of presence or absence of cerebral venous thrombosis; in the remaining 3 patients they disagreed. In 2 patients this was probably due to impaired cardiac output that resulted in insufficient contrast enhancement. In the other patient it was due too difficulties in discriminating a partial thrombosis from a displacement and compression of a sinus by an epidural haematoma.

Although the overall agreement on a per patient analysis was good, disagreement occurred in 21 of 700 sinuses or veins. This concerned the superior sagittal (n=3), transverse (n=5) and sigmoid sinus (n=3) and veins in the deep venous system (n=10). These discrepancies occurred relatively often for the structures of the deep venous system in patients with a concomitant thrombosed superior sagittal, transverse and/or sigmoid sinus. An explanation for the discrepancy could be mistaking small arteries for veins due to arterial contamination. Arterial contamination is often been seen in patients with cerebral venous thrombosis due to an increase in cerebral circulation time.[26] Discrepancies in interpretation with regard to presence or absence of thrombosis could be resolved in consensus in all involved sinuses and veins. The good interobserver agreement found in the present study is in line with reports from earlier studies that reported on interobserver agreement on CTV; in these studies, however, a considerable lower number of patients was included. Wetzel et al reports an excellent agreement in 10 patients with the use of MIP images.[12] Casey et al reports an excellent agreement in a

number of 14 patients.[11] In the study of Linn et al no kappa was reported; results suggest that in this study the interobserver agreement was also excellent.[9]

In the present study a delay time of 25 seconds was used. Fig. 2 shows that this delay time resulted in a highly variable contrast distribution in the veins with the ratio of enhancement in the superior sagittal sinus and the confluence of sinuses depending on the age of a patient. This suggests that for older patients a better enhancement would have been obtained with a longer delay time, and for younger patient with a shorter one. This is in accordance with findings in literature that optimal timing of a contrast enhanced scan is dependent on age, gender and neurological status of a patient.[27,28] In the patients with thrombosis the ratio SSS-CFS was generally lower than in the other patients, but this could be caused by the presence of a thrombus in the superior sagittal sinus. The fact that the average ratio SSS-CFS is slightly below 1 in our study (see Table I), indicates that on the average the contrast was not yet at its maximum value in the superior sagittal sinus when a scan was started. We recently adjusted our scan protocol to a delay time of 30 seconds, in accordance with the suggestion by Rodallec et al,[7] and found that the ratio SSS-CFS indeed increased to an average slightly exceeding 1. However, in some cases, the ratio of enhancement was almost 2, and in these cases the delay time was probably too long. We note that above observations refer to the scan protocols used in the present study. The choice of an optimal delay time is complicated as scan time, amount of contrast and infusion rate also play a role. Optimal results probably should be obtained with a delay time adjusted to age (see Fig. 2). With the use of CT scanners with more detector rows, scans can be made in a shorter time and a more constant contrast distribution can be obtained, although the choice of the delay time will remain a critical factor for the level of enhancement.

Previous authors have noted that CTV has high sensitivity and specificity (95% and 91%, respectively)[12] for depicting cerebral venous thrombosis when digital subtraction angiography (DSA) is used as the gold standard. In comparison with DSA, CTV normally provides less information on flow dynamics. However, with the development of 320 slice CT scanners 3D dynamic imaging of the whole brain is now also possible.[29] CTV is superior to MR Venography (MRV) in the identification of cerebral veins and dural sinuses and is at least equivalent in establishing the diagnosis of cerebral venous thrombosis.[8,10] Linn et al and Ozsvath

et al report sensitivities and specificities of CTV, with MRV as the gold standard, of both 100%.[9,10] Khandelwal et al reports figures of 75% and 100%, respectively.[8] A major advantage of CTV as compared to MRV is that it can be instantly performed as an adjunct to a nonenhanced CT in the acute setting, resulting in shorter time to diagnosis. Since procedure duration is less than one minute, image quality is hardly impaired by patient motion, and patient monitoring is easier in critically ill patients as compared with MR imaging.[8,10] Compared to MRV (2D TOF MRA), CTV is easier to interpret as it suffers from less pitfalls as compared to MRV.[7,8]

Although the diagnosis of cerebral venous thrombosis can be made by evaluation of the source images or MPR images or thin-slab MIP images of a helical CT scan,[9] 3D MIP images of the complete venous vasculature free from overprojecting bone have clearly additional value. The importance of bone removal in CTV was stressed in a recent surview article by Leach et al.[6] In CT angiography the use of bone removal significantly reduced reading time.[30] 3D MIP images of the complete vasculature are valuable as a communication tool with clinicians, have the ability to be viewed in a limitless number of views and decrease the likelihood that normal anatomic variations, such as high splitting of the superior sagittal sinus, will be mistaken for an empty delta sign.[11]

The use of bone removal is widespread in CTV.[6-8,10-18] In our study, MMBE was chosen for bone removal, because of its user independent and fully automated nature. Manual bone editing in CTV is virtually impossible and semi-automated bone removal techniques are time-consuming and user dependent. The 'graded subtraction' technique,[11] that has been used in a number of CTV studies,[8,10,12,14] requires performance by a highly skilled technologist or radiologist with detailed knowledge of the cerebrovascular anatomy. Even then it may be very difficult to remove all bone without also removing part of the dural sinuses and cortical veins.[6,15]

With MMBE and related techniques[16,21] a nonenhanced CT scan is necessary to remove the bone from the contrast enhanced scan. In the present study an additional low-dose scan was made, with a corresponding slight increase in dose. However, before the CTV scan nearly always a nonenhanced brain CT scan is made to exclude parenchymal abnormalities.[6] Nowadays this scan is made in the spiral mode with thin collimation,[31] and it can be used as the non-enhanced CT scan in the MMBE procedure. In this way the MMBE procedure can be used to

remove bone without exposing the patient to additional radiation dose.

Some lessons can be learnt from the errors that were made by the observers in this study. In some cases errors in the timing of the CTV scan relative to contrast injection lead to the (incorrect) diagnosis of thrombosis, while actually the contrast had not yet arrived or already had disappeared. Judgement of the contrast distribution over the complete venous system, as we have done in this study by determining the SSS-CFS ratio (see Fig. 2), can give information on this point. As noted above, optimal timing is of course of prime importance.

Sometimes it is difficult to distinguish hypoplastic sinuses for (partially) thrombosed sinuses. To reduce the chance to make an error on this respect, observers should pay attention to the presence and size of the vascular groove in the occipital and temporal bone at the expected location of the tranverse and sigmoid sinus. As in the case of hypoplasia or aplasia the groove will be small or even be absent, while it will be well-delineated in the case of thrombosis.[32,33] A final point concerns arterial contamination. We found in the region of the deep venous system arteries were sometimes taken to be small veins. This problem can be reduced by tracing the small vessels back to there parent vessel, to check whether this is arterial or venous.

Disadvantages of CTV include the use of ionizing radiation, limiting its use in pregnant patients and children and the use of iodinated contrast material, limiting its use in patients with renal failure and contrast material allergy.[6]

V. CONCLUSION

Multislice CTV using MMBE is a robust, rapid and fully automatic operator independent technique for visualization of the intracranial venous circulation, removing bone effectively. The technique has a high interobserver agreement for presence or absence of cerebral venous thrombosis.

REFERENCES

1   K. Einhaupl, M. G. Bousser, S. F. de Bruijn, J. M. Ferro, I. Martinelli, F. Masuhr and J. Stam, "EFNS guideline on the treatment of cerebral venous and sinus thrombosis," Eur. J. Neurol. 13 (6), 553-559 (2006).

2   J. Stam, "Thrombosis of the cerebral veins and sinuses," N. Engl. J. Med. 352 (17), 1791-1798 (2005).

3   J. M. Ferro, P. Canhao, J. Stam, M. G. Bousser and F. Barinagarrementeria, "Prognosis of cerebral vein and dural sinus thrombosis: results of the International Study on Cerebral Vein and Dural Sinus Thrombosis (ISCVT)," Stroke 35 (3), 664-670 (2004).

4   M. Wasay and M. Azeemuddin, "Neuroimaging of cerebral venous thrombosis," J. Neuroimaging 15 (2), 118-128 (2005).

5   F. Lafitte, M. Boukobza, J. P. Guichard, C. Hoeffel, D. Reizine, O. Ille, F. Woimant and J. J. Merland, "MRI and MRA for diagnosis and follow-up of cerebral venous thrombosis (CVT)," Clin. Radiol. 52 (9), 672-679 (1997).

6   J. L. Leach, R. B. Fortuna, B. V. Jones and M. F. Gaskill-Shipley, "Imaging of cerebral venous thrombosis: current techniques, spectrum of findings, and diagnostic pitfalls," Radiographics 26 Suppl 1, S19-41; discussion S42-13 (2006).

7   M. H. Rodallec, A. Krainik, A. Feydy, A. Helias, J. M. Colombani, M. C. Julles, V. Marteau and M. Zins, "Cerebral venous thrombosis and multidetector CT angiography: tips and tricks," Radiographics 26 Suppl 1, S5-18; discussion S42-13 (2006).

8   N. Khandelwal, A. Agarwal, R. Kochhar, J. R. Bapuraj, P. Singh, S. Prabhakar and S. Suri, "Comparison of CT venography with MR venography in cerebral sinovenous thrombosis," AJR Am. J. Roentgenol. 187 (6), 1637-1643 (2006).

9   J. Linn, B. Ertl-Wagner, K. C. Seelos, M. Strupp, M. Reiser, H. Bruckmann and R. Bruning, "Diagnostic value of multidetector-row CT angiography in the evaluation of thrombosis of the cerebral venous sinuses," AJNR Am. J. Neuroradiol. 28 (5), 946-952 (2007).

10 R. R. Ozsvath, S. O. Casey, E. S. Lustrin, R. A. Alberico, A. Hassankhani and M. Patel, "Cerebral venography: comparison of CT and MR projection venography," AJR Am. J. Roentgenol. 169 (6), 1699-1707 (1997).

11 S. O. Casey, R. A. Alberico, M. Patel, J. M. Jimenez, R. R. Ozsvath, W. M. Maguire and M. L. Taylor, "Cerebral CT venography," Radiology 198 (1), 163-170 (1996).

12 S. G. Wetzel, E. Kirsch, K. W. Stock, M. Kolbe, A. Kaim and E. W. Radue, "Cerebral veins: comparative study of CT venography with intraarterial digital subtraction angiography," AJNR Am. J. Neuroradiol. 20 (2), 249-255 (1999).

13 M. M. Lell, K. Anders, M. Uder, E. Klotz, H. Ditt, F. Vega-Higuera, T. Boskamp, W. A. Bautz et al., "New techniques in CT angiography," Radiographics 26 Suppl 1, S45-62 (2006).

14 S. O. Casey, D. Rubinstein, K. O. Lillehei, R. A. Alberico, R. R. Ozsvath, A. G. Cajade-Law, B. E. Weprin, E. Michel et al., "Integral and shell-MIP display algorithms in MR and CT three-dimensional models of the brain surface," AJNR Am. J. Neuroradiol. 19 (8), 1513-1521 (1998).

15 C. B. Majoie, M. van Straten, H. W. Venema and G. J. den Heeten, "Multisection CT venography of the dural sinuses and cerebral veins by using matched mask bone elimination," AJNR Am. J. Neuroradiol. 25 (5), 787-791 (2004).

16 M. Lell, K. Anders, E. Klotz, H. Ditt, W. Bautz and B. F. Tomandl, "Clinical evaluation of bone-subtraction CT angiography (BSCTA) in head and neck imaging," Eur. Radiol. 16 (4), 889-897

(2006).

17 H. W. Venema and G. J. den Heeten, "Subtraction helical CT angiography of intra- and extracranial vessels: technical considerations and preliminary experience--rediscovery of matched mask bone elimination?," AJNR Am. J. Neuroradiol. 24 (7), 1491; author reply 1491-1492 (2003).

18 V. K. Jayakrishnan, P. M. White, D. Aitken, P. Crane, A. D. McMahon and E. M. Teasdale, "Subtraction helical CT angiography of intra- and extracranial vessels: technical considerations and preliminary experience," AJNR Am. J. Neuroradiol. 24 (3), 451-455 (2003).

19 H. W. Venema, F. J. Hulsmans and G. J. den Heeten, "CT angiography of the circle of Willis and intracranial internal carotid arteries: maximum intensity projection with matched mask bone elimination-feasibility study," Radiology 218 (3), 893-898 (2001).

20 M. Romijn, H. A. Gratama van Andel, M. A. van Walderveen, M. E. Sprengers, J. C. van Rijn, W. J. van Rooij, H. W. Venema, C. A. Grimbergen et al., "Diagnostic Accuracy of CT Angiography with Matched Mask Bone Elimination for Detection of Intracranial Aneurysms: Comparison with Digital Subtraction Angiography and 3D Rotational Angiography," AJNR Am. J. Neuroradiol. (2007).

21 H.A.F. Gratama van Andel, H. W. Venema, G. J. Streekstra, M. van Straten, C. B. Majoie, C. A. Grimbergen and G. J. den Heeten, "Removal of bone in CT angiography by multiscale matched mask bone elimination," Med. Phys. 34 (10), 3711-3723 (2007).

22 S. D. Olabarriaga, J. G. Snel, C. P. Botha and R. G. Belleman, "Integrated support for medical image analysis methods: from development to clinical application," IEEE Trans. Inf. Technol. Biomed. 11 (1), 47-57 (2007).

23 D.G. Altman, (Chapman & Hall, London, 1999), pp. 403-405.

24 A. Waaijer, M. Prokop, B. K. Velthuis, C. J. Bakker, G. A. de Kort and M. S. van Leeuwen, "Circle of Willis at CT angiography: dose reduction and image quality--reducing tube voltage and increasing tube current settings," Radiology 242 (3), 832-839 (2007).

25 M. van Straten, H. W. Venema, G. J. Streekstra, C. B. Majoie, G. J. den Heeten and C. A. Grimbergen, "Removal of bone in CT angiography of the cervical arteries by piecewise matched mask bone elimination," Med. Phys. 31 (10), 2924-2933 (2004).

26 R. Kochhar, N. Khandelwal, P. Singh and S. Suri, "Arterial contamination: a useful indirect sign of cerebral sino-venous thrombosis," Acta Neurol. Scand. 114 (2), 139-142 (2006).

27 S. Lukosevicius, A. Basevicius and A. Tamasauskas, "Cerebral computed tomographic angiography scan delay in subarachnoid hemorrhage," Neurol. India 53 (1), 73-77; discussion 77-78 (2005).

28 I. J. Hartmann, R. T. Lo, J. Bakker, W. de Monye, P. F. van Waes and P. M. Pattynama, "Optimal scan delay in spiral CT for the diagnosis of acute pulmonary embolism," J. Comput. Assist. Tomogr. 26 (1), 21-25 (2002).

29 E. Siebert, G. Bohner, M. Dewey, F. Masuhr, K. T. Hoffmann, J. Mews, F. Engelken, H. C. Bauknecht et al., "320-slice CT neuroimaging: initial clinical experience and image quality evaluation," Br. J. Radiol. (2009).

30 D. Morhard, C. Fink, C. Becker, M. F. Reiser and K. Nikolaou, "Value of automatic bone subtraction in cranial CT angiography: comparison of bone-subtracted vs. standard CT angiography in 100 patients," Eur. Radiol. 18 (5), 974-982 (2008).

31 M. van Straten, H. W. Venema, C. B. Majoie, N. J. Freling, C. A. Grimbergen and G. J. den Heeten, "Image quality of multisection CT of the brain: thickly collimated sequential scanning versus thinly collimated spiral scanning with image combining," AJNR Am. J. Neuroradiol. 28 (3), 421-427 (2007).

32 J. L. Mas, J. F. Meder, E. Meary and M. G. Bousser, "Magnetic resonance imaging in lateral sinus hypoplasia and thrombosis," Stroke 21 (9), 1350-1356 (1990).

33 Bernhard Schaller, "State-of-the-Art Imaging in Stroke". (Nova Biomedical Books, 2007).

5

Evaluation of an improved technique for automated center lumen line definition in cardiovascular image data

Hugo A.F. Gratama van Andel, Erik Meijering, Aad van der Lugt, Henri A. Vrooman,
Cecile de Monyé, Rik Stokking

ABSTRACT

The aim of the study was to evaluate a new method for automated definition of a center lumen line in vessels in cardiovascular image data. This method, called VAMPIRE, is based on improved detection of vessel-like structures. A multiobserver evaluation study was conducted involving 40 tracings in clinical CTA data of carotid arteries to compare VAMPIRE with an established technique. This comparison showed that VAMPIRE yields considerably more successful tracings and improved handling of stenosis, calcifications, multiple vessels, and nearby bone structures. We conclude that VAMPIRE is highly suitable for automated definition of center lumen lines in vessels in cardiovascular image data.

I. INTRODUCTION

Analysis of vasculature in patients suspected of atherosclerosis is of great importance as cardiovascular disease is one of the leading causes of death in the western world. Accurate and reproducible methods to analyze vessels, and most importantly the degree of stenosis, are crucial when considering therapeutical options. Traditionally Digital Subtraction Angiography (DSA) projection images have been the gold standard for stenosis grading. The shortcomings of visual assessment of these types of images have motivated the development of automated techniques to support vessel analysis,[3,4] which resulted in programs such as Quantitative Coronary Angiography (QCA).[5] Nowadays the required image data for diagnostic purposes on vessels is increasingly acquired using techniques such as Magnetic Resonance Angiography (MRA) and Computed Tomography Angiography (CTA),[6] which are minimally invasive and yield three-dimensional (3D) image data. Part of the analysis of this image data is usually automated but nonetheless the observer is required to make (a considerable amount of) decisions which means that the whole procedure is still time consuming and highly user dependent.[4] In the future these problems are expected to rise considerably given the continuing increase in the application of these non-invasive imaging techniques.[7]

It is therefore crucial to develop automated methods for accurate, fast, robust and reproducible analysis of (atherosclerotic) vessels in CTA and MRA data.

Automated analysis of vessels can be roughly divided into several steps: segmentation, quantification, and visualization. Segmentation is the basis for the other steps and typically involves definition of a center lumen line (CLL). This CLL can be defined manually (possibly supported by some form of automation) but the resulting CLLs have a high intra and inter observer variability.[8-10] Automated definition of a CLL is called for and several methods have been published.[1,11,12]

Aylward et al.[13] grouped the path tracing methods into 3 approaches: explicit methods (directly targeting a CLL), implicit methods (whenever a CLL extraction is implied in methods to segment a tubular object), and post-processing methods (the lumen is segmented from which a CLL is calculated). Implicit and post-processing methods can be suitable techniques whenever a vessel tree needs to be extracted, e.g. for surgical planning and/ or guidance, or for centerline extraction for virtual colonoscopy.[14] Unfortunately these methods appear less suitable for quantification of vessels.[1,15] This is because automated segmentation of the lumen typically runs into problems in stenotic areas,[16] especially in vessels with a small diameter such as coronary arteries. Here we focus on techniques for explicit path tracing as results from earlier studies and our own preliminary tests indicated that (some of) these techniques have the potential to cope with stenotic areas and may therefore be more suitable for the automated tracing of a CLL.

Over recent years a number of techniques for explicit automated path tracing in vessels have been published. The first approach is the use of iterative methods, i.e. a path grows in a search direction based on local properties.[16] For example, Direct Vessel Tracking[17] determines the middle of a vessel by performing a local search algorithm based on previously defined points and edge-detection of the vessel. Unfortunately, vessels of high curvature and vessels where the lumen area does not change gradually, such as in the transition to a stenosis or an aneurysm, cause considerable problems. In general, iterative methods fail in cases with severe stenosis or image degradation.[16] A second approach centers on the use of filters specifically aimed at vessel-like structures.[1,13,15-19] The results are very promising, but actual application in clinical procedures is hampered by the high computational cost.

The aforementioned techniques for explicit automated path tracing typically

run into problems when dealing with vessels with abnormalities such as stenoses, aneurysms, and calcifications, but also when dealing with bifurcations, vessels of high curvature and nearby other vessels and bone. These problems severely hamper application in clinical practice and only very few quantitative evaluation results have been reported so far.[1] With this in mind we decided to implement and quantitatively evaluate a new method for automated definition of a CLL in cardiovascular image data based on improved detection of vessel-like structures. These technical improvements were first tested on 2D images of clinical data as a proof of concept. This paper briefly describes our method and presents the results of a multi-observer evaluation study performed on (clinical) cardiovascular image data.

II. MATERIALS AND METHODS

II.A. DESCRIPTION OF METHOD

Our method for automated CLL definition in cardiovascular image data is called 'VAMPIRE' (Vascular Analysis using Multiscale Paths Inferred from Ridges and Edges). The major progress in VAMPIRE comes from the combination of an improved ridge filter with standard Canny edge detection to enhance elongated structures.[20] The ridge filter is based on a modified Hessian (second-order derivative matrix) and it has already been successfully applied for automated neurite tracing.[21] We hypothesized that the modified Hessian, and corresponding ridge filter, should also be more sensitive to elongated structures such as vessels compared to vessel tracing techniques based on normal Hessian analysis [1,2] (Fig. 1). In addition, Hessian analysis provides vector information (Fig. 2), which is highly suited to steer search algorithms in tracing a path. The actual implementation in VAMPIRE utilizes a multiscale version of the ridge filter, which makes it more suitable for the varying diameters of vessels in cardiovascular image data.[1,15] The resulting edge and ridge information is used to calculate a cost image (Fig. 3). Subsequently, an implementation of Dijkstra's shortest path algorithm based on the cost image and the vector information yields a minimal cost path.[19,22]
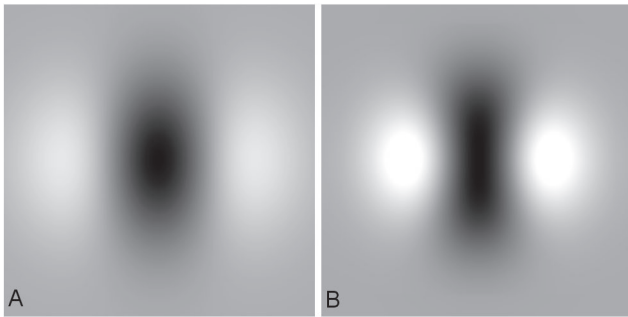
Fig. 1
Visualization of the shapes of (a) the ridge filter based on normal Hessian analysis as described by Frangi et al.1,2, and (b) the ridge filter based on the modified Hessian as used in VAMPIRE. The use of the modified Hessian makes the corresponding filter more sensitive for vessel-like structures.
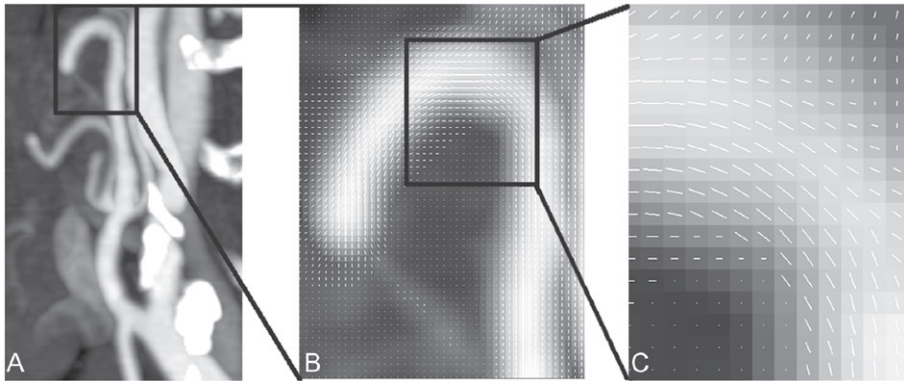

Fig. 2
The analysis of (a) the original image using the modified Hessian implemented in VAMPIRE yields vector information as shown as white lines for each pixel in the blow-ups of (b) and (c).
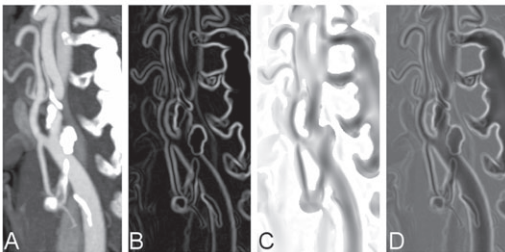

Fig. 3
(d) A cost image is calculated from (a) the original image based on (b) Canny edge filtering and (c) ridge filtering using the modified Hessian.

VAMPIRE is compared with a method based on a ridge filter for vessel enhancement using normal Hessian analysis,[18] in combination with a minimal cost path algorithm (identical algorithm is used in VAMPIRE) as described by Wink et al.[19] In short we will call this combination the Frangi-Wink method. Both the Frangi-Wink method and VAMPIRE were implemented as plug-ins in a public domain JavaTM[23] image-processing program called ImageJ.[24] The parameter settings were optimized for both methods and were fixed during the experiments. This strategy follows from earlier work by Sato et al.[15] and our parameters were based on the same settings.

II.B. EVALUATION OF THE METHOD

In this evaluation study we used 21 slab maximum intensity projections (MIPs)[25] with a thickness of 10 mms of multislice CTA image data from 14 patients with stenosis (>30%) in the internal carotid artery (ICA). The slab MIPs were oriented in such a way that the common carotid artery (CCA), the ICA, and the external carotid artery (ECA) were visualized in one image. In these 21 slab MIPs a total of 40 tracings were obtained by focusing on the CCA plus bifurcation and either choosing the ICA (yielding 24 paths, as sometimes both ICAs were visible) or the ECA (yielding 16 paths) as secondary target.

Reference paths for each of the 40 tracings were obtained by manual path tracing performed by four qualified and trained observers. The datasets were blinded and given in different order to the observers. Each observer indicated points in the target vessel in each of the MIPs which were automatically connected by straight lines resulting in 160 CLLs (40 CLLs per observer). The path tracings were required to begin as proximal as possible in the CCA and track either the ICA or ECA as distal as possible. All paths, required time and required number of points were stored individually for each of the observers. Subsequently, a mean manual tracing was calculated from the paths of the four observers for each of the 40 vessels.

The automated tracings of Frangi-Wink and VAMPIRE were both initialized using the same start and end point. Whenever the defined path left the target vessel a live-wire[26] implementation allowed placement of an additional point (performed by the main author, setting the total to three) to prevent the path from leaving the vessel. The minimal cost path algorithm in combination with the live-wire

implementation allows minimal observer-variability in the placement of the additional point within the target vessel, which implies that the resulting path is virtually observer-independent.

Evaluation of the tracings was based on calculating the deviation. This deviation was defined as the area spanned between a tracing and corresponding reference tracing divided by the length of the reference tracing (area/ length).[21] Consequently, the deviation for the manual tracings was determined by calculating the deviation for each observer using the mean tracing of the other three observers as reference. The deviation for an automated tracing (either the Frangi-Wink method or VAMPIRE) was assessed using the corresponding mean manual tracing as reference.

II.C. STATISTICAL ANALYSIS

The observer experiments were analyzed using a mixed model ANOVA. First we considered observer as fixed effect in order to test for systematic differences between observers; next we considered observer as random effect along with the vessels in order to estimate the between-vessel variance component and the two within- vessel components (between- and within-observer).

The paired Student t-test was found to be the most appropriate method for statistical analysis of the results of the automated methods. To obtain a normal (gaussian) distribution in the data the values were log-transformed. Significance is supposed to be reached for p-values below 0.05.

III. RESULTS

III.A. MANUAL TRACINGS

Table I shows results of the manual tracings for each observer using the average tracing of the other three observers as reference. Considering observer as fixed effect, the null hypothesis of equal manual tracing could be rejected (p = 0.028).

Pairwise comparison of the observers only revealed a significant difference between observers 1 and 3 (p = 0.003; 95 % CI: 0.061 – 0.295). When considering random effects, the total variance of the manual tracings equals 0.100 mm, of which 27 % is due to between-image variability. The remaining 73 % of within-image variability is the total of 4 % between-observer and 69 % within-observer variability. However, the between-image variability component of 27 % is an artifact caused by taking absolute deviations (spanned areas) of within-image measurements. This is because the definition of the tracing value of an observer is the absolute deviation from an average of absolute deviations from a reference tracing in the other three observers.

In-depth analysis of the manual tracings showed two situations, i.e., i) the observers produced virtually identical tracings in areas where the vessel could be considered normal, and ii) the observers produced considerable differences in abnormal areas, most notably in stenotic areas with calcifications (Fig. 5a).

Table I
Path tracing results for the four observers

	Mean deviation*
Observer 1	1.08 ± 0.33
Observer 2	1.02 ± 0.29
Observer 3	0.90 ± 0.29
Observer 4	0.99 ± 0.33
mean	1.00 ± 0.31

* In mm with sd over all 40 path tracings for each of the four observers using the average of the other three observers as reference.

III.B. USER INTERACTION

On average, the observers required 18.1 ± 4.7 points (including start and end point) and 41.9 ± 14.0 seconds for each of the manual vessel tracings. For the automated path definition the time needed to calculate the cost-image (essentially preprocessing) was 12 seconds on a Pentium IV 2 GHz. The subsequent definition of a minimal cost path (based on previously defined start and end points) was virtually instantaneous. Essentially the latter step was only limited by the required

user-interaction whenever the tracing left the target vessel. The time it took an observer to indicate all required points (i.e. start and end point and, when necessary, an additional point) in order to define a path using the automated methods was approximately 3 seconds per case. In short, the automated technique VAMPIRE considerably reduced the number of required clicks (from 18 to a maximum of 3) and required time (from 42 sec. to 3 sec.) per vessel in tracing atherosclerotic carotid arteries compared to manual vessel tracing.

III.C. COMPARISON AUTOMATED METHODS

The results of the path tracing based on a start and end initialization point using the automated methods Frangi-Wink and VAMPIRE were compared with the mean tracings of the four observers (see Table II). Statistical analysis revealed that the results for the automated methods Frangi-Wink and VAMPIRE were significantly different ($p = 0.000$, ci -1.710 - -0.910). Moreover, both methods yielded significantly different results when compared to the manual mean (Frangi-Wink: $p = 0.000$, ci $= 1.646 – 2.503$ and VAMPIRE: $p = 0.000$, ci 0.562 - 0.967), which is primarily caused by the automated tracings that left the target vessel. With the Frangi-Wink method 29 path tracings left the target vessel and with VAMPIRE this was limited to 7 cases.

Table II
Results for the automated methods Frangi-Wink and VAMPIRE compared with the manual reference

	Manual mean	Frangi-Wink[†]	VAMPIRE[†]
mean deviation*	1.00 ± 0.31	16.33 ± 19.91	2.66 ± 2.32

* In mm. with sd. over all 40 path tracings.
[†]Both Frangi-Wink and VAMPIRE were initialized using the same start and end point.

These results show that, given the two initialization points, VAMPIRE clearly outperforms the Frangi-Wink method, but still requires improvements and/or more user interaction to produce acceptable tracings.

III.D. AUTOMATED METHODS: ADDITIONAL USER-INTERACTION

The benefit of additional user-interaction was assessed by adding one additional point whenever an automated tracing left the target vessel. Consequently, the results of the Frangi-Wink method and VAMPIRE were subdivided into three categories (Table III); (i) '2-point-success': tracings initialized by one start and one end point that did not leave the target vessel; (ii) '3-point-success': tracings requiring one additional point to stay in the target vessel; and (iii) 'unsuccessful': tracings leaving the target vessel even after an additional point is placed.

Without an aditional point, there were 7 cases were VAMPIRE left the target vessel. This was caused by a nearby other vessel or overprojection of another vessel in the MIP (5 cases), or a nearby elongated calcification (1 case), or a combination of both (1 case). The results for these 7 cases with the Frangi-Wink method were worse compared to VAMPIRE, i.e. with the Frangi-Wink method 2 of these cases required an additional point and the remaining 5 cases were unsuccessful.

Given the additional point there where no cases where VAMPIRE tracings left the target vessel whereas the Frangi-Wink method still resulted in 20 tracings leaving the target vessel. Some of the tracings with the Frangi-Wink method needed up to 8 additional points to keep the tracing in the vessel.

Table III
Results for the automated methods Frangi-Wink and VAMPIRE after additional user-interaction.

	Frangi-Wink		VAMPIRE	
Category	mean deviation*	n†	mean deviation*	n†
2-point-success	1.58 ± 0.64	11	1.71 ± 0.51	33
3-point-success	1.65 ± 0.91	9	1.67 ± 0.60	7
Unsuccessful	7.06 ± 4.28	20	-	-

* In mm. with sd.
† n = number of cases.

The results for both automated methods for the categories 2-point-success and 3-point-success were statistically analyzed and compared to the manual mean. This test revealed that there was no significant difference between the automated methods Frangi-Wink and VAMPIRE with regards to the tracings in the categories

2-point-success and 3-point-success (2-point-success: $p = 0.329$, $ci = -0.127 -$ 0.343 and 3-point-success; $p = 0.908$, $ci = -1.961 - 1.917$). The mean values for both automated methods for the categories 2-point-success and 3-point-success were still significantly different from the manual mean (Frangi-Wink, 2-point-success: $p = 0.017$, $ci = 0.079 - 0.635$, VAMPIRE, 2-point-success: $p = 0.000$, $ci = 0.413 - 0.628$, Frangi-Wink, 3-point-success: $p = 0.009$, $ci = 0.140 - 0.720$ and VAMPIRE, 3-point-success: $p = 0.000$, $ci = 0.307 - 0.651$).

Several typical examples from the category 'unsuccessful' are depicted in Fig. 4. The paths defined using the Frangi-Wink method left the target vessel because of bone, calcifications, or another vessel, whereas the paths defined using VAMPIRE did not leave the target vessel. Characteristic examples of problems in defining a CLL in the current implementation of VAMPIRE are presented in Fig. 5b en Fig. 5c. Fig. 5b illustrates the problem of nearby or overlapping vessels in the MIP images and Fig. 5c illustrates swaying of the VAMPIRE path caused by calcifications and local variations of the edge of the lumen.
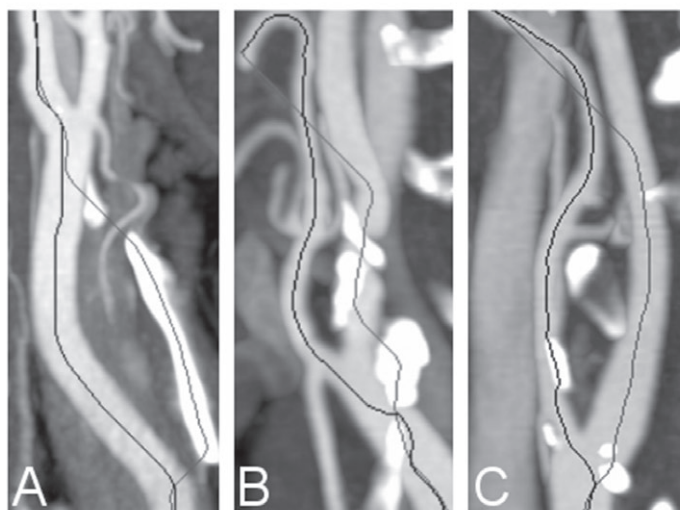

Fig. 4
Three examples where the Frangi-Wink method (gray tracings) yielded errors in path definition because of (a) bone, (b) calcifications, or (c) another vessel. Use of VAMPIRE resulted in paths (black tracings) that did not leave the target vessels.
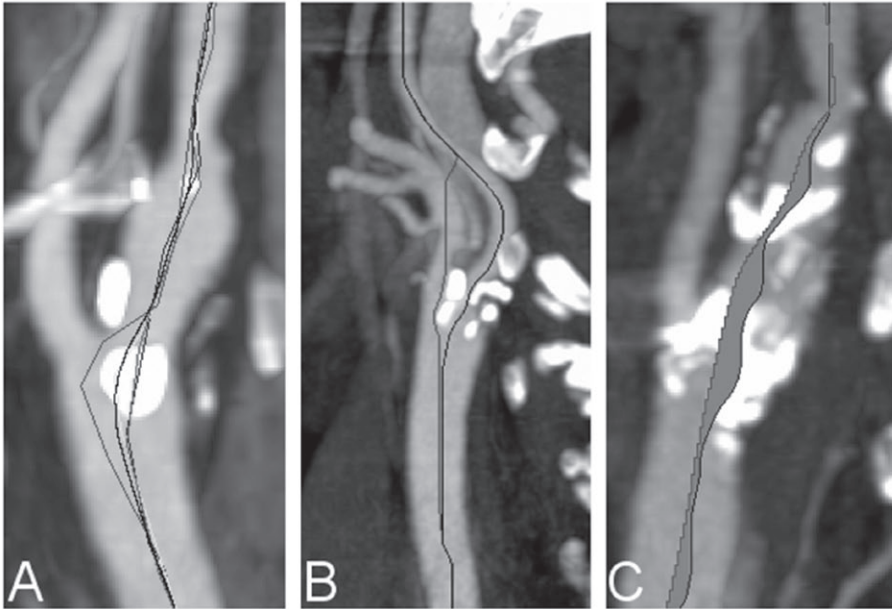
Fig. 5
Problems in defining a CLL: (a) observer tracings indicating differences in manual CLL definition especially in dealing with calcifications and bifurcations, (b) the proximity of another vessel causes the VAMPIRE tracing to leave the target vessel, and (c) paths defined using VAMPIRE occasionally exhibit swaying behavior.

IV. DISCUSSION

This study evaluates the combined effect of two technical improvements over earlier methods for explicit automated path tracing in clinical data, i.e., a filter more tuned to vessel-like structures and the combination with edge information. These technical improvements in VAMPIRE were first tested on 2D images of clinical data as a proof of concept. This setup not only saved considerable time and effort in implementing and testing the method, but also in the required manual labor for the path tracings by the clinicians. In addition, the 2D images made it very easy to visually assess the behavior of the automated (and observer) tracings.

VAMPIRE was compared with the method as described by Frangi and Wink and we found that the automated path definitions obtained with VAMPIRE were considerably more successful in tracing the target vessel with fewer problems in finding a CLL nearby stenoses, calcifications, multiple vessels and bone structures.

Given the design of the present study we cannot distill from the results whether and in what way this success can be attributed to the use of the modified Hessian or by the addition of edge information. This will be subject to further study. Moreover, Wink et al.[16] recently published an improved version of the Frangi-Wink method. Their improvement is complementary to our improvements and will most propably be included in future versions of VAMPIRE.

The respons of the ridge filters for both the Frangi-Wink and VAMPIRE methods is dependent on the intensity, i.e. high intensities favor higher ridge responses. Originally the Frangi-Wink method was used for MRA image data where this intensity dependence can be regarded an advantage for vessel tracing. However, when applying these ridge filters on CTA data the intensity dependence implies that the traced path will be attracted to high HU values of calcifications and bone. This unwanted behavior was clearly noticeable with the Frangi-Wink method. The addition of the edge information in VAMPIRE seems to be a powerful mechanism to prevent the traced path to follow calcified structures. Another option to prevent the unwanted behavior could be to segment the calcified structures from the CTA data as a preprocessing step. Unfortunately, the HU distributions of the contrast in the vessel and the calcified structures typically overlap, which means that segmentation, e.g. by setting a single threshold, is not straightforward and may require (substantial) user input. More intricate segmentation methods for calcified structures in CTA such as proposed by van Straten et al. and Isgum et al.[27-29] may be more appropriate. However, VAMPIRE tracings experienced little problems with the calcified structures and we therefore decided not to further pursue this.

Path definitions using VAMPIRE resulted in a slightly higher mean deviation in the 2-point-success tracings (1.71 mm) compared to Frangi-Wink (1.58 mm). Although this difference is not statistically significant we decided to analyze it more thoroughly. This difference appears to be caused by the swaying behavior (Fig. 5c) in the path definitions by VAMPIRE, which is probably due to two main factors. First factor is the sensitivity of the Canny edge filter to edges in the lumen caused by inhomogeneous contrast filling. This clearly caused the tracings to exhibit unwanted behavior when using VAMPIRE and a simple thresholding step of the edge information was implemented so as to suppress filter responses to small edges in the lumen. We anticipate that this threshold will no longer be necessary upon further optimizing the parameters for the calculation of the cost

image from the edge and ridge information. Second factor is the effect of small structures like calcifications and nearby bone structures, but also small variations in the edges of the vessel itself. The observers typically ignored these small effects, but it was not clear whether this was motivated by the aim to produce smooth paths or merely to save time and effort by taking shortcuts. This means that the question whether these small effects cause the VAMPIRE tracings to exhibit truly unwanted behavior can only be answered after standards have been developed for the definition of the CLL in clinical data.

Unique (mathematical) definition of a CLL in simulated and phantom data of vessels is possible, but unfortunately defining the CLL of a vessel in clinical cases is not trivial. The variation in the tracings performed by the observers made this very clear, especially in areas involving e.g. a bifurcation, stenosis, or calcification (see the tracings by each of the four observers in Fig. 5a). As a further complication different clinical questions may require different definitions of an 'optimal' path (not necessarily the CLL). For instance, the path for quantification of stenoses probably follows the center of the lumen whereas a path defined for stent placement may be required to follow the center of the vessel. As already implied earlier, standards have to be developed for the definition of the CLL in clinical cases.

The use of the minimal cost path algorithm to calculate the path implies that methods such as Frangi-Wink and VAMPIRE will tend to follow the inner curve of a vessel and not the center of the vessel. Whenever this behavior is unwanted it can be reduced or even prevented by using another algorithm to calculate a path in the cost image or by adding an extra processing step, e.g. using the local edge and/ or ridge information to optimize the location of all individual points of the tracing.

As already indicated earlier, Hessian analysis on multiple scales in 3D data is a problem because of the high computational cost. A local instead of global analysis of the Hessian can avoid this problem, e.g. by using thresholding-based pre-segmentation of the vessels.[13] Other options are to perform the required calculations in a pre-processing step and/ or to use a parallel implementation on a multi-CPU machine using multi-threaded programming.[15]

An important consequence of the obtained results is the fact that paths defined using VAMPIRE in the images we used are virtually independent of the observer. In 33 of 40 cases the required observer input in the MIP images of the carotid arteries was limited to the two initialization points. In the remaining 7 cases

one additional point was required. Additional software can be developed which takes these points as a first guess and investigates the neighboring edge and ridge information to locate optimal points ('snapping'). This would effectively remove all observer-critical decisions in the definition of paths. The remaining observer input can even be replaced by using an atlas or (CLL) model (e.g. based on statistical analysis) in combination with nonlinear registration so as to provide the relevant initialization data. This would result in completely user-independent vessel tracing and the observer would only be required to verify the results of the path tracing.

The applicability of VAMPIRE was tested on image data from DSA, MRA and CTA in other clinical cardiovascular studies. Fig. 6 presents the results of VAMPIRE for a DSA image and MRA data, and in Fig. 7 a result for coronary CTA data is shown. No additional points other than a start and end point were required to yield these successful tracings. These promising results indicate the potential of VAMPIRE in other imaging modalities and/ or other clinical cardiovascular applications.
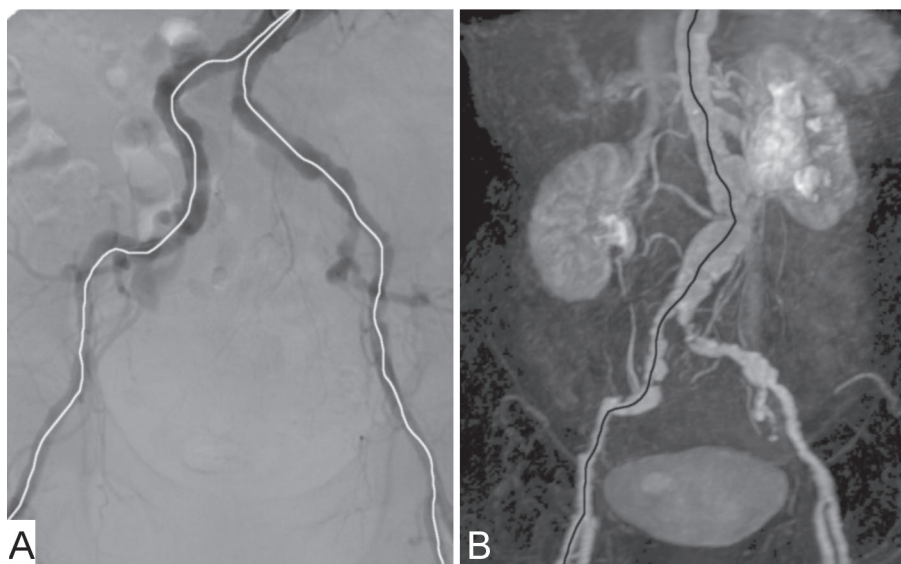

Fig. 6
Examples of path definitions in aorta-iliac arteries using VAMPIRE in (a) a DSA image and (b) a MIP of an MRA dataset.
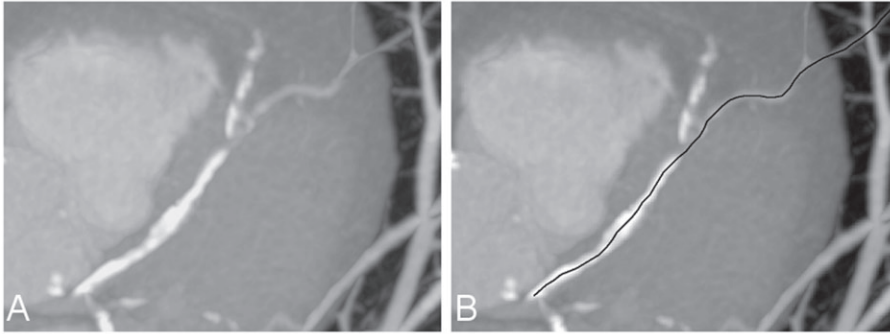
Fig. 7
(a) A MIP-image of a CTA of coronary arteries (b) with a path definition using VAMPIRE.

The result of our evaluation study indicate that automated vessel tracing in CTA images of the carotid artery with VAMPIRE is a robust technique which considerably reduces the amount of observer interaction and time compared to manual tracing. We conclude that the VAMPIRE approach is highly suitable for automated path definition in vessels in (clinical) cardiovascular image data. Further development of the technique is expected to yield fully automatic, observer independent paths (also in 3D) that may directly serve as CLLs in accordance with standards provided by clinicians.

V. ACKNOWLEDGMENTS

REFERENCES

1   A. F. Frangi, W. J. Niessen, R. M. Hoogeveen, T. van Walsum and M. A. Viergever, "Model-based quantitation of 3-D magnetic resonance angiographic images," IEEE Trans. Med. Imaging 18 (10), 946-956 (1999).

2   A. F. Frangi, W. J. Niessen, K.L. Vincken and M. A. Viergever, presented at the Medical Image Computing and Computer-Assisted Intervention, Boston, USA, 1998 (unpublished).

3   K. Haris, S. N. Efstratiadis, N. Maglaveras, C. Pappas, J. Gourassas and G. Louridas, "Model-based morphological segmentation and labeling of coronary angiograms," IEEE Trans. Med. Imaging 18 (10), 1003-1015 (1999).

4   H. Greenspan, M. Laifenfeld, S. Einav and O. Barnea, "Evaluation of center-line extraction algorithms in quantitative coronary angiography," IEEE Trans. Med. Imaging 20 (9), 928-952 (2001).

5   J.H.C. Reiber, L.R. Schiemanck, P.M.J. van der Zwet, G. Koning, B. Goedhart, J.J. Gerbrands, M.J. Schalij and A.V.G. Bruschke, in Quantitative Coronary Imaging, edited by P.J. de Feyter, C. Di Mario, and P.W. Serruys (1995), pp. 9-27.

6   P. J. Nederkoorn, W. P. Mali, B. C. Eikelboom, O. E. Elgersma, E. Buskens, M. G. Hunink, L. J. Kappelle, P. C. Buijs et al., "Preoperative diagnosis of carotid artery stenosis: accuracy of noninvasive testing," Stroke 33 (8), 2003-2008 (2002).

7   G. D. Rubin, "Data explosion: the challenge of multidetector-row CT," Eur. J. Radiol. 36 (2), 74-80 (2000).

8   C. W. White, C. B. Wright, D. B. Doty, L. F. Hiratza, C. L. Eastham, D. G. Harrison and M. L. Marcus, "Does visual interpretation of the coronary arteriogram predict the physiologic importance of a coronary stenosis?," N. Engl. J. Med. 310 (13), 819-824 (1984).

9   L.M. Zir, S.W. Miller, R.E. Dinsmore, J.P. Gilbert and J.W. Harthorne, "Interobserver variability in coronary angiography," Circulation 53 (4), 627-676 (1976).

10 T. Sandor, A. d'Adamo, W.B. Hanlon and J.R. Spears, "High precision quantitative angiography," IEEE Trans. Med. Imaging 6 (Sept.), 258-266 (1987).

11 F. K. Quek and C. Kirbas, "Vessel extraction in medical images by wave-propagation and traceback," IEEE Trans. Med. Imaging 20 (2), 117-131 (2001).

12 L. M. Lorigo, O. D. Faugeras, W. E. Grimson, R. Keriven, R. Kikinis, A. Nabavi and C. F. Westin, "CURVES: curve evolution for vessel segmentation," Med. Image Anal. 5 (3), 195-206 (2001).

13 S. R. Aylward and E. Bullitt, "Initialization, noise, singularities, and scale in height ridge traversal for tubular object centerline extraction," IEEE Trans. Med. Imaging 21 (2), 61-75 (2002).

14 M. Wan, Z. Liang, Q. Ke, L. Hong, I. Bitter and A. Kaufman, "Automatic Centerline Extraction for Virtual Colonoscopy," IEEE Trans. Med. Imaging 21 (12), 1450-1460 (2002).

15 Y. Sato, S. Nakajima, N. Shiraga, H. Atsumi, S. Yoshida, T. Koller, G. Gerig and R. Kikinis, "Three-dimensional multi-scale line filter for segmentation and visualization of curvilinear structures in medical images," Med. Image Anal. 2 (2), 143-168 (1998).

16 O. Wink, W. J. Niessen and M. A. Viergever, "Multiscale vessel tracking," IEEE Trans. Med. Imaging 23 (1), 130-133 (2004).

17 O. Wink, W. J. Niessen and M. A. Viergever, "Fast delineation and visualization of vessels in 3-D angiographic images," IEEE Trans. Med. Imaging 19 (4), 337-346 (2000).

18 C.M. Van Bemmel, L. Spreeuwers, M. A. Viergever and W.J. Niessen, presented at the 10th Annual Meeting of the International Society for Magnetic Resonance in Medicine (ISMRM), Honolulu,

Hawaii, 2002 (unpublished).

19 O. Wink, A. F. Frangi, B. Verdonck, M. A. Viergever and W. J. Niessen, "3D MRA coronary axis determination using a minimum cost path approach," Magn. Reson. Imaging 47 (6), 1169-1175 (2002).

20 M. Jacob and M. Unser, "Design of Steerable Filters for Feature Detection using Canny-Like Criteria," IEEE Trans. Pattern Anal. Mach. Intell. 26 (8), 1007 - 1019 (2004).

21 E. Meijering, M. Jacob, J. C. Sarria, P. Steiner, H. Hirling and M. Unser, "Design and validation of a tool for neurite tracing and analysis in fluorescence microscopy images," Cytometry 58A (2), 167-176 (2004).

22 T.H. Cormen, C.E. Leiserson, R.L. Rivest and C. Stein, "Introduction to Algorithms", 2 ed. (MIT Press, Cambridge, MA, 2001).

23 Inc. Sun Microsystems.

24 W. Rasband, (U.S. National Institutes of Health).

25 G. D. Rubin, "Techniques for performing multidetector-row computed tomographic angiography," Techniques in Vascular and Interventional Radiology 4 (1), 2-14 (2001).

26 A. X. Falcao, J. K. Udupa and F. K. Miyazawa, "An ultra-fast user-steered image segmentation paradigm: live wire on the fly," IEEE Trans. Med. Imaging 19 (1), 55-62 (2000).

27 M. van Straten, H. W. Venema, G. J. Streekstra, C. B. Majoie, G. J. den Heeten and C. A. Grimbergen, "Removal of bone in CT angiography of the cervical arteries by piecewise matched mask bone elimination," Med. Phys. 31 (10), 2924-2933 (2004).

28 M. van Straten, H. W. Venema, G. J. Streekstra, J. A. Reekers, G. J. den Heeten and C. A. Grimbergen, "Removal of arterial wall calcifications in CT angiography by local subtraction," Med. Phys. 30 (5), 761-770 (2003).

29 I. Isgum, B. van Ginneken and M. Olree, "Automatic detection of calcifications in the aorta from CT scans of the abdomen. 3D computer-aided diagnosis," Acad. Radiol. 11 (3), 247-257 (2004).

6

Model-based measurements of the diameter of the internal carotid artery in CT angiography images

Hugo A.F. Gratama van Andel, Henk W. Venema, Karin Bol, Henk A. Marquering,
Charles B.L.M. Majoie, Gerard J. den Heeten, Cornelis A. Grimbergen and Geert J. Streekstra

ABSTRACT

Computed tomography angiography (CTA) is often used to determine the degree of stenosis in patients that suffer from carotid artery occlusive disease. Accurate and precise measurements of the diameter of the stenosed internal carotid artery are required to make decisions on treatment of the patient. However, the inherent blurring of images hampers a straightforward measurement, especially for smaller vessels.

We propose a model-based approach to perform diameter measurements in which explicit allowance is made for the blurring of structures in the images. Three features of our approach are the use of prior knowledge in the fitting of the model at the site of the stenosis, the applicability to both cylindrical and non-cylindrical vessels and the ability to deal with additional structures in the images such as calcifications. Cross-sections of non-cylindrical vessels were modeled with Fourier descriptors. When calcifications are adjacent to the lumen, both the lumen and the calcifications were modeled in order to improve the diameter estimates of the vessel.

Measurements were performed in CT scans of a phantom mimicking stenosed carotids and in CTA scans of two patients with an internal carotid stenosis. In order to validate the measurements in CTA, measurements were also performed in three dimensional rotational angiography (3DRA) images of the same patients.

The validity of the approach for diameter measurements of cylindrical arteries in CTA-images is evident from phantom measurements. When prior knowledge about the enhancement and the blurring parameter was used, accurate and precise diameter estimates were obtained down to a diameter of 0.4 mm. The potential of the presented method both with respect to the extension to non-circular cross-sections and the modeling of adjacent calcifications appears from the patient data. The accuracy of the size estimates in the patient images could not be unambiguously established because no gold standard was available and the quality of the 3DRA images was often suboptimal.

We have shown that the inclusion of a priori information results in very accurate and precise diameter measurements of small cylindrical structures. Furthermore, in patient data the cylindrical model appears to be often too simple, and our extension to non-cylindrical lumens and adjacent calcifications results in realistic modeling of the carotid artery.

I. INTRODUCTION

Stenosis of the internal carotid artery may lead to neurological symptoms and is considered to be the major risk factor for ischemic stroke. Whether a patient will benefit from treatment, endarterectomy or endovascular stent placement, depends on the severity of the stenosis.[1-4] Digital subtraction angiography has historically been the gold standard to assess the severity of stenosis, but it has been shown that it can be replaced by the less invasive three dimensional techniques magnetic resonance angiography and computed tomography angiography (CTA).[5,6] CTA is often used for the quantification of carotid stenosis as it is relatively cheap and widely available.[7,8]

As manual measurements give rise to inter- and intra-observer variations, there has been an interest in automated methods in stenosis quantification in CTA. Methods described in the literature encounter various complications: they show a decreasing accuracy and precision in size measurements of smaller vessels,[9,10] are influenced by the convolution kernel used for the reconstructed images,[10] are dependent on the amount of contrast enhancement[11] and tend to have problems with the presence of calcifications.[12,13]

Underlying these problems is the blurring of the images, which is inherent in CT imaging. This blurring, which can be modeled by the convolution of the vessel geometry with a point-spread function (PSF), causes conventional methods[14,15] to inaccurately locate the vessel boundary, leading to a bias in size estimate.[16] The adequate dealing with this bias in measurements of the vessel size at the site of a stenosis is obviously of crucial importance for quantification of the stenosis.

Various approaches have been introduced to overcome this problem, each, however, with its own limitations. One method tries to reduce the average bias by the use of training datasets and specific imaging protocols.[17] This, however, limits applicability and results in reduced accuracy for small vessels as the bias depends on the diameter. Other methods[18,19] use special unbiased edge detectors using image derivatives. This procedure may be difficult or unreliable at the site of a stenosis as the signal-to-noise (SNR) is low at that site. To reduce the SNR problem the full-width at half-maximum (FWHM) criterion has been used, which is more robust in the presence of noise than the derivative-based edge detectors. The bias

of the FWHM criterion can be corrected if the PSF of the imaging system is known and cylindrical vessels are assumed.[20] However, obtaining FWHM values from the image data may be unreliable in vessels of only a few pixels in diameter.

Another option is a model-based approach, in which explicit allowance is made for the blurring of the image. In principle, this eliminates the bias in the diameter measurements. The fitting of a parametric model for size measurements has proved to be useful in projection images[21-23] and in three dimensional data.[24,25] Wörz et al[24,26,27] describe a model-based approach for vessel segmentation and quantification in which a vessel is modeled as a cylindrical tubular structure in a homogeneous background. However, vessels often are *not* cylindrical. Another complication is that calcifications may be present in the vessel wall, which affects the assumption of the homogeneity of the background.

In this paper, we propose a more extensive model-based approach for stenosis measurements in CTA images. In its basic form, a parametric image of a blurred circular disk-shaped cross-section of a cylinder is fitted to the cross-sectional image of a vessel. The extended model allows for both non-cylindrical vessel shapes and the presence of calcifications. The extension to more general shapes is obtained by the use of Fourier descriptors for the shape of the cross-section of the vessel.[28,29] When calcifications are present, both the lumen of the vessel and the calcifications are modeled to improve the diameter estimates of the vessel.

In model-based approaches of diameter measurements a considerable number of parameters have to be estimated. At sites of low SNR this may result in fits with poor precision. For small diameters the estimation procedure may be ill-defined because of a dependency of the parameters.[26,27] Three important parameters are the intensity of lumen and background, and the width of the PSF. In CTA the contrast enhancement of an artery is variable over different patients and scan protocols,[30,31] and the width of the PSF depends on the type of scanner and reconstruction filter. However, in a limited volume of interest of a single scan these three quantities are approximately constant, and reliable estimates can be obtained from the image data at sites with a high SNR. In the present paper, the consequences of the use of this prior knowledge of these three parameters are investigated for the accuracy and precision of diameter measurements.

Measurements were performed in phantom images and in CTA scans of patients with an internal carotid stenosis. To validate the diameter estimates in the clinical

images, two patients were selected for which the diameters could be measured in three dimensional rotational angiography (3DRA) images as well. In 3DRA the contrast of the arteries is greatly enhanced because the contrast is administered intra-arterial instead of intravenously, as is the case in CTA. Therefore these images have a higher SNR than CTA images.[32-34] Furthermore, calcifications are hardly visible in these images, thus eliminating one of the problems present in CTA.

II. MODELING OF BLOOD VESSELS IN CTA IMAGES

We assume a CT scanner to be a linear imaging system. In the absence of noise the image intensity $I(x,y,z)$ of a three-dimensional 3D attenuation coefficient distribution $\mu(x,y,z)$ can be described by the convolution of $\mu(x,y,z)$ with the 3D PSF $h(x,y,z)$:

$$I(x,y,z) = \mu(x,y,z) * h(x,y,z) \tag{1}$$

Strictly speaking, the PSF of a CT scanner is dependent on the position in the image. However, in a limited size of the region of interest, it is reasonable to assume the PSF to be shift invariant. For the relatively smooth kernels that are used in the reconstruction of CTA images, the PSF can be approximated with a 3D Gaussian function,[35] i.e.

$$h(x,y,z,\sigma_{xy},\sigma_z) = \frac{1}{2\pi\sigma_{xy}}\, e^{-(x^2+y^2)/2\sigma^2_{xy}}\, \frac{1}{\sqrt{2\pi\sigma_z}}\, e^{-z^2/2\sigma^2_z} \tag{2}$$

In Eq. (2) σ_{xy} and σ_z characterize the in-plane and the out-of-plane sharpness, respectively.

In CTA images blood vessels are enhanced due to the presence of contrast agent in the blood that has been administered intravenously to the patient. We consider an artery that is orthogonal to the xy-plane, with a diameter that changes relatively slowly in the z-direction. For the part of the internal carotid artery considered in this study both assumptions are reasonable. We will return to the limitations in the Discussion.

II.A. CYLINDRICAL MODEL

An artery is modeled by a homogeneous cylinder of contrast enhanced blood surrounded by homogeneous tissue. Consider a model image that contains a disk-shaped cross-section of the cylinder with radius R that is blurred by the PSF of the CT system. Because the cylinder is oriented in the z-direction, the PSF component in this direction can be omitted and the PSF is a 2D Gaussian with parameter $\sigma = \sigma_{xy}$.

It can be shown that the intensity of the model as a function of the distance r from the center of the disk shaped cross-section of the cylinder is given by:

$$f(r) = B + (A-B)\, e^{-\frac{r^2}{2\sigma^2}} \left(\sum_{k=0}^{\infty} \frac{2^{-k}}{k!^2} 2^{-k} \left(\frac{r}{\sigma} \right)^{2k} \left(k! - Gamma\left[1+k, \frac{R^2}{2\sigma^2} \right] \right) \right) \qquad (3)$$

with A and B the intensity of the artery and the background, respectively and σ the in-plane parameter of the PSF. In practice the summation is truncated at an upper limit k_{max} that is chosen to obtain an approximation of $f(r)$ within the machine precision.

The value of each pixel (x,y) of the model image equals $f(r)$ with r the distance of the pixel to the center (x_0, y_0) of the disk:

$$r = \sqrt{(x-x_0)^2 + (y-y_0)^2} \qquad (4)$$

The model image can therefore be described by six parameters: x_0, y_0, R, A, B, and σ.

II.B. EXTENDED MODEL

For adequate modeling of clinical images two extensions are made: (1) non-cylindrical arteries, and (2) structures in the background.

To allow for non cylindrical arteries, and thus for non-circular shapes of their cross-section, the model is extended by using polar Fourier descriptors to describe the outer contour.[28,29] Polar Fourier descriptors describe the radius as a function of the polar angle:[36,37]

$$R(\varphi) = R_0 + \sum_{k=1}^{n} a(k) \cos(k\varphi + \psi(k)) \tag{5}$$

with R_0 the radius of the basic circle, n the number of Fourier terms, and $a(k)$ and $\psi(k)$ the amplitudes and phase angles, respectively. For homogeneous backgrounds this model contains the six parameters of the cylindrical model, with R_0 instead of R, and in addition $2n$ Fourier parameters.

The second extension deals with structures in the background, such as one or more calcifications adjacent to the lumen of the artery, or another vessel nearby. In this case the model image contains multiple shapes, each one with its own set of parameters x_0, y_0, A, and Fourier parameters R_0, $a(k)$ and $\psi(k)$ (Eq. 5). The shapes have a common value for B, and σ.

The images for the extended model were calculated with a numerical method, see Sec. IV.B.

II.C. PARAMETER ESTIMATION

The parameters are estimated by fitting the model image to a region of interest (ROI) of the CTA image containing the artery and its surroundings. All parameters can be estimated in the fitting process, but it is also possible to use *prior knowledge* for the three parameters $A, B,$ and σ. The intensity A of the vessel can be assumed to be constant within the relative small volume that contains the arteries, because of the venous injection of the contrast agent and the mixing of contrast and blood between the site of injection and the site of the scan. The constancy of B is also often a reasonable assumption. The value of σ depends on the scanner used and the scanning protocol but is constant within one examination.

In our approach $A, B,$ and σ are estimated in a part of the vessel with a large diameter, and thus with a high SNR. These estimates are used as prior knowledge at the site of a stenosis, where the SNR is lower.

III. DATA ACQUISITION AND PREPROCESSING

III.A. CT SCANS

A 64 slice CT scanner (Brilliance 64, Philips Healthcare, Best, The Netherlands) with a collimation of 64 x 0.625 mm was used. Spiral scans were made using a rotation time of 0.75 s, high resolution, pitch of 0.765, 120 kV and 265 effective mAs. Images were reconstructed on a 512 x 512 matrix with a field of view (FOV) of 150 mm, a nominal slice width of 0.9 mm, a slice increment of 0.45 mm, and reconstruction kernel B.

III.B. PHANTOM

The accuracy and precision of the diameter measurements using the cylindrical model was investigated with a phantom mimicking the neck with four arteries near the center. The phantom was made of nylon and consisted of a cylinder with 110 mm diameter containing a smaller cylinder, with 50 mm diameter, both with a length of 100 mm. The 50 mm cylinder contained a number of cylindrical holes, each one with a length of 45 mm, 15 mm from the center of the phantom. Two sets of 50 mm cylinders were used, which contained four holes with diameters of 6.0 and 4.0 mm, respectively, and smaller holes, with diameters of 2.4, 1.2 and 0.6 mm, and 2.8, 1.6, 0.8 and 0.4 mm, respectively.

The holes were filled with a water diluted contrast agent (Visipaque 320 mg I/mL, 1:24), to obtain a contrast comparable to that in a typical clinical scan. The phantom was scanned with its axis aligned in the z-direction.

The diameter of the circular cross-section of each cylinder was estimated in approximately 40 axial images, 1 mm apart.
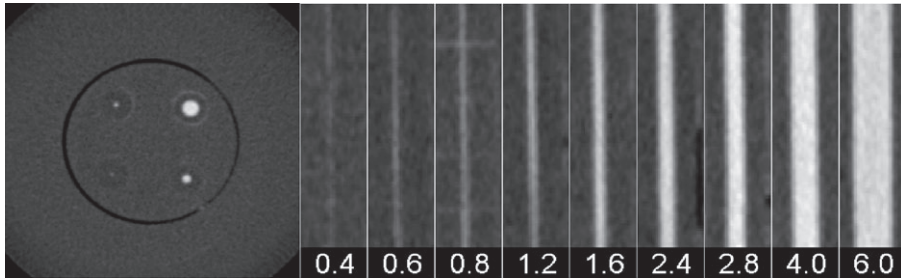
Fig. 1

On the left an axial image through the phantom with the 50 mm cylinder with holes with diameters of 2.8, 1.6, 0.8 and 0.4 mm. The holes are filled with a water diluted contrast agent. On the right sagittal images through the center of the holes with different diameters. Window center 200 HU, window width 400 HU.

III.C. PSF MEASUREMENTS

The values for σ obtained using the model fitting were compared to the PSF determined in a conventional way. A scan was made of a small block of polyvinyl chloride (PVC) of approximately $3 \times 4 \times 4$ cm^3, with a CT value of approximately 1100 HU. It was scanned in a small water-filled PMMA cylinder (outer diameter 70 mm) and CT images were acquired using the acquisition and reconstruction parameters listed in Sec. III.A. In both the x- and y-direction five images of 80 by 50 pixels orthogonal to the edge of the cube were used to estimate σ by fitting a convolution of a Gaussian and a step edge.

III.D. PATIENTS

III.D.1. CTA IMAGES

To test the feasibility of the method in clinical data we performed size measurements of the cross section of the internal carotid artery in CTA images of two patients. For these two patients also 3DRA images were available (see below). Patient #1 was scanned on the 64-slice scanner, patient #2 was scanned on a 4-slice CT scanner (Mx8000 Quad, Philips Healthcare, Best, The Netherlands). The acquisition and reconstruction parameters of the 64-slice scanner are listed in Sec. III.A. For the 4-slice scanner, the same acquisition parameters were used, apart from a collimation of 4 x 1 mm and a pitch of 0.875. For this scanner the nominal slice width was 1.3 mm and the slice increment 0.5 mm.

On the 64-slice scanner the patient was scanned from just below the aortic

arch to just above the circle of Willis and 80 mL contrast agent (Visipaque 320 mg I/mL) was injected at a rate of 4 mL/s. On the 4-slice scanner, the patient was scanned from just above the shoulders to just above the circle of Willis and 120 mL contrast agent was injected. For both scanners the scanning delay was automatically adjusted by a bolus-tracking technique.

III.D.2. 3DRA IMAGES

3DRA examinations were performed on a single-plane angiographic unit (Integris Allura Neuro; Philips Medical Systems) using propeller rotation.[38] While 15- to 21-mL contrast agent (Visipaque 320 mg I/mL) at 3 mL/s was injected through a 6F catheter positioned in the common carotid artery (CCA), 100 projection images were acquired during a 240° rotational run in 8 seconds. Images were reconstructed on a 256 x 256 matrix, with a FOV of 70 mm and a slice increment of 0.27 mm.

III.D.3. REGISTRATION OF CTA AND 3DRA IMAGES

To spatially relate the CTA and 3DRA size measurements, the external and internal carotid artery were segmented. This segmentation was used for registration of the two modalities and was performed with open source software available in the Vascular Modeling Toolkit.[39] An initial segmentation was performed by placing seed points in all the vessels of interest and applying a colliding fronts method[40,41] using a lower threshold of 150 HU and an upper threshold of 400 HU in CTA. For 3DRA images only a lower threshold was used with a value halfway between the average background value and the average lumen intensity. Next, a segmentation was performed using a geodesic level set segmentation method based on the image gradients.[42] In the case of CTA images a correction was included for the presence of high intensity structures as bone and calcifications (defined with a lower threshold of 450 HU).[43] The surfaces of the segmented arteries in the 3DRA images and CTA images were registered using an iterative closest point registration.[44] Registered surfaces are shown in Fig. 5. In the CTA images a centerline was determined through the segmented internal carotid artery based on solving Eikonal equation on a Voronoi diagram.[40] Cross-sectional images perpendicular on this centerline were made of the internal carotid artery from both CTA and 3DRA using cubic

interpolation with a pixel size of 0.1 mm, an image size of 128^2 pixels centered on the artery, and an increment of 0.5 mm.

III.D.4. SELECTION OF CTA AND 3DRA IMAGES

For each patient the section containing the stenosis was selected in the carotid artery, and two reference sections, one proximal and the other distal to the stenosis. The reference sections were chosen in order to obtain estimates of the parameters *A, B,* and σ to be used as prior knowledge in the estimation of the diameter in the stenosed section. *Two* reference sections were chosen in order to have a check on the invariance of these parameters. The first reference section was in the common carotid just below the bifurcation, the second reference section was in the internal carotid a few cm distal to the site of stenosis. The sections have a length of 4-10 mm, and in a section 8-20 images were analyzed.

IV. FITTING OF IMAGES – PRACTICAL ASPECTS

IV.A. PHANTOM DATA; CYLINDRICAL MODEL

In the fitting procedure a circular ROI with a diameter of 8 mm around the center of each cylinder was used. The cylindrical model was fitted by minimizing the root mean square (RMS) differences of the pixel values of the real image and the model image using the down-hill simplex method.[45] For fast convergence of the fitting procedure, it is important to have good initial parameter values. First the maximal intensity value within the ROI was determined. The background value within the ROI was estimated by calculating the average value of a ring two pixels wide at the border of the ROI. A segmentation of vessel and background was obtained by tresholding the image with the average of these two values. In case more than one connected region was present within the ROI after thresholding, a situation that sometimes occurred with small cylinders due to the presence of noise with high intensity, the connected region closest to the center of the ROI was considered to be the cylinder cross-section.

The coordinates of the center of gravity of the cylinder cross-section were taken as initial values for (x_0, y_0). The equivalent radius $(\sqrt{S/\pi})$ was used as the initial value of R, with S the area. The mean values of the intensity of cylinder cross-section and background were used as initial value of A and B. A default value of 0.5 mm was used as initial value of σ.

This procedure did not provide reliable initial values of R and A for very small cylinders, i.e. for diameters less than one mm. In this case a somewhat more involved initialization for R was used, as described in the Appendix, and a default value of enhancement $A-B$ of 300 HU, a value that is within 20% of the actual value in the phantom. The exact choice of this default value was not critical. A was thus initialized with $B + 300$.

All diameters were estimated using six parameters of the cylindrical model. For diameters less than 4 mm the model fitting was also performed with three parameters to be estimated (x_0, y_0, R) and fixed values for $A, B,$ and σ, obtained as mean estimates in the fit of the 6 mm or 4 mm cylinder.

In the simplex method the initial step size has to be specified as well. The initial step sizes that were used are listed in Table I.

Table I
The initial step sizes used in the simplex minimization method.

Parameter	Step size
dx_0 and dy_0	0.4 mm
dR	0.2 mm
$d(\sigma)$	0.1 mm
dA	50 HU
dB	25 HU

In the simplex algorithm a maximum of 500 iterations was chosen. Once a minimum is found, it is customary to restart the procedure at least once, with the parameter values for which the minimum error was obtained used as initial values, and check whether a true minimum has been found.[46] When after the restart the minimum was not yet reached, we continued with restarts until the RMS difference of real image and model image remained constant.

As a check for the accuracy and precision of the numerical approximation used in the fitting of the extended model (see Sec. IV.B), model images were fitted to the phantom images using this numerical approximation as well.

IV.B. PATIENT DATA; EXTENDED MODEL

For each patient image a ROI containing the artery of interest was determined by thresholding. A threshold between 150 and 200 HU appeared to be adequate to separate artery and background. In case one or more calcifications were present contiguous to the artery a second threshold was applied with a value between 300 and 400 HU, depending on the maximal intensity of the lumen. Connected regions with intensities exceeding the high threshold corresponded to one or more calcifications. An approximation of the artery was obtained by opening[37] the structure consisting of the remaining pixels (three times with a 3x3 mask) in order to clean up this structure.

For the 3DRA images no absolute threshold could be specified; for each patient a threshold was chosen empirically for the initial segmentation of the artery. In these images the relative contrast of the calcifications was very low; therefore they were disregarded in the fitting procedure.

For each ROI the background region was defined as a border with a width of 1 mm (10 pixels) around the thresholded artery; all pixels at larger distance were set to zero. When one or more calcifications were present, only the part of the calcification within the border region was retained within the ROI. This proved to be advantageous in the fitting of the model, especially for calcifications with a complex shape. When another artery was present within the border region, as background region a border with a width of 1 mm was chosen around both arteries together.

For the extended model a numerical approximation was used. In this approximation we consider an image in which pixels with centers within the boundary defined by Eq.(5) have value A, and the other ones value B. This image is blurred by convolution with a Gaussian kernel. Because of the separability of this kernel, the 2D convolution was performed by two successive convolutions with a 1D Gaussian kernel in the x- and y-direction. This kernel was truncated at 3σ from the center. A pixel size of 0.1 mm was used.

The fitting of the extended model was also performed with the downhill simplex method. Initial values for x_0, y_0, A and B were determined as described for the phantom in Sec. IV.A. Different numbers of Fourier terms were tried, depending on the shapes involved. Initial values for R_0 and the Fourier terms were obtained in the following way: A rough estimate of the radius $R(\varphi)$ was determined from the initial center (x_0, y_0) to the boundary for 64 angles in $[0,2\pi)$, and smoothing was applied with a moving average over 9 angles. Initial values for R_0 and the amplitudes and phase angles a(k) and $\psi(k)$ were obtained by calculating the discrete Fourier transform of this smoothed version of $R(\varphi)$. For σ again an initial value of 0.5 mm was chosen.

In the fitting of an image containing an artery with one or more calcifications, often overlap between lumen and calcification in the model image occurred. The reason of this overlap was that the shape of the lumen was described with only a few Fourier terms, and that much more terms would be needed to describe the contour excluding the calcification adequately. In case of overlap, the pixels in the model image before blurring were set to the highest value, i.e. to the intensity of the calcification.

The reference sections were fitted without prior knowledge, i.e. with all parameters free. For the CTA images in the stenosed section, the model was fitted both without and with prior knowledge. In this last case estimates of A, B and σ were used obtained from the reference sections. For the 3DRA images we did not use prior knowledge because the enhancement of the carotid artery may vary substantially within a range of a few cm.

The initial step sizes of Table I were used, with step sizes of 0.1 mm for the amplitudes and 0.5 radian for the phase angles of the Fourier terms. If after 15 restarts convergence had not yet been reached the minimization procedure was terminated and the last parameter estimates were used. The equivalent diameter

of the artery was estimated as $2(\sqrt{S/\pi})$, with S the area of the shape describing the artery. In case overlap occurred with one or more calcifications, S was taken to be the area of the shape of the artery minus the area of the overlapping region.

V. RESULTS

V.A. PHANTOM DATA

The estimated diameters using the cylindrical model with all six parameters are shown in Fig. 2 and in Table II. Although the accuracy of the diameter estimates is satisfactory, the standard deviation for diameters less than 1.5 mm increases sharply. This increase in SD is also present for σ and A. This is caused by the fact that for small diameters only two of the three parameters D, A and σ are independent, where we have taken for simplicity B to be constant. Thus unambiguous estimation of all three parameters is not possible, and the use of prior knowledge of at least one of these parameters is mandatory.[27] This dependency appears from the high correlation between D, z, σ and A in this range (see Fig. 3 for an example), and the large number of restarts that is needed to obtain convergence (Table II).
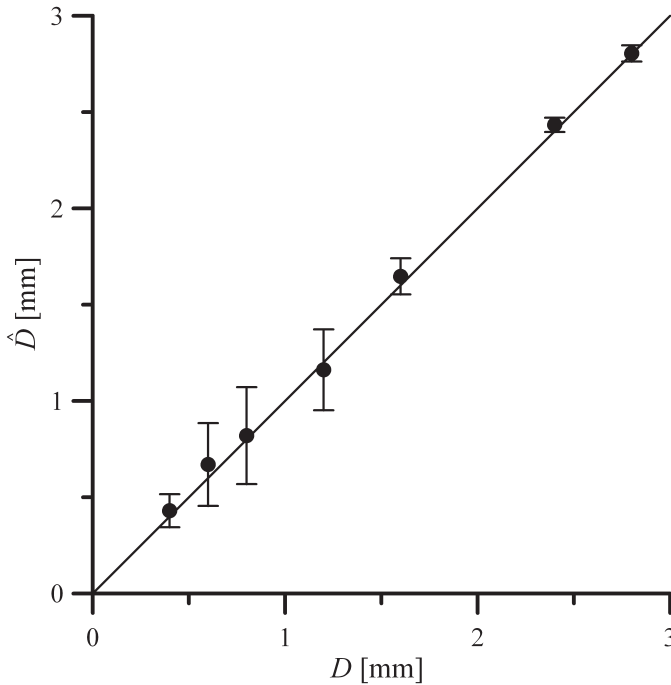
Fig. 2
Average estimated values of the diameter $D \pm 1$ standard deviation, using the cylindrical model with six parameters. The line of identity is also shown. In order to facilitate comparison with **Fig. 4** in this figure measurements up to 3 mm are shown. Estimated values for 4 and 6 mm can be found in Table II.

Table II
Average estimated values of the diameter $D=2R$, σ, A and B, and their standard deviations, using the cylindrical model with six-parameters. The values of A and B in phantoms #1 and #2 are slightly different.

| Scan	D (mm)	# images	$\hat{D}$ (mm)		$\hat{\sigma}$ (mm)		$\hat{A}$ (HU)		$\hat{B}$ (HU)		# restarts	
			Av.	SD	Av.	SD	Av.	SD	Av.	SD	Av.	range
1	6.0	173	6.01	0.046	0.406	0.014	335	2	82	2	1.3	1-3
2	4.0	164	4.06	0.031	0.407	0.011	359	2	87	1	1.3	1-3
2	2.8	41	2.80	0.042	0.411	0.017	365	6	86	2	1.8	1-8
1	2.4	46	2.43	0.037	0.416	0.019	346	8	78	2	1.5	1-4
2	1.6	47	1.65	0.094	0.416	0.031	365	35	84	1	2.1	1-8
1	1.2	46	1.16	0.210	0.422	0.049	421	185	77	1	3.8	1-9
2	0.8	39	0.82	0.252	0.395	0.051	410	159	85	2	5.4	1-22
1	0.6	41	0.67	0.215	0.424	0.065	412	128	78	2	4.7	1-11
2	0.4	36	0.43	0.086	0.439	0.101	390	41	86	1	3.1	1-12

Av.: average; SD: standard deviation.
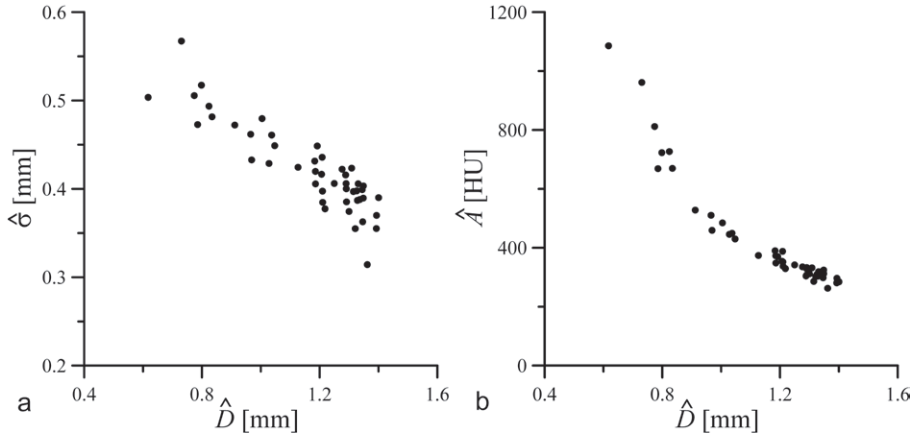
Fig. 3
Relation between estimated values of (a) the diameter $(\hat{D})$ and sigma $(\hat{\sigma})$ and (b) the diameter $(\hat{D})$ and the intensity $(\hat{A})$ of the cylindrical hole with a diameter of 1.2 mm.

The estimated diameters using three free parameters (x_0, y_0 and R) and fixed values for A, B and σ, are shown in Fig. 4 and in Table III. Here both the accuracy and precision are satisfactory.

Fig. 4 also displays the diameter estimates according to the FWHM-criterion, and the estimates based on the second order derivative zero-crossing, calculated using Eq. (2). This figure demonstrates the range of diameters for which these methods lead to a bias (for $\sigma = 0.4$, the value of the phantom study).

Because of the impossibility to estimate the smallest diameters unambiguously when all six parameters are used, the verification of the diameter estimation using the numerical approximation was performed with three free and three fixed parameters only, for diameters between 0.4 and 2.8 mm. An excellent agreement was obtained, with differences of maximal 3 μm between average diameters obtained with both methods, and virtually identical Ds.
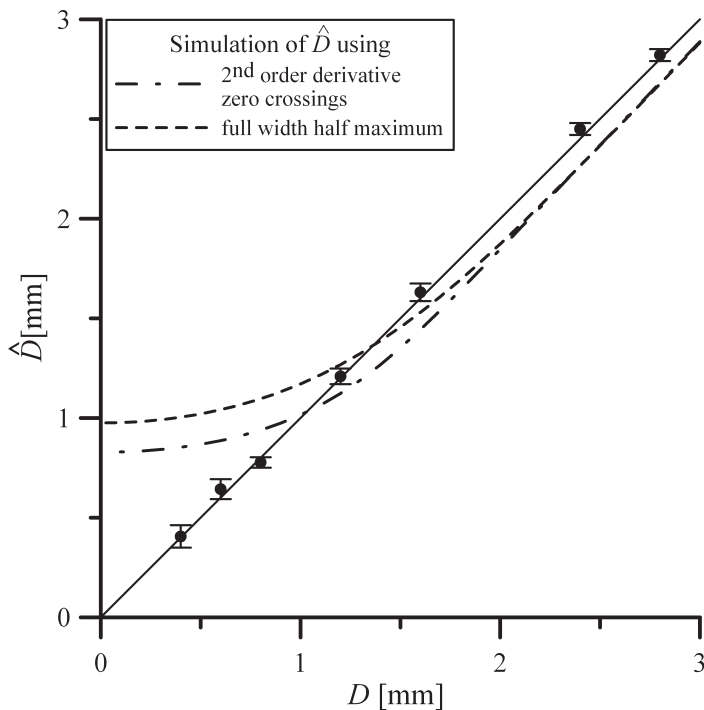
Fig. 4
Average estimated values of the diameter $D \pm 1$ standard deviation, using the three-parameter cylindrical model, in which prior knowledge of σ, A and D is used. The upper curve shows the diameters when the full width half maximum criterion is used, the lower curve displays the diameters as determined using second derivative zero-order crossing. The line of identity is also shown.

Table III
Average estimated value of the diameter D=2R and standard deviation, using the cylindrical model with three free parameters, and prior knowledge of σ, A and B. The average number of restarts for convergence was between 1.1 and 1.2.

Scan	D (mm)	# images	Z (mm)	
			Av.	SD
2	2.8	41	2.82	0.030
1	2.4	46	2.45	0.030
2	1.6	47	1.63	0.044
1	1.2	46	1.21	0.039
2	0.8	39	0.78	0.026
1	0.6	41	0.64	0.050
2	0.4	36	0.41	0.056

Av.: average; SD: standard deviation.

V.B. PSF MEASUREMENTS

The value of σ_{xy} measured in the scan of the PVC cube was 0.414 mm (SD 0.012 mm). This value is nearly the same as the most precise estimates of σ_{xy} obtained from the phantom data with the cylindrical model (0.406-0.416 mm; Table II).

V.C. PATIENT DATA

Fig. 5 shows the registered surfaces of the carotid arteries of both patients. The reference sections and stenosed sections are indicated.
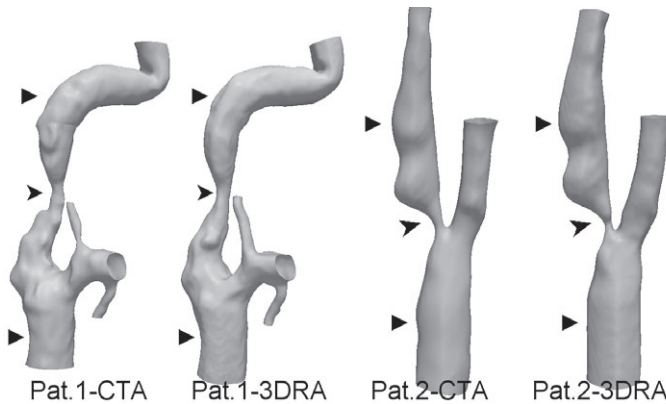

Fig. 5
Registered surfaces of CTA images and 3R-RA images of both patients. The center of the stenosis part is indicated with an arrow head and the center of the reference sections are indicated with a triangle.

V.C.1. REFERENCE SECTIONS

The cross-section of the carotid of patient #1 was somewhat elongated in the proximal section, while in the distal reference section, and in both reference sections of patient #2 it was reasonably circular. A typical example of a non-circular carotid cross section of patient #1 is shown in Fig. 6; Fig. 6a shows the CTA image and Fig. 6d the 3DRA image. The extended model was fitted using 0, 2, 4, 6, and 8 Fourier terms, respectively. Fitted model images with 6 Fourier terms and the contours are shown in Fig. 6b, c, e and f. Number of restarts before convergence, RMS error and parameter values for the CTA image are shown in Table IV.
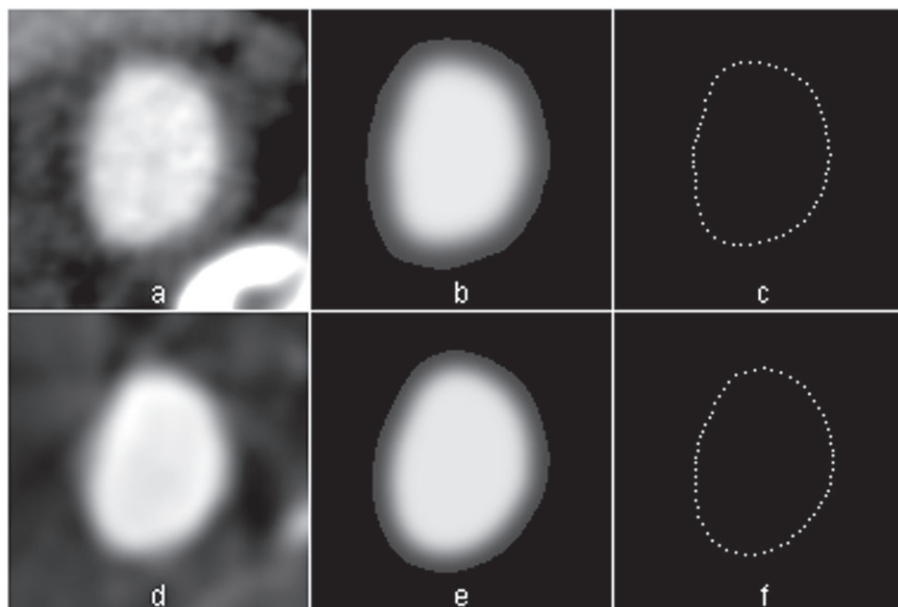
Fig. 6
 Cross-sections of the common carotid of patient #1, image #2, 1 mm from the beginning of the proximal section.
(a) shows the CTA-image and (d) the 3D-RA image. The other figures show the fitted model images (middle column) and contours (last column) for CTA (upper) and 3D-RA (lower), using 6 Fourier terms. Each image measures 12.8 x 12.8 mm2.

Table IV
Details of the fit of a model image to the CTA image of Fig. 6a. The number of Fourier terms increases from 0 (i.e. a circle) to 8. In Fig. 6b a fitted image with n=6 is shown.

n (# FDS)	# restarts	RMS err. (HU)	$\hat{D}$ (mm)	$\hat{\sigma}$ (mm)	$\hat{A}-\hat{B}$ (HU)
0	3	49.6	6.58	0.591	282.9
2	7	19.4	6.75	0.477	300.3
4	5	15.2	6.73	0.469	300.2
6	3	13.5	6.72	0.463	299.5
8	6	13.0	6.73	0.465	300.5

RMS err.: root mean square error.

From visual inspection it appears that 4 to 6 Fourier terms are adequate to describe this kind of shape, and, because the other cross-sections in the reference sections were more circular than this one, adequate for all reference sections. It is evident that the estimated value of the equivalent diameter is not very sensitive for
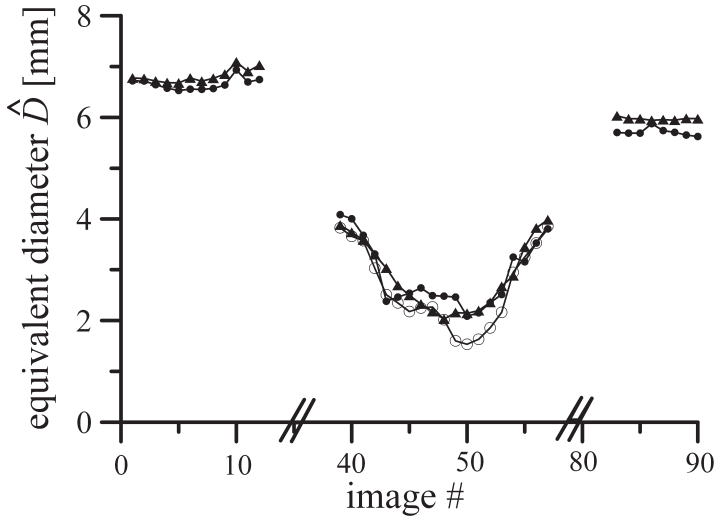
Fig. 7
Estimated diameters of the carotid of patient #1. Left and right are the diameters of both reference sections; in the middle of the stenosed section. CTA measurements are indicated with circles; 3D-RA measurements with triangles. Open circles indicate estimated diameters using prior knowledge (Table V). In the reference sections 6 Fourier terms were used. In the stenosed section for the CTA images 0 Fourier terms were used for the arteries (i.e. circles were fitted), and 2 Fourier terms were used for the calcifications. For the 3D-RA images 2 Fourier terms were used for the artery.
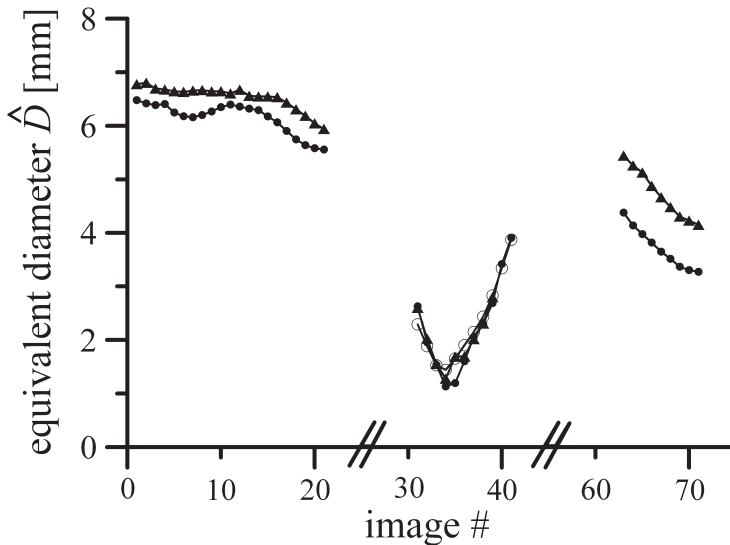

Fig. 8
 Estimated diameters of the carotid artery of patient #2. For the arteries in the stenosed section 2 Fourier terms were used (3 for the external carotid; results not shown). For the two last 3D-RA images in the stenosed section no reliable diameter estimates could be obtained because of the artifacts in these two images. Further details as in **Fig. 7**.

the number of Fourier terms used; the diameter is virtually constant for $n=2$ and higher. In the example shown in Fig. 6, with 6 Fourier terms, the estimated equivalent diameter of the 3DRA image is 6.72 mm, the same value as for the CTA image.

Fig. 7 and Fig. 8 (at the left and right side) show the estimated diameters for the reference sections for both patients. For patient #1 the agreement between the diameters derived from CTA images and 3DRA images is fair to good. For patient #2, however, the estimated diameters are systematically higher for the 3DRA images. This is caused by severe artifacts in the 3DRA images for this patient, which causes the average value of the surrounding of the artery to vary considerably, which results in poor fits of the model images to the 3DRA images (see Fig. 9). For the CTA-images the intensities within and outside the artery, $\hat{A}$ and $\hat{B}$, and blurring parameters $\hat{\sigma}$, are on the average nearly the same in the proximal and distal reference section. This is evident from the relative low values of the SD which is determined from the collection of measurements at the proximal and distal reference section (Table V)
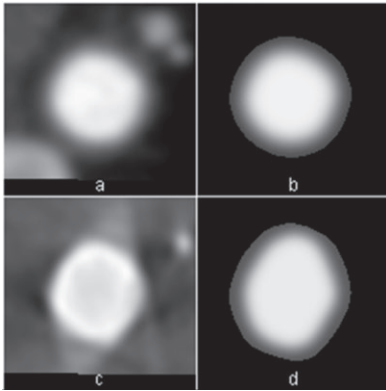

Fig. 9
Cross-sections of the common carotid of patient #2, image #7 (3 mm from the beginning of the proximal section). (a) shows the CTA-image and (c) the 3DRA image. (b) and (d) show the fitted model images, using 6 Fourier terms. Note the severe streak artifacts in the 3DRA image (c), with background values varying between -400 and 800, with the intensity of the artery in the order of 1800 (all arbitrary units), and edge enhancement of the artery. These artifacts cause deviations in the shape of the artery, see (c) in comparison with (a), and a very poor fit (d). Each image measures 12.8 x 12.8 mm2.

Table V
Mean values and standard deviations of $\hat{\sigma}$, $\hat{A}$ and $\hat{B}$ for the reference sections of the CTA images of patient #1 and #2. These data are used as prior information in the sections with a stenosis.

Patient #	$\hat{\sigma}$ (mm)		$\hat{A}$ [HU]		$\hat{B}$ [HU]	
	Av.	SD	Av.	SD	Av.	SD
1	0.467	0.017	346	12	55	6
2	0.570	0.016	469	6	24	7

RMS err.: root mean square error.

V.C.2. SECTIONS WITH STENOSIS

In the stenosed section of patient #1 calcifications were present (Fig. 10). In patient #2 the stenosed section was immediately above the carotid bifurcation (Fig. 11, see also Fig. 5), and we included both arteries above the bifurcation in the model images for this patient.

For the images in the stenosed section sometimes a large number of restarts was needed to obtain convergence, especially when no prior knowledge was used. In this situation 7 to 15 restarts (the maximal number used) were used. With the use of prior knowledge in the order of 4 to 8 restarts were required, and incidentally more.
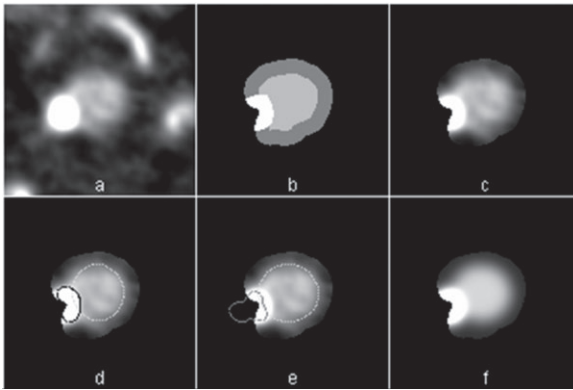
Fig. 10
(a) Cross-section in the proximal part of the stenosed section of patient #1 with calcification (**Fig. 7**, image #39); (b) ROI with initial segmentation of the artery (light grey) and border (dark grey; calcification white); (c) ROI; (d) initialization with n=2 for the artery and n=4 for the calcification; (e) fitted contours and (f) fitted shapes, using prior knowledge (Table V, patient #1). Each image measures 12.8 x 12.8 mm2.

Fig. 11
(a) Cross-section just above the bifurcation of the carotid of patient #2 (**Fig. 8**, image #32); (b) and (c) fitted images without and with prior knowledge (Table V, patient #2). For the internal and external carotid (middle and right) 2 and 4 Fourier terms were used, respectively. Each image measures 12.8 x 12.8 mm2.

Because of the smaller dimensions and the lower contrast of the arteries in the stenosed section, for adequate modeling a smaller number of Fourier terms were used than for the cross se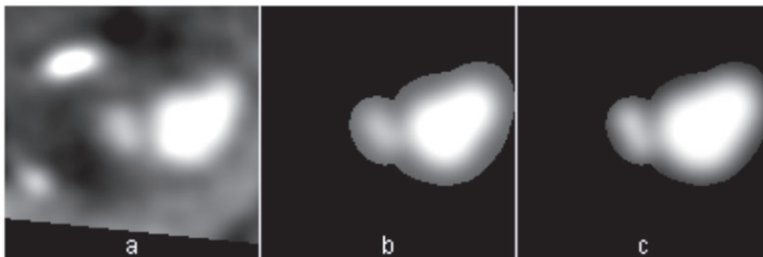ctions of the reference sections. For the stenosed artery of patient #1 zero terms were used (i.e. a circle was fitted), because of the poor quality of the images (see Fig. 12); for patient #2 two terms were used for the internal carotid, and 4 for the external carotid. For the calcifications 2 to 4 terms were adequate.

In Fig. 7 and Fig. 8 (middle) the estimated diameters in the stenosed section are shown. It appears that for the smallest diameters (in the order of 2 mm and smaller) some systematic differences exist between the CTA diameter estimates without and with use of prior knowledge (Table V). The 3DRA estimates, which were only obtained without the use of prior knowledge, appear to have a better agreement with the CTA estimates obtained without using prior knowledge for patient #1. For patient #2 no systematic differences are present in this respect. The value of a comparison with the 3DRA estimates is limited, however, because the quality of the 3DRA images is often rather poor due to the artifacts in the reconstructed images (see Fig. 9 and Fig. 12).
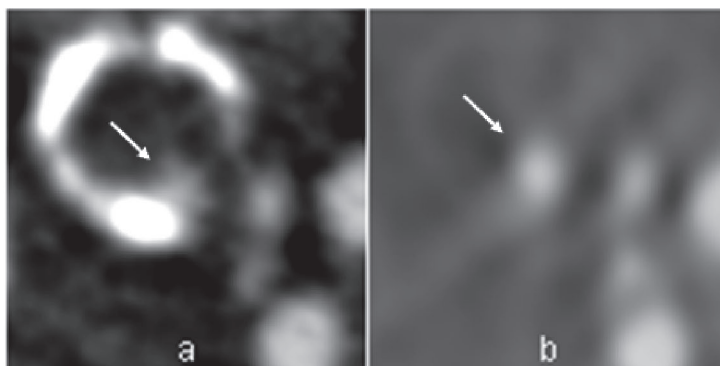

Fig. 12
(a) CTA image at the site of maximal stenosis of patient #1(**Fig. 7**, image #27); (b) 3D-RA image at the same site. The calcification is virtually invisible in this image due to the relatively low contrast in comparison with the intravascular contrast; note the streak artifacts. The carotid is indicated in both images with an arrow. Each image measures 12.8 x 12.8 mm2.

VI. DISCUSSION

The value of the presented model-based approach for diameter estimation of arteries in CTA-images in which prior knowledge is used of essential parameters is evident from phantom measurements. We have shown that this approach can also be applied to the modeling of non-cylindrical arteries, with adjacent high-density structures, such as calcifications.

We first discuss the importance of the use of prior knowledge. A few years ago Wörz and Rohr demonstrated that when vessels are modeled as blurred cylinders, the use of prior knowledge is indispensable for the estimation of the diameter of *small* vessels.[27] This can be readily understood, because when the radius of a blurred cylinder decreases, the intensity as function of the distance of the center $f(r)$ (Eq. 3) becomes virtually indistinguishable from a Gaussian. Apart from the location parameters, a Gaussian can be described by two parameters, amplitude and σ, and thus of the three parameters of our model R, $(A-B)$ and σ, only two are independent. For the present study, with $\sigma = 0.4$ mm, this appeared to be the case for diameters in the order of 1.5 mm and less. In the phantom study it appeared that, when prior knowledge was used, accurate and precise diameter estimates could be obtained down to 0.4 mm. For diameters larger than 1.5 mm the use of prior knowledge was not essential, but still advantageous, as this improved the precision of the estimates.

In clinical data the advantage of the use of prior information could not be established unambiguously. Improvement can be expected in smaller vessels and these were not present in the two patients of this study. To obtain improved estimates in patients, the enhancement at the site of the stenosis has to be approximately the same as at the reference site, and the border between artery and surrounding tissue must have a blurring that is adequately described by the PSF determined at the reference site. For the CTA-images of this study both conditions appear to be met. The average intensity before and after stenosis was nearly the same, and there is no reason to suspect that at the stenosis site the intensity was different. The parts of the carotid artery that were analyzed were nearly orthogonal to the xy-plane (Fig. 5), so that the blurring can be expected to be constant in the part of the carotid that was analyzed.

The other important point of this study is the generalization to the modeling of non-cylindrical arteries and adjacent high-density structures. Model-based studies until now were restricted to vessels with circular cross-sections in homogeneous backgrounds. Circular cross-sections, however, appear to be more the exception than the rule, and calcifications in the vessel wall or other vessels nearby are also fairly common.

In this study we used polar Fourier descriptors to describe non-circular shapes. Results from two patients show that this approach is feasible, and that it performs reasonably well.

A choice has to be made of the number of Fourier terms that is used. In the two patients in the present study the non-stenosed carotids could be adequately described with 4 to 6 terms. It is interesting to note that although the use of a higher number of terms was important for an adequate description of the artery cross-section, the choice of the number of terms influenced the values of the estimated equivalent diameters only in a minor degree. Within the stenosed sections, with smaller arteries and less contrast, fewer terms were used because under these conditions the use of too many Fourier terms could result in oscillating contours. Although most high frequencies disappeared in the final image because of the smoothing applied, oscillating contours are most likely not in correspondence with the real situation in the body. Also in this case, the estimated equivalent diameter was not largely influenced by the number of Fourier terms used.

The accuracy of the diameter estimates in the clinical images could not be established unambiguously, because no gold standard was present. We tried to validate these measurements with diameter estimates using matched 3DRA images. As the signal-to-noise ratio of the carotids is much higher in 3DRA images than in CTA images we expected more precise measurements in 3DRA images. However, the quality of these images was often impaired by the presence of artifacts, which showed up as shading in the background, and/or inhomogeneities in the enhancement within the arteries. In future studies the quality of 3DRA images could possibly be improved, for instance by incorporating a better beam hardening correction and ECG-gating. In that case, 3DRA could be a more useful standard for the judgment of the performance of the present method in CTA images.

The presented method has some limitations. As mentioned above, the part

of the carotid artery that was analyzed was approximately orthogonal to the *xy*-plane, and therefore the blurring can be adequately by one parameter, σ_{xy}. This is no longer the case when the artery is not orthogonal to the *xy*-plane and the out-of-plane blurring parameter σ_z differs from σ_{xy}. However, in this case the blurring can be made isotropic by preblurring in-plane or out-of-plane before the analysis is carried out.[20,24]

An additional limitation is that the method presented in this article is essentially 2 dimensional. A next step should be the implementation of a similar method in 3D, in which 3D parametric shapes are fitted to a volume of interest containing the artery. Some problems encountered in the present study should be alleviated when a 3D method is used. In the first place, the signal to noise ratio would effectively increase, because the information of a number of neighboring images is combined in the fitting procedure. Secondly, the approach would also be feasible in vessels which do show abrupt diameter changes.

In conclusion: this study stresses the importance to use prior knowledge when the diameter of narrow blood vessels is estimated with a model-based method, and presents a new approach to obtain realistic modeling of blood vessels in patient data.

APPENDIX

INITIAL VALUE OF THE EQUIVALENT DIAMETER FOR SMALL VESSELS

The initial value for the equivalent diameter or radius of small vessels (diameter 1 mm or less) was obtained by using the property that the integrated intensity $I_{blurred}$ of a blurred detail is the same as the integrated intensity I_{sharp} of the unblurred detail, both relative to the background. We first discuss the continuous situation (see Fig. 13).
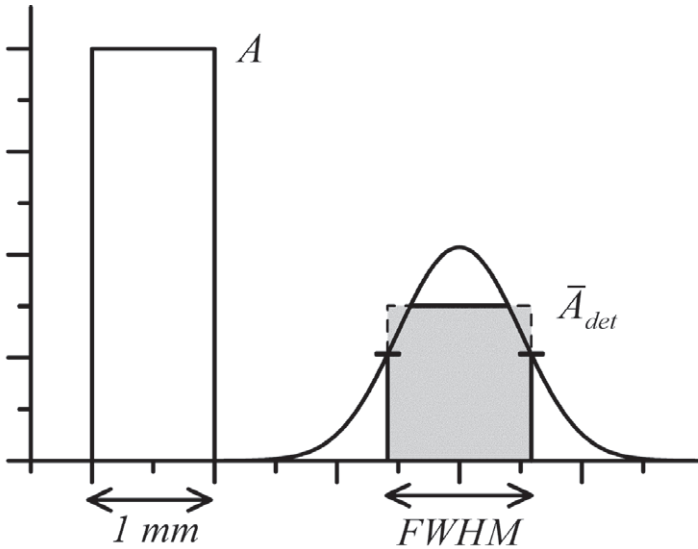
Fig. 13

Cross-sections of the 2D intensity profiles of a disk-shaped detail with a diameter of 1 mm and intensity A (left), and of the same detail blurred with a Gaussian PSF with a σ of 0.4 mm (right). The integrated intensity of the unblurred detail is the same as that of the blurred detail. $\bar{A}_{det}$ is the mean intensity within the full width at half maximum ($FHWM$). In this example $B = 0$. The integrated intensity of the blurred detail can be approximated with the integrated intensity within the $FHWM$ multiplied by a factor $f > 1$ to allow for the tails that are not included in the integration. For a Gaussian profile, which is a good approximation to the true intensity distribution in this example, $f > 2$

For a disk-shaped detail:

$$I_{sharp} = \pi R^2 (A{-}B) \qquad (6)$$

with R the radius of the disk and A and B the intensity of disk and background.

To avoid problems with the integration of the intensity of the blurred detail that will be encountered in practice, because of the (in principle) infinite integration limits and the presence of noise, we calculate $I_{blurred}$ as the integral within the full width at half maximum (*FWHM*), multiplied with a factor *f* to allow for the tails that are not included in the integration:

$$I_{blurred} = f.\pi R_{HM}^2 \, (\overline{A}_{det} - B) \qquad (7)$$

with $R_{HM} = FWHM/2$ and $\overline{A}_{det}$ the mean intensity within the *FWHM*. For a Gaussian profile $f=2$, and this value is also a good approximation for blurred disks with a diameter of 1 mm or less (for $\sigma = 0.4$ mm).

In the discrete situation we start with an initial segmentation of vessel cross-section and background, obtained by thresholding at half of the maximal value of the vessel cross-section relative to the background. The area of the vessel cross-section is S_{vessel}, its mean intensity $\overline{A}_{vessel}$ and the mean intensity of the background $\overline{B}_{bg}$.
Then

$$I_{measured} = f.S_{vessel}(\overline{A}_{vessel} - \overline{B}_{bg}) \qquad (8)$$

Because I_{sharp} (Eq. 8) $\cong I_{blurred}$ (Eq. 7) $= I_{sharp}$ (Eq. 6), we can initialize the equivalent radius R with

$$R_{ini} \cong \sqrt{\frac{f.S_{vessel}(\overline{A}_{vessel} - \overline{B}_{bg})}{\pi(A-B)}} \qquad (9)$$

with $f=2$. For $(A-B)$ a default value was used, see the main text.
We finally note that initialisation (Eq. 9) can be used for small cross-sections of arbitrary shape as well. In the two patients analysed in this study these small cross-sections did not occur, however.

REFERENCES

1   "Endarterectomy for asymptomatic carotid artery stenosis. Executive Committee for the Asymptomatic Carotid Atherosclerosis Study," Jama 273 (18), 1421-1428 (1995).

2   "Randomised trial of endarterectomy for recently symptomatic carotid stenosis: final results of the MRC European Carotid Surgery Trial (ECST)," Lancet 351 (9113), 1379-1387 (1998).

3   H. J. Barnett, D. W. Taylor, M. Eliasziw, A. J. Fox, G. G. Ferguson, R. B. Haynes, R. N. Rankin, G. P. Clagett et al., "Benefit of carotid endarterectomy in patients with symptomatic moderate or severe stenosis. North American Symptomatic Carotid Endarterectomy Trial Collaborators," N Engl J Med 339 (20), 1415-1425 (1998).

4   A. Halliday, A. Mansfield, J. Marro, C. Peto, R. Peto, J. Potter and D. Thomas, "Prevention of disabling and fatal strokes by successful carotid endarterectomy in patients without recent neurological symptoms: randomised controlled trial," Lancet 363 (9420), 1491-1502 (2004).

5   S. M. Debrey, H. Yu, J. K. Lynch, K. O. Lovblad, V. L. Wright, S. J. Janket and A. E. Baird, "Diagnostic accuracy of magnetic resonance angiography for internal carotid artery disease: a systematic review and meta-analysis," Stroke 39 (8), 2237-2248 (2008).

6   M. J. Koelemay, P. J. Nederkoorn, J. B. Reitsma and C. B. Majoie, "Systematic review of computed tomographic angiography for assessment of carotid artery disease," Stroke 35 (10), 2306-2312 (2004).

7   I. Kane, W. N. Whiteley, P. A. Sandercock and J. M. Wardlaw, "Availability of CT and MR for assessing patients with acute stroke," Cerebrovasc Dis 25 (4), 375-377 (2008).

8   C. L. Sistrom and N. L. McKay, "Costs, charges, and revenues for hospital diagnostic imaging procedures: differences by modality and hospital characteristics," J Am Coll Radiol 2 (6), 511-519 (2005).

9   H. Scherl, J. Hornegger, M. Prummer and M. Lell, "Semi-automatic level-set based segmentation and stenosis quantification of the internal carotid artery in 3D CTA data sets," Med Image Anal 11 (1), 21-34 (2007).

10   S. Suzuki, S. Furui, T. Kaminaga and T. Yamauchi, "Measurement of vascular diameter in vitro by automated software for CT angiography: effects of inner diameter, density of contrast medium, and convolution kernel," AJR Am J Roentgenol 182 (5), 1313-1317 (2004).

11   S. Suzuki, S. Furui and T. Kaminaga, "Accuracy of automated CT angiography measurement of vascular diameter in phantoms: effect of size of display field of view, density of contrast medium, and wall thickness," AJR Am J Roentgenol 184 (6), 1940-1944 (2005).

12   H. M. Silvennoinen, S. Ikonen, L. Soinne, M. Railo and L. Valanne, "CT angiographic analysis of carotid artery stenosis: comparison of manual assessment, semiautomatic vessel analysis, and digital subtraction angiography," AJNR Am J Neuroradiol 28 (1), 97-103 (2007).

13   Z. Zhang, M. H. Berg, A. E. Ikonen, R. L. Vanninen and H. I. Manninen, "Carotid artery stenosis: reproducibility of automated 3D CT angiography analysis method," Eur Radiol 14 (4), 665-672. Epub 2003 Nov 2014. (2004).

14   T. Boskamp, D. Rinck, F. Link, B. Kummerlen, G. Stamm and P. Mildenberger, "New vessel analysis tool for morphometric quantification and visualization of vessels in CT and MR imaging data sets," Radiographics 24 (1), 287-297 (2004).

15   J. Canny, "A computational approach to edge detection," IEEE Trans. Pattern Anal. Mach. Intell. 8 (6), 679-698 (1986).

16   A. F. Frangi, W. J. Niessen, P. J. Nederkoorn, J. Bakker, W. P. Mali and M. A. Viergever, "Quantitative analysis of vascular morphology from 3D MR angiograms: In vitro and in vivo results," Magn Reson

Med 45 (2), 311-322 (2001).

17 R. Manniesing, B. K. Velthuis, M. S. van Leeuwen, I. C. van der Schaaf, P. J. van Laar and W. J. Niessen, "Level set based cerebral vasculature segmentation and diameter quantification in CT angiography," Med Image Anal 10 (2), 200-214 (2006).

18 H. Bouma, A. Vilanova, L. J. van Vliet and F. A. Gerritsen, "Correction for the dislocation of curved surfaces caused by the PSF in 2D and 3D CT images," IEEE Trans Pattern Anal Mach Intell 27 (9), 1501-1507 (2005).

19 Paulo Mendonça, Dirk Padfield, James Miller and Matt Turek, in *Computer Vision - ECCV 2004* (2004), pp. 554-565.

20 H. Bouma, J. O. Bescos, A. Vilanova and F. A. Gerritsen, in *Medical Imaging 2007: Image Processing* (SPIE, San Diego, CA, USA, 2007), Vol. 6512, pp. 65122N-65131N.

21 R. C. Chan, W. C. Karl and R. S. Lees, "A new model-based technique for enhanced small-vessel measurements in X-ray cine-angiograms," IEEE Trans Med Imaging 19 (3), 243-255 (2000).

22 H. Fujita, K. Doi, L. E. Fencil and K. G. Chua, "Image feature analysis and computer-aided diagnosis in digital radiography. 2. Computerized determination of vessel sizes in digital subtraction angiography," Med Phys 14 (4), 549-556 (1987).

23 K. R. Hoffmann, D. P. Nazareth, L. Miskolczi, A. Gopal, Z. Wang, S. Rudin and D. R. Bednarek, "Vessel size measurements in angiograms: a comparison of techniques," Med Phys 29 (7), 1622-1633 (2002).

24 S. Worz and K. Rohr, "Cramer-Rao Bounds for Estimating the Position and Width of 3D Tubular Structures and Analysis of Thin Structures with Application to Vascular Images," J. Math. Imaging Vis. 30 (2), 167-180 (2008).

25 G. J. Streekstra, S. D. Strackee, M. Maas, R. ter Wee and H. W. Venema, "Model-based cartilage thickness measurement in the submillimeter range," Med Phys 34 (9), 3562-3570 (2007).

26 S. Worz and K. Rohr, "Segmentation and quantification of human vessels using a 3-D cylindrical intensity model," IEEE Trans Image Process 16 (8), 1994-2004 (2007).

27 Stefan Wörz and Karl Rohr, in *Medical Image Computing and Computer-Assisted Intervention – MICCAI 2004* (2004), pp. 491-499.

28 G.H. Granlund, "Fourier Preprocessing for hand print character recognition," IEEE Trans. Computers C-21 (Febr), 195-201 (1972)

29 C.T. Zahn and R.Z. Roskies, "Fourier descriptors for plane close curves," IEEE Trans. Computers C-21 (March), 269-281 (1972).

30 C. de Monye, F. Cademartiri, T. T. de Weert, D. A. Siepman, D. W. Dippel and A. van Der Lugt, "Sixteen-detector row CT angiography of carotid arteries: comparison of different volumes of contrast material with and without a bolus chaser," Radiology 237 (2), 555-562 (2005).

31 C. de Monye, T. T. de Weert, W. Zaalberg, F. Cademartiri, D. A. Siepman, D. W. Dippel and A. van der Lugt, "Optimization of CT angiography of the carotid artery with a 16-MDCT scanner: craniocaudal scan direction reduces contrast material-related perivenous artifacts," AJR Am J Roentgenol 186 (6), 1737-1745 (2006).

32 N. Anzalone, F. Scomazzoni, R. Castellano, L. Strada, C. Righi, L. S. Politi, M. A. Kirchin, R. Chiesa et al., "Carotid artery stenosis: intraindividual correlations of 3D time-of-flight MR angiography, contrast-enhanced MR angiography, conventional DSA, and rotational angiography for detection and grading," Radiology 236 (1), 204-213 (2005).

33 D. E. Hyde, A. J. Fox, I. Gulka, P. Kalapos, D. H. Lee, D. M. Pelz and D. W. Holdsworth, "Internal carotid artery stenosis measurement: comparison of 3D computed rotational angiography and conventional digital subtraction angiography," Stroke 35 (12), 2776-2781 (2004).

34 W. W. Zhang, L. M. Harris and M. L. Dryjski, "Should conventional angiography be the gold standard

for carotid stenosis?," J Endovasc Ther 13 (6), 723-728 (2006).

35   S. Schaller, J. E. Wildberger, R. Raupach, M. Niethammer, K. Klingenbeck-Regn and T. Flohr, "Spatial domain filtering for fast modification of the tradeoff between image sharpness and pixel noise in computed tomography," IEEE Transactions on Medical Imaging 22 (7), 846-853 (2003).

36   K.R. Castleman, *Digital Image Processing*, 2nd International Edition ed. (Pearson Education, 1996).

37   B. Jähne, „*Digital Image Processing*", 6 ed. (Springer-Verlag, Heidelberg, 2005).

38   J. Y. Gauvrit, X. Leclerc, M. Vermandel, B. Lubicz, D. Despretz, J. P. Lejeune, J. Rousseau and J. P. Pruvo, "3D rotational angiography: use of propeller rotation for the evaluation of intracranial aneurysms," AJNR Am J Neuroradiol 26 (1), 163-165 (2005).

39   L. Antiga and D. A. Steinman, "The Vascular Modeling Toolkit", http://www.vmtk.org, 2009

40   L. Antiga, B. Ene-Iordache and A. Remuzzi, "Computational geometry for patient-specific reconstruction and meshing of blood vessels from MR and CT angiography," IEEE Trans Med Imaging 22 (5), 674-684 (2003).

41   L. Antiga, M. Piccinelli, L. Botti, B. Ene-Iordache, A. Remuzzi and D. A. Steinman, "An image-based modeling framework for patient-specific computational hemodynamics," Med Biol Eng Comput 46 (11), 1097-1112 (2008).

42   V. Caselles, R. Kimmel and G. Sapiro, "Geodesic Active Contours," International Journal on Computer Vision 22 (1), 61-97 (1997).

43   L. Antiga, B. Ene-Iordache, L. Caverni, G. P. Cornalba and A. Remuzzi, "Geometric reconstruction for computational mesh generation of arterial bifurcations from CT angiography," Comput Med Imaging Graph 26 (4), 227-235 (2002).

44   P.J. Besl and N.D. McKay, "A method for registration of 3-d shapes," IEEE Trans. Pat. Anal. and Mach. Intel. 14 (2), 239-256 (1992).

45   J. A. Nelder and R. Mead, "A Simplex Method for Function Minimization," The Computer Journal 7 (4), 308-313 (1965).

46   W.H Press, S.A. Teukolsky, W.T. Vetterling and B.P. Flannery, in *The Art of Scientific Computing* (Cambridge University, New York, 2002), pp. 292.

7

Intracranial CT angiography obtained from a cerebral CT perfusion examination

Hugo A.F. Gratama van Andel, Henk W. Venema, Charles B.L.M. Majoie,
Gerard J. Den Heeten, Cornelis A. Grimbergen, Geert J. Streekstra

ABSTRACT

CT perfusion (CTP) examinations of the brain are performed increasingly for the evaluation of cerebral blood flow in patients with stroke and vasospasm after subarachnoid hemorrhage. Of the same patient often also a CT angiography (CTA) examination is performed. This study investigates the possibility to obtain CTA images from the CTP examination, thereby possibly obviating the CTA examination. This would save the patient exposure to radiation, contrast, and time.

Each CTP frame is a CTA image with a varying amount of contrast enhancement, and with high noise. To improve the contrast-to-noise ratio (CNR) we combined all 3D images into one 3D image, after registration to correct for patient motion between time frames. Image combination consists of weighted averaging in which the weighting factor of each frame is proportional to the arterial contrast. It can be shown that the arterial CNR is maximized in this procedure. An additional advantage of the use of the time series of CTP images is that automatic differentiation between arteries and veins is possible. This feature was used to mask veins in the in the resulting 3D images to enhance visibility of arteries in maximum intensity projection (MIP) images.

With a Philips Brilliance 64 CT scanner (64 x 0.625 mm) CTP examinations of 8 patients were performed of 80 mm of brain, using the toggling table technique. The CTP examination consisted of a time-series of 15 3D images (2 x 64 x 0.625 mm; 80 kV; 150 mAs each) with an interval of 4 s. We measured the CNR in images obtained with weighted averaging, images obtained with plain averaging and images with maximal arterial enhancement. We also compared CNR and quality of our images with that of regular CTA examinations and examined the effectiveness of automatic vein masking in MIP images.

The CNR of the weighted averaged images is on the average 1.73 times the CNR of an image at maximal arterial enhancement in the CTP series, where the use of plain averaging increases the CNR only with a factor of 1.49. The quality of the weighted averaged images approaches that of CTA images although in the present study the image quality of CTA was not quited reached. The automatic masking of veins is effective and only small remnants of veins were sometimes present in the masked images.

Weighted averaging makes it possible to create CTA images from a CTP examination with a CNR considerably higher than that of images with maximal arterial enhancement. The quality of the resulting images approaches that of CTA images and offers the additional advantages to automatically differentiate between arteries and veins.

I. INTRODUCTION

CT perfusion (CTP) examinations of the brain are performed increasingly in patients with stroke and vasospasm after subarachnoid hemorrhage.[1-3] A CTP examination consists of a time-series of sequential CT scans, during and after injection of a contrast bolus in the patient. With CTP different functional parameters such as the cerebral blood volume and mean transit time can be quantitatively determined which may aid diagnosis and therapy of these patients.

Until recently the *z*-coverage of the CTP perfusion studies of the brain was limited and the slice thickness was substantial. Initially the coverage existed of a single section of 10 mm thickness.[4,5] This was extended to multiple sections by the introduction of multidector-array technology[6] and the introduction of the 'toggling-table' technique.[7,8] With the ongoing development of CT-scanner technology the coverage has further increased while the slice thickness decreased. Although this last feature was not of primary importance for CT-perfusion studies, it opens the possibility to exploit this higher resolution to obtain anatomical images from the cerebral vasculature from the same scan that is used to obtain the functional images.

In the diagnostic process both functional (CTP) and anatomical images (CTA) are often required at the same time.[9,10] Recently a study was published in which the feasibility of the approach of a combined CTP-CTA examination was demonstrated.[11] This approach saves the patient exposure to radiation, contrast, and examination time.

The present study addresses the question how an optimal set of CTA-like images can be obtained from a series of CTP images in time. Each CTP image can be seen as a CTA image with a varying amount of contrast enhancement and a relatively high noise level. Even at the time of maximal enhancement a single

image from a CTP sequence has a contrast-to-noise ratio (CNR) that is too low to be useful as a CTA image. To create images that have a higher CNR, and therefore are more useful in the diagnostic process as anatomical images, different strategies can be used. Plain averaging is a simple option, but it is unlikely to be optimal as it does not take into account the varying contrast over time. Weighted averaging may solve this problem.

In this paper we present a method that produces an anatomical image of the cerebral arteries with an optimal CNR from a CTP examination. First a rigid registration technique is used for the registration of all the scans in a CTP examination to correct for possible patient motion. Next weighted averaging is used to obtain one 3D image with optimal CNR of the arterial vessels.

The use of a CTP examination to create CTA images offers the additional possibility to differentiate between arteries and veins based on their enhancement in time. Differences in enhancement can be used to automatically mask venous structures that obscure the sight of arterial blood vessels in maximum intensity projections (MIP) or volume renderings (VR). This makes manual removal of veins, which can be very time consuming or virtually impossible when in close proximity of arteries, unnecessary.[12-14]

We compare the CNR of the images obtained with weighted averaging to the CNR in images obtained with plain averaging and in images with maximal arterial enhancement. We also compare the quality of our images with that of regular CTA examinations and show the effectiveness of automatic vein masking in MIP images.

II. METHODS

We start with a CTP examination with images acquired at n moments in time. A flow-diagram of the method to obtain CTA images from this CTP examination is shown in Fig. 1. The method can be divided into three parts:

I. Registration:
1   Scans from the CTP series, at moments 2,..,n, are registered to the first scan.

II. Averaging:

2   A weighted averaged image is constructed from the CTP series with the use of an arterial enhancement function.

III. Masking (optional):

3   A bone mask is created from the first, unenhanced, scan of the CTP series.
4   A weighted averaged image is constructed from the CTP series with the use of a venous enhancement function.
5   The bone in the venous weighted averaged image is masked and the resulting image is thresholded to obtain a set of all vascular voxels.
6   The vascular voxels are classified as veins or arteries based on their enhancement in time and a vein mask is created.
7   In the weighted averaged image bone and vein voxels are masked to obtain masked CTA images.
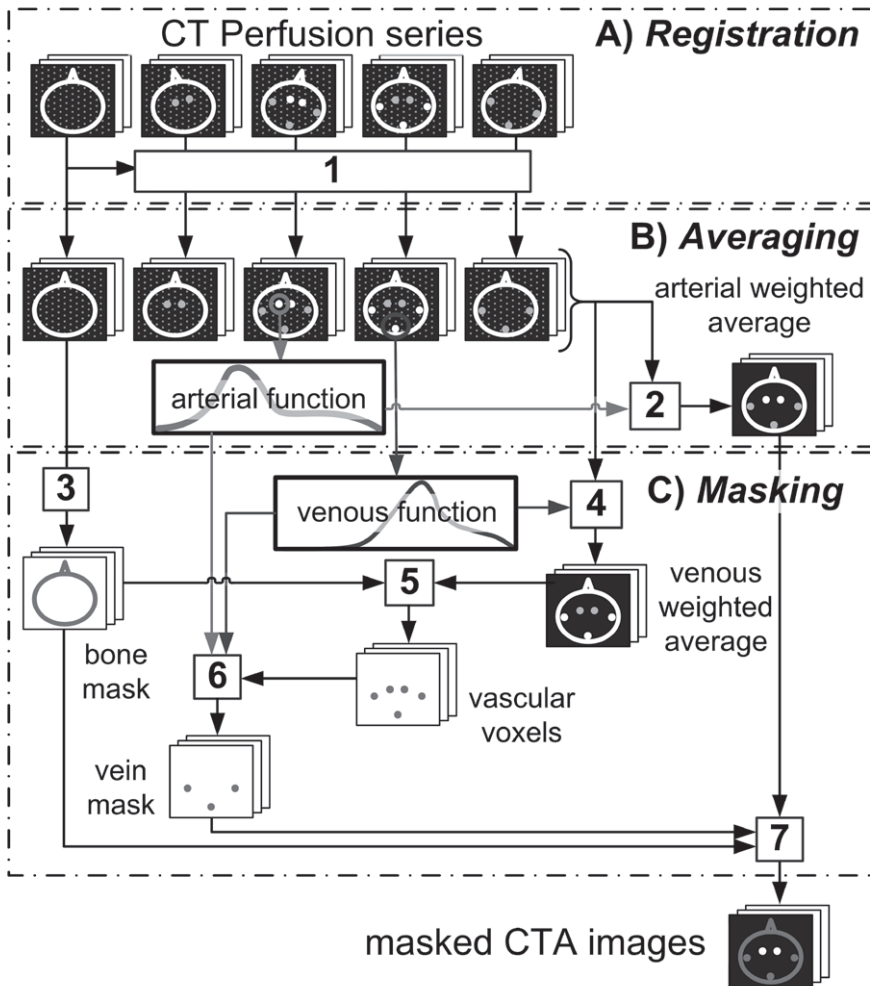
Fig. 1
A flow-diagram of the method to obtain CTA images from a CT perfusion series. The three main parts of the method are A) registration, B) weighted averaging and optionally C) masking of bone and vein structures. The numbers in the figure correspond to different processing steps and are explained in section II.

II.A. ACQUISITION

A 64 slice CT scanner was used (Brilliance 64, Philips Medical Systems, Best, The Netherlands) with a coverage in the direction of the table movement (z-direction) of 40 mm (64 x 0.625 mm). CTP examinations of the brain were performed with the toggling table technique (or 'Jog mode'),[7] which extends the

z-coverage to 2 x 40 mm. We refer to the lower volume as the caudal volume and the upper as the cranial volume. The scans normally ranged from the circle of Willis to just below the vertex of the skull. The CTP examination consisted of 2 x 15 scans with 1.8 seconds between the first and second table position and 3.8 seconds between consecutive images at the same location and a total duration of 55 seconds. The first scan was made 6 seconds after the start of the intravenous contrast bolus injection (40 ml Iodixanol; 320 mg I /ml at a rate of 4 ml/sec) followed by a 35 ml saline flush. Scans were made with 80 kV, 150 effective mAs per scan, standard resolution and 0.4 s rotation time. For CT perfusion analysis images were reconstructed with a slice thickness of 10 mm and a field of view (FOV) of 220 mm. For the purpose of this study 2 x 64 images were reconstructed with a slice thickness of 0.625 mm, a FOV of 150 mm and a matrix size of 512 x 512. Images were reconstructed with kernel *UB* (smooth with beam hardening correction[15] and scatter correction[a]).

II.B. MOTION CORRECTION AND PREPROCESSING (STEP 1)

To minimize motion artifacts, the head of the patient was placed in a holder and fixed with a hook and loop fastener. Because of the short scantime of each scan (0.4 s) motion *during* each scan was minimal. Slight motions *in between* the scans, however, are almost inevitable due to the total duration of the examination (55 s) and the toggling of the table. To correct for the motion in between the scans, we used a 3D rigid registration technique[16] to register all volumes of the subsequent scans to the volume of the first scan, using the bones of the skull as a reference. This was done separately for the cranial and caudal volume.

After registration of the data, two preprocessing steps were performed. First in each volume of 64 slices, pairs of adjacent slices were averaged to obtain a slice width of 1.25 mm and a slice increment of 0.625 mm. This was done in order to reduce the noise and to obtain overlap in the *z*-direction.

Secondly, a slight increase appeared to be present in the CT-values towards the periphery of the brain. This was probably a cupping artifact due to imperfections in the reconstruction procedure, and some spill-over of the high CT-values of the skull to the first adjacent voxels. Because this inhomogeneity negatively influenced the quality of the MIPs of the complete scan volume, it was corrected in a preprocessing step (see Sec. III.A).

II.C. WEIGHTED AVERAGING (STEP 2)

A 3D image with an optimal contrast-to-noise ratio can be obtained from the CT time series with weighted averaging, using the following procedure.

Consider a series of 3D images $I_i(\boldsymbol{x})$, $\{i=1,..,n\}$ obtained during a CTP examination at n moments in time, $I_i(\boldsymbol{x})$ representing the CT-value in scan i for all voxels $\boldsymbol{x}$. A weighted averaged image is obtained by multiplying the value of each voxel in image $I_i(\boldsymbol{x})$ with a weight factor w_i, with $\sum_{i=1}^{n} w_i = 1$, and summation of the weighted images:

$$I_{wa}(\boldsymbol{x}) = \sum_{i=1}^{n} w_i I_i(\boldsymbol{x}) \qquad (1)$$

The weight factors are determined as follows. Consider a volume-of-interest (VOI) containing an artery, (see Fig. 2a). The contrast c_i in a scan i of this VOI in an image I_i is defined as the average CT-value within the VOI minus the average CT-value of the same, unenhanced, VOI, (see Fig. 2b). The contrast of the VOI in the weighted averaged image is given by:

$$\overline{c} = \sum_{i=1}^{n} w_i c_i \qquad (2)$$
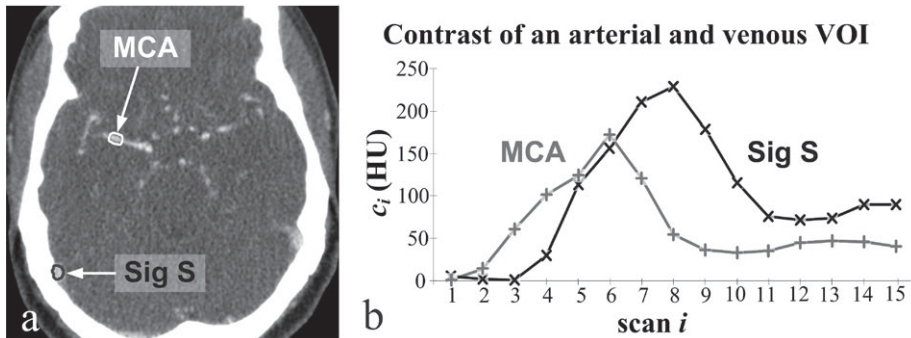
Fig. 2

Contrast in a CTP examination. (a) An axial CT image from a CT perfusion examination at the time of maximal arterial contrast enhancement with two volume of interests (VOIs) indicated, an arterial VOI in the right middle cerebral artery (MCA) and a venous VOI in the right sigmoid sinus (Sig S) (window width 600 HU, window center 200 HU). (b) The contrast c_i of the VOIs shown in (a) as a function of i.

The expected value of the standard deviation (SD) of the CT-values in a

homogeneous region within each image can be considered to be constant as all images within the time series are acquired with the same mAs value. Because the noise in the successive images can be taken to be uncorrelated, the SD in the weighted averaged image is given by:

$$SD = \sqrt{\sum_{i=1}^{n} w_i^2} \qquad (3)$$

where we have taken, without loss of generality, the SD in each image to be 1.

The optimal contrast-to-noise ratio (CNR) of the VOI can be found by maximizing:

$$CNR = \frac{\sum_{i=1}^{n} w_i c_i}{\sqrt{\sum_{i=1}^{n} w_i^2}} \qquad (4)$$

By a straightforward derivation (see appendix) it can be seen that the optimal weighting factors, w_k are:

$$w_k = \frac{c_k}{\sum_{i=1}^{n} c_i} \qquad (5)$$

For the moment we make the assumption that the enhancement in time of all arteries in the volume is the same (apart from a scale factor). We return to this point in section III.A.

The same procedure can be applied to obtain a 3D image in which the CNR of the veins is optimized. In this case the weighting factors are derived from a VOI containing one of the veins (see Fig. 2). In the present study weighted averaged images of the veins were used in the further image processing steps as detailed below (Sec. II.D.2)

II.D. MASKING

If volume rendering or maximum intensity projection is used in the visualization of CTA images, it is necessary to remove bone and vein voxels before visualization. Manual removal of veins or bone can be very time consuming or virtually

impossible when in close proximity of arteries.[12-14] Automatic removal of bone is a standard procedure.[16-21] Veins can automatically be removed by using the differences of enhancement in time between arteries and veins as described below

II.D.1 BONE MASKING (STEP 3 AND 7)

Bone masking in the arterial weighted averaged image $I_{wa}^{art}(x)$ was performed in the following way.[17] A bone-mask was made from the first, unenhanced, scan in the CTP examination by a taking all voxels with a value above a threshold τ. In this study we have taken τ to be 200 HU.[22] This mask was dilated with a kernel containing 10 voxels (8 in-plane, 2 out-of-plane) to improve its quality.[16] All voxels in the image $I_{wa}^{art}(x)$ corresponding to the voxels in the bone mask were set to an arbitrary low value.

II.D.2 VEIN MASKING (STEPS 4-7)

A vein mask was obtained as follows. First a venous enhancement function, c_i^{ven} was determined from a VOI containing a vein and the venous weighted averaged image, $I_{wa}^{ven}(x)$ was obtained. Bone in the image was masked (Fig. 3a), and the image was thresholded with a threshold ζ to find a set of vascular voxels (Fig. 3b). It appeared that $\zeta = 100$ HU gave good results. This set contains not only venous voxels but arterial voxels as well because of the large overlap in the enhancement in time of arteries and veins. For each vascular voxel the Pearson correlation coefficient r^{art} was calculated of the 15 CT-values of that voxel in time $I_i(i=1,..,15)$ and $c_i^{art} I_i(i=1,..,15)$. Likewise the correlation coefficient r^{ven} was determined, using c_i^{ven} instead of c_i^{art}, with $I_i(i=1,..,15)$ (see Fig. 3c and Fig. 3d).[23] We first tried the obvious classification rule: a voxel is considered to be venous if $r^{ven} > r^{art}$, and otherwise arterial. It appeared, however, that the classification rule: a voxel is considered to be venous if $r^{ven} > 0.86 \, r^{art}$, and otherwise arterial, gave slightly better results. This can be seen in Fig. 3e were the two clusters of arterial and venous voxels are clearly separated by this classification rule. From all voxels that were classified venous, voxels that can be attributed to noise were removed by eliminating small isolated clusters, that is, sets of connected voxels containing at most 32 voxels. Finally the venous voxels in the mask were dilated with the same

kernel as the one used for the bone mask, but in this case conditionally: voxels for which the correlation coefficient $r^{art}(x) \geq 0.8$ were not included in the vein mask. This condition was introduced to prevent erosion of arteries contiguous to veins. All voxels in the image $I_{wa}^{art}(x)$ corresponding to voxels included in the vein mask (Fig. 3f) were set to an arbitrarily low value.
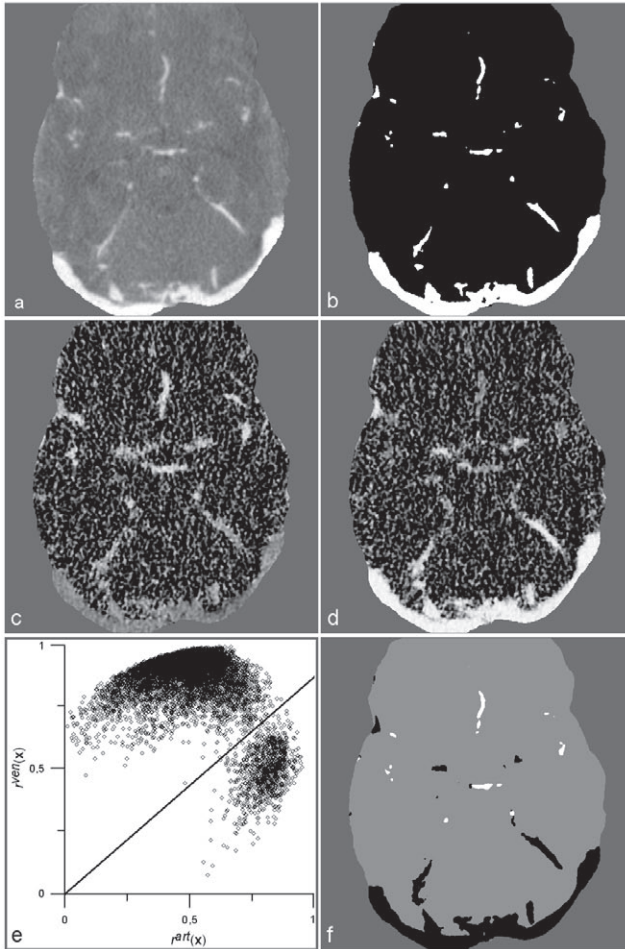
Fig. 3
Creation of the vein mask, illustrated in an axial image from a CTP examination. (a) venous weighted average image made from a CTP examination, with the bone and voxels outside the skull masked (window width 280, window level 75). (b) image (a) thresholded with $\zeta = 100$ HU, all selected voxels are white, (c) and (d) arterial and venous correlation coefficients $r^{art}(x)$ and $r^{ven}(x)$, white representing a high correlation and black a low one. For this illustration the correlation coefficients are shown for all voxels; in the calculation of the vein mask only the voxels shown in (b) are used. (e) scatter plot of the arterial and venous correlation coefficients for the voxels shown in (b). (f) final venous mask (black voxels) with arterial voxels colored white. In this final mask, the venous voxels were conditionally dilated (see sec II.D.2)

III. EXPERIMENTS

III.A. PREPROCESSING

A scan was made of the head of a Rando phantom (Alderson Research Laboratories, Stanford, CA, USA), which consists of a human skull filled with a soft tissue equivalent rubber. Acquisition and reconstruction parameters were those of the CTP examination (sec II.A) In an image acquired 3 cm above the petrous segment of the temporal bone in the phantom, the CT-value of the rubber was determined as a function of the distance to the nearest voxel of the skull. A curve was fitted to these values, up to a distance of 100 voxels from the skull, which consisted of the sum of two exponentials. In the preprocessing of the images of the patients, the CT-values of all voxels within the skull were corrected using this empirical correction function.

III.B. PATIENTS

Our method was applied to CTP examinations of eight patients. All patients were clinically suspected of a cerebral perfusion deficiency. Five patients were previously treated for a subarachnoid hemorrhage with either surgical clipping or endovascular coiling of an aneurysm. The other three patients were previously diagnosed with respectively, an arterio-venous malformation, a dissection of the basilar artery and an atypical meningioma.

To demonstrate the importance for registration of the series of scans in the CTP examination, the amount of misalignment (before registration) was quantified by determining the translation in three directions applied to the center of 14 scan volumes relative to the center in the first one in the registration procedure. Average and maximal values were taken over 14 registrations of two volumes for eight patients.

For each patient the contrast c_i^{art} and c_i^{ven}, $i=1,..,n$ were measured in a VOI in standard arteries and veins. For the caudal volume the left middle cerebral artery (L MCA) was chosen and for the cranial volume the pericallosal artery (PA) (as proximal as possible). In the caudal volume the confluence of sinuses (CfS) was chosen as standard vein and for the cranial volume the superior sagittal sinus (SSS) (as distal as possible on the dorsal side). If for some reason the standard vessel was

not present in the volume, the vessel on the right side or a vessel nearby was chosen. The VOIs consisted of all voxels with a CT value of at least 140 HU in one of the perfusion scans within a distance of 2.5 mm of the voxel in the center of the vessel.

Of some of these patients also regular CTA examinations were performed in the spiral mode, with a rotation time of 0.75 s, high resolution, pitch of 0.765, 80 kV and 600 effective mAs or 120 kV and 265 effective mAs and an injection of 80 ml contrast agent (Visipaque 320 mg I/ml) at a rate of 4 ml/s. Images were reconstructed with a FOV of 150 mm, a slice width of 0.9 mm, a slice increment of 0.45 and reconstruction kernel UB. For automatic bone removal an additional unenhanced scan was made with 150 effective mAs and the other settings the same as for the CTA scan.

The effective dose of both the CTP and the CTA examination was estimated using the CT-Expo Spreadsheet.[24] In order to make a fair comparison, the scan range for the CTA examinations was taken to be the same as for the CTP examination, i.e. 8 cm, in the lower part of the brain. The actual scan range for the CTA examinations was in the order of 12 cm or more, depending on the indication of the scan.

III.C. WEIGHT FACTORS.

In the standard procedure the weight factors for the arterial weighted image were derived from the VOI in the standard artery. Only in case all arteries in the volume have the same enhancement in time, these weight factors will be optimal for the complete volume. To investigate whether this was indeed the case, 12 additional arterial VOIs were placed in the caudal volume and two in the cranial volume (see Table III) in the CTP scans of the eight patients, provided the vessels were present.

In all VOIs the contrast $\overline{c}$ was measured after application of weighted averaging and the CNR was determined using *Eq. 4*. For the calculation of the CNR the SD was determined according to *Eq. 3*. Whether the real SD deviated from the calculated SD was studied separately (Sec. III.D) The CNR of all VOIs was also determined in the images with maximal arterial enhancement and the ratio of the CNR after weighted averaging and the CNR of the maximal arterial contrast images was calculated. For comparison the ratio was also determined using the CNR in the images obtained with plain averaging, thus with all weight factors equal in *Eq. 4*.

For purposes of comparison the CNR was also determined for venous weighting, using six venous VOIs in the caudal volume and four in the cranial volume.

III.D. NOISE MEASUREMENTS

To investigate if the noise reduction after application of weighted averaging can be described by *Eq. 3*, scans were made of the head of a Rando phantom with the acquisition and reconstruction parameters of a CTP examination (Sec. II.A) The standard deviation of the CT values within a circular region of interest (ROI) with a diameter of 38 mm placed in one slice in a homogeneous area, were measured in a single scan and after plain averaging of 2, ..,n scans (in all possible permutations of n taken from 15 scans). The SD in the ROI was also measured in 100 weighted averaged images and the average SD was determined. These images were obtained with the use of the weight factors derived from the standard artery of the caudal volume of the first patient (see Sec. III.C) and random permutations of the 15 scans made of the phantom.

III.E. CNR VALUES OF CTP AND CTA IMAGES

Although not all scan parameters for the CTP and CTA protocol were identical, we performed a comparison of the CNR in images from a weighted averaged CTP examination and images from a CTA examination. Three patients had a CTP examination that was followed by a CTA examination on the same CT scanner within a few minutes. In one of these patients the CTA was made with 80 kV, in the other two with 120 kV.

Both for the weighted averaged and CTA-images the mean CT-value was determined within small circular ROIs (diameter 1.5 mm) at the same location in three relatively large arteries (diameter approximately 4 mm). The contrast was calculated as the difference of this mean CT value and the mean CT value in a ROI in a nonenhanced scan at the same location. This last ROI was chosen slightly larger (diameter 3 mm) to reduce the influence of noise. The mean contrast value of the three ROIs was used in the CNR calculations.

For the weighted averaged images the SD values were determined as in section III.C nd section III.D The SD values for the CTA examinations were determined

by making two additional spiral CT scans of the head of the Rando phantom, with scan parameters as given in section III.B and by measuring the SD in these scans in the same manner as described in the section III.D.

IV. RESULTS

IV.A. PREPROCESSING

Fig. 4 shows the CT-values of the voxels inside the skull in the cross-section image of the head of the Rando phantom as a function of the distance to the skull. These CT-values can be adequately described by the following function:

$$f(x) = 29.6e^{-0.029x} + 120.6e^{-0.80x} + 8.0 \qquad (6)$$

All images were preprocessed by subtracting $f(x) - 8.0$ from the CT value of the voxels of the image, with x the distance in voxels to the nearest voxel of the skull in the same image.
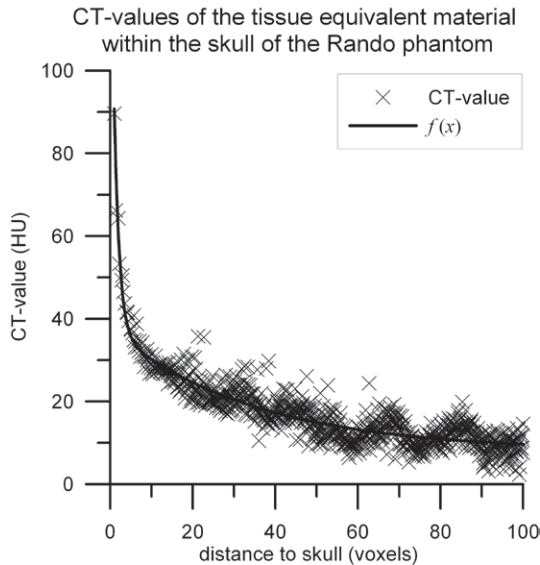

Fig. 4
CT-values of tissue equivalent material within the skull of the Rando phantom as a function of the distance to the skull. CT-values are indicated with a x, the experimental correction function $f(x)$ with a continuous line.

IV.B. PATIENT EXAMPLES

IV.B.1 REGISTRATION

Table I shows the average and maximal translation of the center of the scan volumes relative to center in the first scan volume in the registration of the patient data. The translation is the largest in the z-direction, which is probably due to the use of the toggling table technique, and the smallest in the y-direction, which reflects the stabilizing influence of the table top on the movement of the head.

Table I
Translation in three directions applied to the center of 14 scan volumes relative to the center in the first scan volume in the registration procedure. Average and maximal values were taken over 14 registrations of two volumes for eight patients.

	Translation (mm)		
Direction	x	y	z
Average	0.22	0.08	0.41
Maximum	1.08	0.55	2.04

With the x-axis horizontally and the y-axis vertically in the cross-sectional plane, and the z-axis in the direction of table movement.

IV.B.2 IMAGES

Fig. 5 shows a ROI of 75 x 75 mm in axial images of the CTP examination of patient 7. Fig. 5a shows the weighted averaged and Fig. 5b the plain average, Fig. 5c the image of the CTP series with maximal arterial enhancement. For comparison the registered CTA is shown in Fig. 5d. Different window widths and window levels were chosen in order to make the average gray level of arteries and average gray level of brain tissue approximately the same in all the images. Because of the differences in window width and window level, the contrast in the background is enhanced in the weighted averaged image (Fig. 5a), and especially in the plain averaged image (Fig. 5b).

Fig. 6 shows MIP-images on the sagittal plane of a central VOI (of 94 x 94 x 40 mm) of the same patient as in Fig. 5. Fig. 6a shows the weighted average, Fig. 6b

the same image with vein masking and Fig. 6c the plain average. For comparison a MIP image of the same VOI in the registered CTA is shown in Fig. 6d. In both Fig. 5 and Fig. 6 the difference in image quality between the weighted averaged image and image of maximal arterial enhancement is evident. The image quality of the weighted averaged images is somewhat less than that of the CTA image, however. The masking of the veins Fig. 6b aids in the visibility of some of the smaller arteries that are less visible in Fig. 6a. For MIP-images from multiple directions see the EPAPS supplemental movie.[25]

Fig. 7 shows MIP-images on the coronal plane of the complete reconstructed volume from the weighted averaged CTP examination of patient 1. Fig. 7a shows the weighted average, Fig. 7b the weighted average with vein masking. In the latter case the masking of the veins makes arteries in the MIP visible that otherwise would be obscured due to overprojection. The calcifications visible in Fig. 7a are absent in Fig. 7b due to the proximity of a vein that was masked (see Sec. II.D.2). In both Fig. 7a and Fig. 7b some artifacts due to the presence of platinum coils are present in the lower part of the MIP. The MIP-images are also shown in the blinking mode[26] and from multiple directions in the EPAPS supplemental movie.[25]
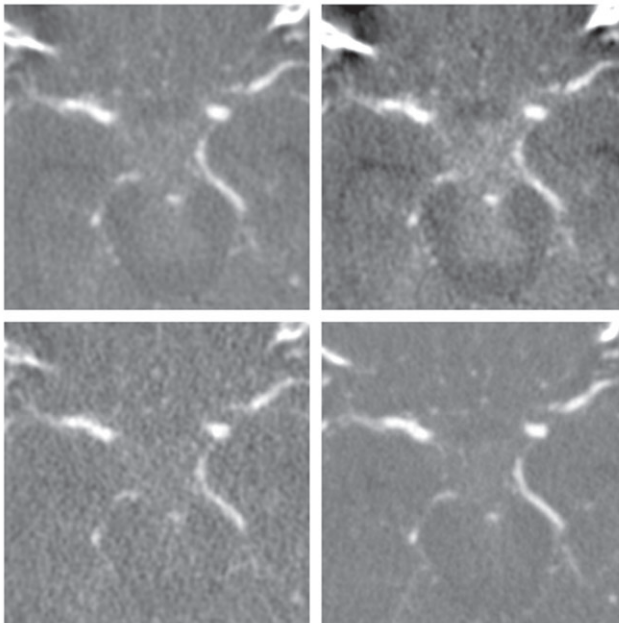
Fig. 5
Images of a region of interest (75 x 75 mm) containing the circle of Willis in an axial slice (slice width 1.25 mm) of a CTP examination; (a) weighted averaged, (b) plain averaged and (c) image with maximal arterial enhancement. (d) axial image (slice width 0.9 mm) from a registered CTA examination. In (c) window width is 600 HU and window level 75 HU, the window width and level in the other three images were chosen to obtain approximately the same gray values for the arteries and background of brain tissue as in figure (c).
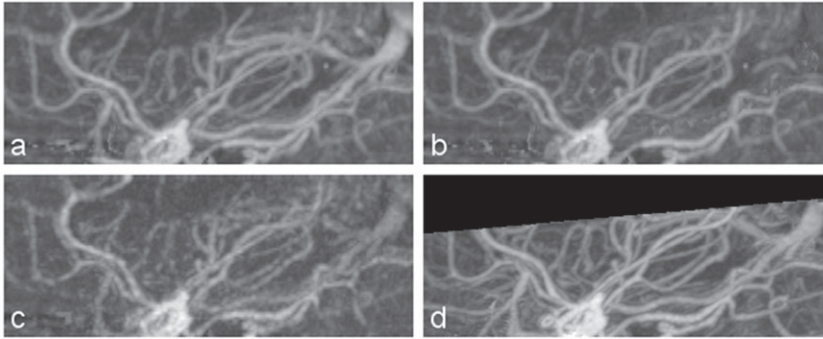
Fig.6

Maximum intensity projection (MIP) on the sagittal plane of a volume of interest (VOI) of 94 x 94 x 40 mm of a CTP examination. (a) weighted averaged, (b) weighted averaged with vein masking and (c) image with maximal arterial enhancement. For comparison (d) shows the MIP image of the same VOI in the registered CTA. In (c) window width is 500 HU and window level 230 HU, the window width and level in the other three images were chosen to obtain approximately the same gray values for the arteries and background of brain tissue as in figure (c).
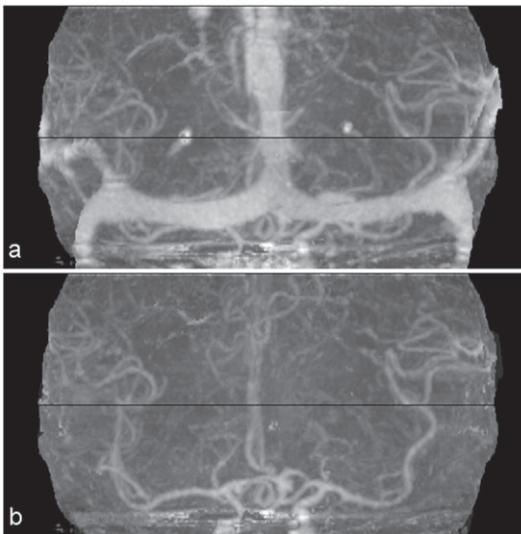
Fig. 7

Maximum intensity projections on the coronal plane of the complete scan volume (150 x 150 x 80 mm) of a weighted averaged CTP examination. (a) without vein masking, (b) with vein masking. Window width 300 and window center 130. In the lower part of the MIPs some artifacts due to the presence of platinum coils are present.

IV.B.3 EFFECTIVE DOSE

The estimated effective doses for a CTP and a CTA examination, both with a scan range of 8 cm, are listed in Table II. We note that for this relatively short scan trajectory the CTA-scan is relatively dose-inefficient, due to the large contribution of spilled dose in the beginning and end of the scan,[27] which amounts to 31% of the total effective dose.

Table II
Estimated effective doses for CTP and CTA examinations with a scan range of 8 cm.

	tube voltage (kV)	effective tube charge (mAs)	effective dose (mSv)
CTP	80	2250	2.3
CTA	80	600	0.8
CTA	120	265	1.0

IV.C. WEIGHT FACTORS

In Table III the CNR of different arteries of patient 1 is given in weighted averaged and plain averaged images, relative to the CNR of the image with maximal arterial enhancement. In this patient weighted averaging using the standard weight factors gives an average increase in CNR of a factor 1.81 compared with the image with maximal enhancement. The choice of the set of arterial weight factors does not influence the relative CNR much: when the weight factors derived from the individual arteries where used, it increased on the average to 1.82. Plain averaging gives an average increase of a factor 1.49 over the CNR in the image with maximal enhancement.

For the other patients, the increase in CNR was somewhat less: on the average for weighted averaging with the use of weight factors derived from the standard artery or the individual arteries 1.73 and 1.75, respectively, and for plain averaging 1.37 (see Table IV).

In optimal venous weighted averaged images the average CNR relative to CNR in the images with maximal venous enhancement was 1.81 (SD 0.12, $n = 77$ venous VOIs) with the weight factors derived from the standard vein. With the weight factors derived from the vein itself the average CNR was 1.84 (SD 0.12) and with plain averaging the average CNR was 1.46 (SD 0.14). The gain in CNR when venous weighting is applied is thus somewhat higher than with arterial weighting, due to the broader peak of the venous enhancement curve (see Fig. 2).

Table III
The CNR, relative to CNR in the image with maximal enhancement, for 16 arteries in patient 1. Weighted averaging with standard weight factors, weight factors from the artery itself and plain averaging.

| Caudal Volume | Artery* | weighted averaging | | plain averaging |
		weight factors from standard artery	weight factors from artery itself	all weight factors equal
	L ICA	1.82	1.82	1.50
	R ICA	1.87	1.88	1.56
	BA	1.91	1.93	1.58
	L PCA	1.87	1.89	1.59
	R PCA	1.82	1.84	1.54
	L MCA M1**	1.79	1.79	1.45
	R MCA M1	1.69	1.70	1.33
	L MCA M2	1.72	1.72	1.38
	R MCA M2	1.80	1.81	1.45
	L MCA M3 sup.	1.62	1.63	1.29
	R MCA M3 sup.	1.96	1.97	1.72
	L MCA M3 inf.	1.63	1.64	1.29
	R MCA M3 inf.	1.95	1.96	1.65
Cranial Volume				
	PA prox.**	1.76	1.76	1.38
	PA ½	1.84	1.86	1.57
	PA dist.	1.91	1.93	1.58
average (SD)		1.81 (0.10)	1.82 (0.11)	1.49 (0.13)

CNR: contrast-to-noise ratio; SD: standard deviation; L: left; R: right; ICA: internal carotid artery; BA: basilar artery; PCA: posterior cerebral artery; MCA: middle cerebral artery; M1-M3: the numbered anatomical segment28; PA: pericallosal artery; sup.: superior; inf.: inferior; prox.: proximal; dist.: distal.
* arteries are ordered from more proximal, to more distal to the heart.
** standard artery.

Table IV
The average contrast-to-noise-ratio (CNR) relative to CNR in the images with maximal arterial enhancement, for 8 patients, with the standard deviation (SD) between parentheses.

| Patient | # arteries | weighted averaging | | plain averaging |
		weight factors from standard artery	weight factors from artery itself	all weight factors equal
1	16	1.81 (0.10)	1.82 (0.11)	1.49 (0.13)
2	16	1.70 (0.11)	1.72 (0.10)	1.37 (0.12)
3	16	1.68 (0.08)	1.69 (0.08)	1.33 (0.08)
4	6	1.80 (0.09)	1.81 (0.10)	1.57 (0.13)
5	16	1.63 (0.13)	1.69 (0.09)	1.36 (0.09)
6	11	1.76 (0.12)	1.77 (0.13)	1.41 (0.12)
7	16	1.79 (0.04)	1.80 (0.05)	1.35 (0.08)
8	13	1.69 (0.08)	1.73 (0.07)	1.26 (0.07)
average (SD)	110	1.73 (0.11)	1.75 (0.10)	1.37 (0.12)

IV.D. NOISE MEASUREMENTS

In Fig. 8 the SD of a ROI in a homogenous area in the Rando phantom is depicted as a function of the number of images that is averaged. It appears that the noise decreases slightly less with the number that is averaged than theory predicts for uncorrelated data, because of slight residual inhomogeneities and artifacts in the images (see Fig. 9). For the weighted averaged images of the phantom that were acquired with the weight factors derived from the standard VOI in patient one, the SD was 6.4 % higher than the theoretical value.
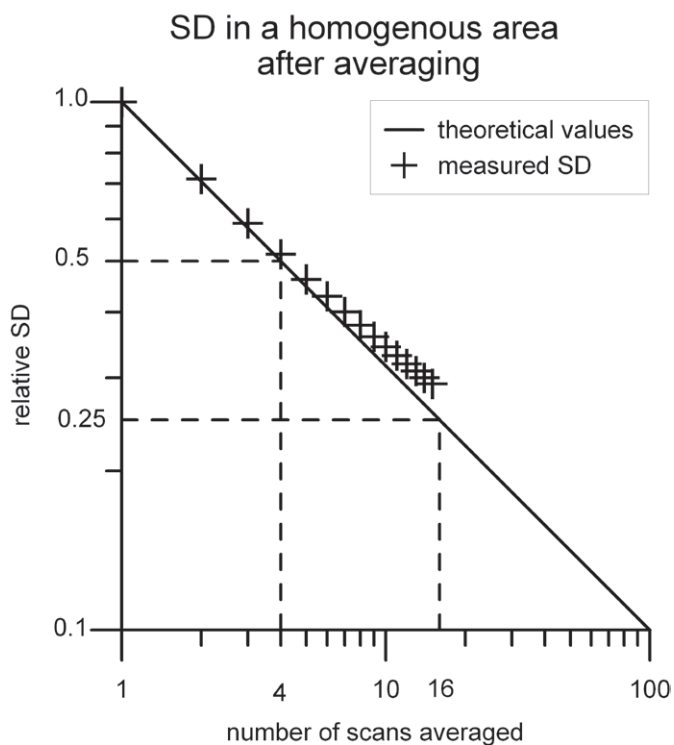
Fig. 8
The standard deviation (SD) of the CT values in a circular ROI (diameter 38 mm) in a homogenous area in the Rando phantom as a function of number of images that is averaged. The theoretical values are indicated with the continuous line and the measured values with a + symbol.
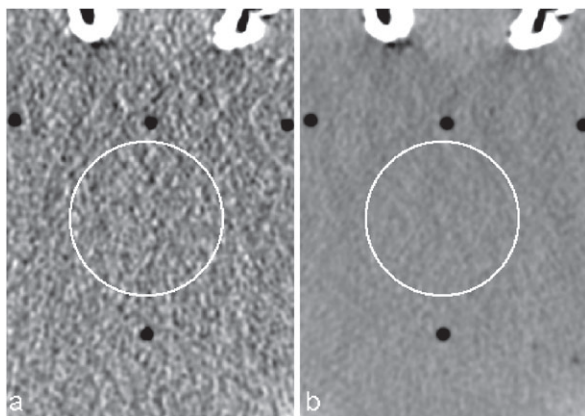
Fig. 9
The region of interest (diameter 38 mm) in the head of the rando phantom in which the standard deviation was measured. (a) one of the scans from the CTP series (b) the average of the 15 scans in the CTP series. Window width 200 and window center 0 HU.

IV.E. CNR VALUES IN CTP AND CTA IMAGES

In Table V CNR values are given for CTP examinations with and without weighted averaging and for CTA examinations of three patients. For the patient for which the CTA examination was performed at 80 kV (pat. 7), the CNR of the weighted CTP examination is slightly less than for the CTA examination. For the two patients for which the CTA examination was performed at 120 kV (pat. 1 and 3) the CNR of the CTP examination is nearly the same or slightly higher. However, in the interpretation of the CNR values the differences in the scan protocols for CTP and CTA examinations have to be taken into account. We return to this point in the discussion.

Table V
The average contrast of regions of interest in three arteries, the standard deviation of the noise and the CNR values in the images obtained with weighted averaging of a CTP examination, the images in the CTP series at maximal enhancement and in the images of a CTA examination for three patients.

	Patient [tube voltage of CTA]	1 [120 kV]	3 [120 kV]	7 [80 kV]
	CTP with weighted averaging	172	193	222
Contrast [HU]	CTP at maximal enhancement	297	338	372
	CTA	209	271	440
	CTP with weighted averaging	7.2	7.6	7.9
SD [HU]	CTP at maximal enhancement	22.5	22.5	22.5
	CTA	10.7	10.7	14.4
	CTP with weighted averaging	24.0	25.2	28.1
CNR	CTP at maximal enhancement	13.2	15.1	16.6
	CTA	19.6	25.4	30.7

CTP: CT perfusion; CTA: CT angiography; SD: standard deviation; CNR: contrast-to-noise ratio.

V. DISCUSSION

In a diagnostic work-up often a CTA examination and CT perfusion study of the brain of a patient are made within a few minutes. Both examinations require the injection of iodine contrast, and both are accompanied with radiation exposure. The present study shows that in principle it is possible to combine the information contained in a CT perfusion study to obtain CTA-images of sufficient quality, although in the present study the image quality of a CTA examination was not quite reached. Elimination of the CTA examination has several advantages. In the first place patient dose will be reduced, although the gain in this respect is limited (in the order of 30 %) due to the relative high effective dose of a CTP examination. Moreover the contrast saving for the patient will be substantial (only 40 ml instead of 120 ml iodine contrast), and the duration of the examination of the patient will be shortened considerably. Another advantage of the use of CTP-derived images over a CTA examination is the possibility to differentiate between arteries and veins which, as the present study shows, can be used to automatically mask venous structures that may obstruct the view of the arteries.

A straightforward approach to obtain CTA images of a CT perfusion examination is to use the images at the time of maximal arterial enhancement.[11] We have shown that with the weighted average approach used in the present study the contrast-to-noise ratio can be considerably improved: the CNR of the averaged images is on the average 1.73 times the CNR of one image at maximal enhancement, equivalent with CNR obtained by the averaging of $1.73^2 = 3$ images of maximal contrast. The consequences for the image quality of this gain in CNR are illustrated in Fig. 5 and Fig. 6.

The CNR-values quoted above were determined using the expected reduction of noise as a function of the number of images that is averaged. In practice it appeared that the noise reduction was slightly less, however. This is due to residual inhomogeneities in the field of view, which are not reduced by the averaging process (see Fig. 9). These inhomogeneities will influence the measured SD, but this will be the case with noise reduction anyhow, irrespectively whether it is pursued with averaging of images, or with an increase of the mAs of a single image.

It appeared that the gain in CNR is hardly influenced by the choice of the arterial enhancement function used in the averaging process. Because the images

of the CTP study were obtained with 150 mAs (at 80 kV), averaging of 3 images means that the CNR of the weighted averaged image is the same as that of a single image made with 450 mAs. This tube charge approaches the tube charge of the CTA-study (600 mAs at 80 kV).

Still the image quality of the weighted averaged images appeared to be somewhat less than that of CTA images. In the one patient for which images could be compared that were made at the same tube voltage (80 kV), the sharpness appeared was somewhat less both in-plane and in the z-direction (Fig. 5 and Fig. 6). The in-plane sharpness of CTP images is slightly lower because these images were made with standard resolution, while for the CTA images the high resolution mode was used. In the z-direction the sharpness is affected by the slightly greater slice thickness in the weighted averaged CTP images (1.25 mm) as compared to the CTA images (0.9 mm).

For this patient the CNR value of the weighted averaged CTP images is only slightly lower than the CNR value of the CTA images. However, when interpreting the relative CNR values one has to take into account the above mentioned differences in resolution. Both the use of the high resolution mode and the use of a smaller slice thickness will increase the noise in the images, and thus for the same resolution the CNR-values of the CTA images would have been higher. Important reasons for this difference in CNR are the higher enhancement of the arteries in the CTA-study (see Table V), due to the larger amount of contrast that is injected,[29] and the above mentioned difference in effective tube charge.

For the two other patients in which the CNR-values were determined the CNR values of the weighted CTP-images were nearly the same or even higher than those of the CTA images. This comparison is not completely fair, however, as in these patients the CTA-study was performed at 120 kV, and it is known that for the same dose (which is approximately the case here, see Table II) the CNR in CTA-examinations of the brain at 120 kV is lower than at 80 kV.[30,31]

Apart from these differences in CNR in weighted averaged and CTA images, other differences remain. The most important one is the use of sequential mode for the CTP-images and spiral mode for the CTA-images. For the same dose the image quality of spiral CT will be somewhat better than that of sequential CT.[32] Moreover, for cone-beam CT with a circular x-ray source trajectory, such as used in the present study, artifacts may be present that also may negatively influence the

image quality.[33] Another difference is that, because of the averaging process, the contrast of the different tissues in the brain is enhanced relative to the contrast of a single image (see Fig. 5).

A final point on the image quality concerns the averaging process that was used to obtain the images in the present study. An important point is that the images are registered before averaging; the in-plane shift in the images was - on the average - in the order of 0.1 to 0.2 mm, and out-of-plane in the order of 0.4 mm, with incidentally higher values (see Table I). Although the registration process is of course not perfect, we expect that the errors in the registration will be substantially less than the above-mentioned values, and that the image sharpness will not be significantly affected by this phenomenon.

Although we demonstrated the feasibility of the approach, some practical limitations remain. One problem in the present study was the limited coverage in the z-direction of the CTP-study, and consequently, of the CTA-images obtained from this study. With the scanner available in this study a coverage of 80 mm was available. In a CTA-scan of the brain often 120 mm or more is covered in the z-direction. With the increasing coverage of new scanners, such as implemented in the Toshiba Aquilion One, with a coverage of 160 mm, this limitation has disappeared.

Another limitation concerns the sample rate. In the present study only one image in 3.5 s was available, and a higher sampling rate is desirable, especially in the arterial phase, to improve the image quality. A much higher sampling rate (0.4 s) could have been obtained by not using the 'toggling table' technique, but that would have reduced the coverage to 40 mm. This limitation will also disappear with the use of scanners with a larger coverage.

An additional advantage of the present approach of obtaining CTA images from a CTP series is the possibility to use the differences in the enhancement in time of arteries and veins to differentiate between these two. In the present study this differentiation was used to construct a venous mask, with which the veins in the images could be obliterated or not. Especially instructive was to use both vein masked images and unmasked images in the blinking mode.[26] Although the quality of the separation of arteries and veins was high, sometimes small remnants of veins were still present in the masked images, and these remnants could be easily identified in the blinked images. Other methods have been developed to

differentiate the arteries from veins in CTA images.[34] As these methods use region-growing techniques, these methods have problems with distinguishing veins and arteries in the central part of the brain where they are close to each other.

One of the reasons that the separation of arteries and veins was not yet perfect, is that there appears to be somewhat more differentiation in the enhancement in time in the veins than in the arteries. This is probably also the reason that the optimal differentiation between arteries and veins was not obtained by separating those two by the line of identical correlation, but a line slightly lower (Fig. 3e). This problem can be solved by estimating the venous enhancement function locally and possibly also as a function of vein size. In one patient we noticed two veins on the left side of the head that were enhanced considerably earlier than the other veins. In this patient the veins originated from an arterio-venous malformation. This is a point for further study as it possibly could be used diagnostically.

The arterial enhancement in time appeared to be relatively constant, as judged from the small changes of the CNR obtained with different arteries. For larger volumes, such as can be obtained with the Toshiba Aquilion One scanner, it is possible that for optimal results of the weighted averaging the arterial enhancement functions also have to be estimated locally.

We finally note that in the present study only arterial images were shown. The above procedure can also be applied if one is interested in the veins instead of the arteries as in CT venography (CTV).[35] The same procedure can be applied using a venous enhancement function, and the arteries can be masked if desired. The gain in CNR when this method is applied for venography is is even slightly higher than in the present application (sect. IV.C).

In conclusion, weighted averaging makes it possible to create CTA images from a CTP examination with a contrast-to-noise ratio considerably higher than that of images with maximal arterial enhancement. The use of weighted averaging on CTP images result in images with a quality that approaches the quality of CTA images and offers the additional advantages to automatically differentiate between arteries and veins.

APPENDIX:

DERIVATION OF OPTIMAL WEIGHTING FACTORS

Given a volume of interest (VOI) in a series of images with contrast c_i, $i=1,..,n$ and $c_1=0$. The weight factors w_i in the weighted averaging procedure have to be chosen to maximize the following function:

$$CNR = \frac{\sum_{i=1}^{n} w_i c_i}{\sqrt{\sum_{i=1}^{n} w_i^2}} \tag{A1}$$

The maximization of the CNR requires that for all $k=1,..,n$, the partial derivative of the CNR^2 with respect to w_k is zero, i.e.:

$$\frac{\partial CNR^2}{\partial w_k} = \frac{\left(\sum_{i=1}^{n} w_i^2\right) 2 \left(\sum_{i=1}^{n} w_i c_i\right) c_k - \left(\sum_{i=1}^{n} w_i c_i\right)^2 2 w_k}{\left(\sum_{i=1}^{n} w_i^2\right)^2} = 0 \tag{A2}$$

From *eq. A2* follows that the partial derivative is zero if:

$$c_k \sum_{i=1}^{n} w_i^2 = w_k \sum_{i=1}^{n} w_i c_i \tag{A3}$$

The weighting factor w_k for an arbitrary image k that will give the optimal CNR of the averaged image is:

$$w_k = \frac{\sum_{i=1}^{n} w_i^2}{\sum_{i\,1}^{n} w_i c_i} \, c_k \tag{A4}$$

Since the term

$$\frac{\sum_{i=1}^{n} w_i^2}{\sum_{i=1}^{n} w_i c_i} \tag{A5}$$

is equal for all k, it follows that $w_k \sim c_k$. By choosing $\sum_{i=1}^{n} w_i = 1$ the optimal weighting factors, w_k are:

$$w_k = \frac{c_k}{\sum_{i=1}^{n} c_i} \tag{A6}$$

REFERENCES

1   R. Scaroni, N. Tambasco, G. Cardaioli, L. Parnetti, F. Paloni, B. Boranga and G. P. Pelliccioli, "Multi-modal use of computed tomography in early acute stroke, part 2," Clin Exp Hypertens 28 (3-4), 427-431 (2006).

2   M. Wintermark, "Brain perfusion-CT in acute stroke patients," European radiology 15 Suppl 4, D28-31 (2005).

3   M. Wintermark, N. U. Ko, W. S. Smith, S. Liu, R. T. Higashida and W. P. Dillon, "Vasospasm after sub-arachnoid hemorrhage: utility of perfusion CT and CT angiography on diagnosis and management," Ajnr 27 (1), 26-34 (2006).

4   M. Koenig, M. Kraus, C. Theek, E. Klotz, W. Gehlen and L. Heuser, "Quantitative assessment of the ischemic brain by means of perfusion-related parameters derived from perfusion CT," Stroke 32 (2), 431-437 (2001).

5   M. Wintermark, J. P. Thiran, P. Maeder, P. Schnyder and R. Meuli, "Simultaneous measurement of regional cerebral blood flow by perfusion CT and stable xenon CT: a validation study," Ajnr 22 (5), 905-914 (2001).

6   M. Wintermark, M. Reichhart, O. Cuisenaire, P. Maeder, J. P. Thiran, P. Schnyder, J. Bogousslavsky and R. Meuli, "Comparison of admission perfusion computed tomography and qualitative diffusion- and perfusion-weighted magnetic resonance imaging in acute stroke patients," Stroke 33 (8), 2025-2031 (2002).

7   H. C. Roberts, T. P. Roberts, W. S. Smith, T. J. Lee, N. J. Fischbein and W. P. Dillon, "Multisection dynam-ic CT perfusion for acute cerebral ischemia: the "toggling-table" technique," Ajnr 22 (6), 1077-1080 (2001).

8   S. W. Youn, J. H. Kim, Y. C. Weon, S. H. Kim, M. K. Han and H. J. Bae, "Perfusion CT of the brain using 40-mm-wide detector and toggling table technique for initial imaging of acute stroke," Ajr 191 (3), W120-126 (2008).

9   M. Wintermark, R. Meuli, P. Browaeys, M. Reichhart, J. Bogousslavsky, P. Schnyder and P. Michel, "Comparison of CT perfusion and angiography and MRI in selecting stroke patients for acute treat-ment," Neurology 68 (9), 694-697 (2007).

10 W. S. Smith, H. C. Roberts, N. A. Chuang, K. C. Ong, T. J. Lee, S. C. Johnston and W. P. Dillon, "Safety and feasibility of a CT protocol for acute stroke: combined CT, CT angiography, and CT perfusion imaging in 53 consecutive patients," Ajnr 24 (4), 688-690 (2003).

11 C. Y. Yang, Y. F. Chen, C. W. Lee, A. Huang, Y. Shen, C. Wei and H. M. Liu, "Multiphase CT Angiography versus Single-Phase CT Angiography: Comparison of Image Quality and Radiation Dose," Ajnr 29, 1288-1295 (2008).

12 S. Napel, M. P. Marks, G. D. Rubin, M. D. Dake, C. H. McDonnell, S. M. Song, D. R. Enzmann and R. B. Jeffrey, Jr., "CT angiography with spiral CT and maximum intensity projection," Radiology 185 (2), 607-610 (1992).

13 R. B. Schwartz, K. M. Jones, D. M. Chernoff, S. K. Mukherji, R. Khorasani, H. M. Tice, R. Kikinis, S. M. Hooton et al., "Common carotid artery bifurcation: evaluation with spiral CT. Work in progress," Radiology 185 (2), 513-519 (1992).

14 R. B. Schwartz, H. M. Tice, S. M. Hooten, L. Hsu and P. E. Stieg, "Evaluation of cerebral aneurysms with helical CT: correlation with conventional angiography and MR angiography," Radiology 192 (3), 717-722 (1994).

15   P. M. Joseph and R. D. Spital, "A method for correcting bone induced artifacts in computed tomography scanners," Journal of computer assisted tomography 2 (1), 100-108 (1978).

16   M. van Straten, H. W. Venema, G. J. Streekstra, C. B. Majoie, G. J. den Heeten and C. A. Grimbergen, "Removal of bone in CT angiography of the cervical arteries by piecewise matched mask bone elimination," Medical Physics 31 (10), 2924-2933 (2004).

17   H. W. Venema, F. J. Hulsmans and G. J. den Heeten, "CT angiography of the circle of Willis and intracranial internal carotid arteries: maximum intensity projection with matched mask bone elimination-feasibility study," Radiology 218 (3), 893-898 (2001).

18   M. Lell, K. Anders, E. Klotz, H. Ditt, W. Bautz and B. F. Tomandl, "Clinical evaluation of bone-subtraction CT angiography (BSCTA) in head and neck imaging," European radiology 16 (4), 889-897 (2006).

19   B. F. Tomandl, T. Hammen, E. Klotz, H. Ditt, B. Stemper and M. Lell, "Bone-subtraction CT angiography for the evaluation of intracranial aneurysms," Ajnr 27 (1), 55-59 (2006).

20   H. A. Gratama van Andel, H. W. Venema, G. J. Streekstra, M. van Straten, C. B. Majoie, G. J. den Heeten and C. A. Grimbergen, "Removal of bone in CT angiography by multiscale matched mask bone elimination," Med. Phys. 34 (10), 3711-3723 (2007).

21   M. Romijn, H. A. Gratama van Andel, M. A. van Walderveen, M. E. Sprengers, J. C. van Rijn, W. J. van Rooij, H. W. Venema, C. A. Grimbergen et al., "Diagnostic accuracy of CT angiography with matched mask bone elimination for detection of intracranial aneurysms: comparison with digital subtraction angiography and 3D rotational angiography," Ajnr 29 (1), 134-139 (2008).

22   C. B. Majoie, M. van Straten, H. W. Venema and G. J. den Heeten, "Multisection CT venography of the dural sinuses and cerebral veins by using matched mask bone elimination," Ajnr 25 (5), 787-791 (2004).

23   W.H Press, S.A. Teukolsky, W.T. Vetterling and B.P. Flannery, in The Art of Scientific Computing (Cambridge University, New York, 2002), pp. 413-417.

24   G. Stamm and H. D. Nagel, "[CT-expo--a novel program for dose evaluation in CT]," Rofo 174 (12), 1570-1576 (2002).

25   See EPAPS Document No. E-MPHYA6-36-035903 for a movie with MIP-images from multiple directions.,ftp//ftp.aip.org, film produced by H.A. Gratama van Andel, (released 2009).

26   D. Westra, "Binocular differentiation of radiographs (the blinking method). A method of detecting changes in the roentgen image retakes," Radiologia clinica et biologica 41 (5), 436-447 (1972).

27   A. J. van der Molen and J. Geleijns, "Overranging in multisection CT: quantification and relative contribution to dose--comparison of four 16-section CT scanners," Radiology 242 (1), 208-216 (2007).

28   P. Michotey, N.P. Moskow and G. Salamon, in Radiology of the Skull and Brain, edited by T.H. Newton and D.G. Potts (Mosby, St Louis, 1974), Vol. 2, pp. 1471–1478.

29   C. de Monye, F. Cademartiri, T. T. de Weert, D. A. Siepman, D. W. Dippel and A. van Der Lugt, "Sixteen-detector row CT angiography of carotid arteries: comparison of different volumes of contrast material with and without a bolus chaser," Radiology 237 (2), 555-562 (2005).

30   A. Waaijer, M. Prokop, B. K. Velthuis, C. J. Bakker, G. A. de Kort and M. S. van Leeuwen, "Circle of Willis at CT angiography: dose reduction and image quality--reducing tube voltage and increasing tube current settings," Radiology 242 (3), 832-839 (2007).

31   M. L. Bahner, A. Bengel, G. Brix, I. Zuna, H. U. Kauczor and S. Delorme, "Improved vascular opacification in cerebral computed tomography angiography with 80 kVp," Invest Radiol 40 (4), 229-234 (2005).

32   G. Wang, Y. Ye and H. Yu, "Approximate and exact cone-beam reconstruction with standard and non-standard spiral scanning," Physics in medicine and biology 52 (6), R1-13 (2007).

33   X. Tang, J. Hsieh, A. Hagiwara, R. A. Nilsen, J. B. Thibault and E. Drapkin, "A three-dimensional weighted cone beam filtered backprojection (CB-FBP) algorithm for image reconstruction in volumetric CT under a circular source trajectory," Physics in medicine and biology 50 (16), 3889-3905 (2005).

34   R. Manniesing, M. A. Viergever, A. van der Lugt and W. J. Niessen, "Cerebral arteries: fully automated segmentation from CT angiography--a feasibility study," Radiology 247 (3), 841-846 (2008).

35   S. O. Casey, R. A. Alberico, M. Patel, J. M. Jimenez, R. R. Ozsvath, W. M. Maguire and M. L. Taylor, "Cerebral CT venography," Radiology 198 (1), 163-170 (1996).

8
General Discussion

In this thesis a number of topics on image processing of vascular CT images have been treated. The first topic is automatic bone removal, a method that is used to aid the visualization of blood vessels in CTA. The second topic is measurement of the diameter of blood vessels in CTA images. The third topic is research into the possibility of the combination of two types of examinations, CT perfusion and CTA, into one examination. The outcomes of the studies on these topics and possible future developments are discussed.

I. BONE REMOVAL

For a better understanding of the vascular anatomy in CT angiography (CTA) or CT venography (CTV) images, maximum intensity projection (MIP) or volume rendered (VR) images are used. Before these images are made high density structures such as bone and calcifications are often removed from the 3D volume because these structures interfere with the visualization of the vessels.

Many different methods have been introduced to remove bone from CTA or CTV images. These methods can be divided into two groups: methods that use the contrast enhanced scan only and methods that need an additional scan without contrast enhancement of the vessels. With regard to the radiation dose, methods that work without an additional scan of course are to be preferred. However, it appears that these methods have considerable limitations. Because it is difficult to find the exact border between bone and contrast-enhanced vessels, the results of these techniques are not optimal, i.e. the bone removal is often incomplete or part of the vasculature is removed. In addition, they are often implemented in a semi-automatic way which makes the results subjective.

Bone removal methods that require an additional scan without contrast enhancement of the vessels are generally fully automatic and are applied increasingly. Ten years ago in our hospital a method, matched mask bone elimination (MMBE), was introduced to automatically remove voxels corresponding to bone from CTA images.[1,2] A number of modifications have been introduced. Siemens Healthcare sells an application called 'Syngo Neuro DSA CT' that implements a

method, 'bone subtraction CTA', described by Lell et al.[3,4] Main difference with the MMBE method is that, instead of using a fixed threshold to define bone in the non enhanced scan, the threshold is locally adjusted depending on the CT-values found in enhanced scan. This should help to reduce erosion of vessels adjacent to bone, while improving bone removal at places without vessels. Preliminary results of a small comparison study between the original MMBE method and the Syngo Neuro DSA CT application that we performed,[5] show that the latter method indeed produces somewhat less erosion of vessels than does MMBE, but also that it performs worse in the case of more pronounced patient movements between the non enhanced and the enhanced scan. This possibly can be explained by differences in the matching process in the two methods. Another bone removal application, SURE Subtraction, is marketed by Toshiba Medical Systems. This method actually does involve subtraction of the non enhanced scan from the enhanced scan, as opposed to the masking methods described above and the processed images are reported to contain more noise than the original CTA scan.[6] as could be expected.[2]

Bone removal is now also possible using dual energy scans made on a dual source scanner.[7] In this method the scan made at two energies is converted into an enhanced and a non-enhanced scan. In a recent comparison between the two-scan method of Lell et al [3,4] and a dual energy bone removal method, the method of Lell et al was found to be superior with respect to vessel integrity. The dual energy bone removal method provided better bone suppression in the neck, because matching in the method of Lell fails when the bone structures within the neck move relative to each other between the scans. A problem with the dual energy method was the correct differentiation of iodine and bone in high noise regions. To improve the differentiation some adhoc solution was implemented, using a vessel tracking algorithm. This algorithm, however, also showed some failures, notably the preservation of the subclavian arteries and some arteries in the neck region and is sensitive to streak artefacts as well.[8]

In this thesis chapters 2-4 deal with bone removal. In chapter 2 a method is described, multiscale MMBE, that is a modification of the original MMBE method. The main advantage of the multiscale approach over the original method is that the width of the strip of soft tissue adjacent to bone that is sacrificed in the masking process is substantially reduced (from 1.0 mm to 0.2 mm), while the quality of the

bone removal is retained or even improved. This is realized by using images with a higher resolution in the masking procedure and by subsequently blurring of the images to obtain the desired resolution and noise. In the study of chapter 2 both deconvolution and scanning with narrower collimation were used to reduce the slice thickness. With deconvolution the resolution was only improved by a modest amount. Scanning with narrow collimation with the scanner used in this study had the drawback, however, of an increased scan time. At present this drawback is less relevant as modern CT scanners have multiple narrow detector rows and can acquire sub-mm slices in very short scan times.

Chapters 3 and 4 deal with clinical evaluations of the original MMBE method. In chapter 3 the diagnostic accuracy of CTA combined with MMBE was determined for detection of intracranial aneurysms in a large patient population with clinically suspected subarachnoid hemorrhage. Digital subtraction angiography (DSA), that is considered to be the gold standard for detection of aneurysms, was used as reference standard in combination with three dimensional rotational angiography (3DRA). CTA with MMBE showed a high specificity and high sensitivity in the detection of intracranial aneurysms, although the sensitivity was limited in the detection of very small aneurysms (< 3 mm). As the rupture risk of very small additional aneurysms is extremely low, the results suggest that DSA is no longer mandatory as a diagnostic tool in patients with a good-quality CTA. Only in patients with confirmed subarachnoid hemorrhage and poor-quality CTAs, a complete diagnostic DSA should be performed. Detection of a ruptured aneurysm with CTA can be followed by selective DSA of the vessel harboring the aneurysm before endovascular treatment, thereby reducing complication risk and procedural time.

In chapter 4 the interobserver variability in the detection of cerebral venous thrombosis using CT venography with MMBE was investigated and the quality of the automatic bone removal was evaluated. The results showed that CTV with MMBE is a robust technique for visualization of the intracranial venous circulation, removing bone effectively. CTV has a high interobserver agreement for diagnosing the presence or absence of cerebral venous thrombosis.

The effectiveness of the bone removal by the original MMBE method was evaluated in both the studies of chapter 3 and 4. In chapter 3 bone removal was scored as 'complete' in 4%, 'nearly complete' as 92% and 'incomplete' in 4% of

the cases. In chapter 4 the percentages for these three classes were 76%, 24% and 0%. And so although in a very high percentage of both studies bone removal was judged to be complete or nearly complete (96% and 100%, respectively), the distribution over both categories is different in both studies. This is for a large part caused by the fact that two different versions of the MMBE software were used. For the CTA study in chapter 3 a version was used in which small high density structures, i.e. structures with a volume less than 40 mm^3, were left unmasked.[9] This was done in order to eliminate small clusters of noise from the mask, and it was thought that very small bone structures would not be present. It appeared, however, that in a number of scans such small bone structures *were* present (such as the auditory ossicles in Fig 2 of chapter 3), and this is largely responsible for the high percentage of judgment of 'incomplete removals' in chapter 3. As it appeared that corruption of the mask by noise pixels actually not was a problem, in the study of chapter 4 a new implementation of the MMBE software was used, without the elimination of noise pixels, and as a result a much higher percentage of 'complete bone removals'.

Most probably the quality of the bone removal in chapter 3 and 4 should have been higher if the multiscale MMBE method, as described in chapter 2, had been used instead of the original MMBE method. However, a comparison of both methods in these two large patient groups was not possible as in multiscale MMBE images are used that are reconstructed with a sharp reconstruction kernel. Both studies in chapter 3 and 4 were performed retrospectively and only images reconstructed with a smooth reconstruction kernel were available. Although the multiscale MMBE performed better in two patient examples of chapter 2, the additional value over the original MMBE in more extensive clinical studies has to yet be shown.

II. MEASUREMENTS OF THE VESSEL DIAMETER

In a number of clinical situations accurate and precise diameter measurements of vessels in CTA images are important. This is for instance the case when CTA is used to determine the degree of stenosis in patients that are suspected of carotid

artery occlusive disease. To measure the diameter of a blood vessel, two steps have to be taken; 1) the center lumen line (CLL) has to determined, as measurements have to be performed perpendicular to the vessel and 2) the size of the cross-section of the lumen of the vessel has to be measured. Both steps can give rise to inter- and intra-observer variations if they are performed manually. Automated methods have been introduced to reduce these variations and to facilitate the process.

In the study in chapter 5, a new method for automated center lumen line definition of vessels in CTA images, VAMPIRE, was described and compared with another automated method and with manual CLL definitions as reference standard. In comparison with the other automated method as described by Frangi and Wink, CLL definitions obtained with VAMPIRE were considerably more successful in tracing the target vessel. Less problems occurred in finding a CLL in the area of stenoses, calcifications, multiple vessels and bone structures. In comparison to manual tracing, VAMPIRE was faster but the mean deviation of the VAMPIRE tracings from the average tracings of 4 observers was larger than the deviation between the observers. The reason is that there appears to be a bias in the VAMPIRE tracings, that tends to follow the inner curve of a vessel instead of the center of the vessel, something that needs improvement. The method described in chapter 5 is limited to slabs of the volume and cannot be used for tracings in 3D. A 3D extension of the technique of chapter 5 has been published more recently.[10]

In the study in chapter 6, a model-based approach was described and tested for the measurement of the diameter of a vessel. Two features of this approach are the use of prior knowledge in the fitting of the model at the site of the stenosis, where the SNR can be low, and the applicability to both cylindrical and non-cylindrical vessels in the presence of an inhomogeneous background. The validity of this approach for diameter measurements of cylindrical arteries in CTA-images is evident from the results of measurements performed on a phantom. Accurate and precise diameter estimates were obtained from circular cross-sectional images of thin cylinders mimicking stenosed carotid sections in the neck down to a diameter of 0.4 mm. For the smallest diameters (1.5 mm and less) the use of prior knowledge was vital to avoid a dependency of the parameters that prevented the estimation of the diameters. The measurements performed in the carotid artery of two patients with non-circular cross-sections and calcifications adjacent to the stenosis, show the feasibility of the presented method and the importance of the modelling of

non-cylindrical arteries with background inhomogeneities. The accuracy of the size estimates in these patients could not be established unambiguously, because no gold standard was present. More advanced phantoms should be used in future experiments to validate the method for these situations.

The approach of chapter 6 is not yet truly 3D as it works only on cross-sectional images and assumes vessels orthogonal to the axial plane. Moreover, abrupt changes in vessel diameter are not accounted for. The direction of the vessel was assumed to be orthogonal to the axial plane, as in this situation the blurring is isotropic within the plane and can be described with one parameter. Extension of the method to 3D and to anisotropic point spread functions would allow for abrupt diameter changes and vessels in any direction. This extension to 3D is challenging, however, as there are many different shapes of the vessel lumen (and of calcifications) that the model has to be able to describe. The use of Fourier descriptors is not straightforward in 3D. A mathematical shape descriptor that might be used is the Zernike moment invariants that have been used to describe the shapes of aneurysms.[11] An extension to anisotropic point spread functions is relatively straightforward. When the anisotropy is relatively insignificant, isotropy can be obtained by preblurring, in-plane or in the z-direction.[12] Otherwise the anisotropy can be explicitly modeled.

Correct diameter measurement of a vessel in the presence of calcifications is challenging. Instead of modeling the calcification as was done in chapter 6, one could also try to remove the calcification prior to the measurements. The method from chapter 2 would not be suitable as the point spread function is not taken into account and the removal of the calcification is too coarse. A more promising approach would be the use local subtraction of calcifications in order to replace the calcification with the background intensity.[13] A slight drawback is that this approach requires an additional non enhanced scan. In the original local subtraction approach two scans were made, and these scans were matched. An exact match was difficult to obtain because of problems with the reproducibility of the calcifications in the two scans.[14] The use of dual energy techniques with a dual source scanner to subtract the calcifications possibly can solve this problem as the two scans with different energies are acquired simultaneously and no matching is required.

In chapter 6 the diameter was measured of internal carotid arteries of patients

with carotid artery occlusive disease. When the bias in the diameter measurements is not accounted for, it is most pronounced in vessels with diameters below 1 mm (see Fig. 4 in chapter 6). Diameters of normal internal carotid arteries are typically reported to be in the range of 4-6 mm. According to the NASCET criterion, patients should be treated when they have a stenosis of more than 70%, which corresponds to diameters of 1.2-1.8 mm of the stenosed internal carotid artery and in this range the bias is less severe. In applications where the vessel diameter tends to be smaller, e.g. diagnosis of coronary stenosis or diagnosis of cerebral vasospasms, application of the presented method to obtain diameter estimates without bias might have important clinical consequences.

III. CTA & CTP COMBINED

Patients that receive a CT perfusion examination almost always also receive a CTA examination of the cerebral arteries at the same time.[15,16] Individual images of a CTP examination are too noisy to use for diagnostic purposes as a CTA study. The study in chapter 7 showed that weighted averaging can be used to combine these images. The quality of the resulting images is promising, although the quality of an ordinary CTA examination was not completely reached.

The study in chapter 7 was performed on 64-slice scanner with a coverage of 4 cm. With the use of the toggling table technique [17,18] the coverage was extended to 8 cm, while reducing the sampling rate from once per 0.4 s to once per 3.5 s. With the use of more recent scanners a coverage of 16 cm is possible while maintaining a sampling rate of once per 0.4 s.[19,20] The higher coverage increases the applicability of the described method as the scan range of a regular CTA examination is approximately 12 cm. With recent scanners it is also possible to vary the time interval between scans. In that way a larger part of the images can be acquired in the maximally enhanced phase which would increase the contrast-to-noise ratio of the weighted average image for the same dose. Another useful feature would be the free choice of the mAs-value for each scan within the CTP sequence. For scans to be used both as CTP and CTA scans, an optimization of all available parameters (number and timing of images, mAs-value for each image) should be performed to

obtain the optimal trade-off between both examinations for a certain dose.

The possibility to use the time dependency of enhancement of vessels to differentiate between arteries and veins is an additional advantage of the approach of obtaining CTA images from a CTP series. Veins (or arteries) can be masked fully automatic to give a clear view on the vessels of interest. In the study of chapter 3 this would have made the manual removal of venous structures to improve the visibility of aneurysms superfluous. The automatic masking of arterial structures could have improved the interobserver variability in diagnosing venous thrombosis in the study of chapter 4 as small arteries were sometimes mistaken for veins due to arterial contamination in the CTV images.

IV. FUTURE RESEARCH

Future research in topics discussed in this thesis will be influenced by the technical development of CT scanners. The current increase in detector coverage of CT scanners with decreasing slice thickness is an development that affects all the topics.

With the increased coverage, a shift can be expected from static CTA examinations to dynamic CTA examinations. A number of advantages of dynamic images are already shown in this thesis. Differentiation will be improved between arteries, veins, soft tissue and bone, which can be helpful in the process of diagnosis. The difference between functional and anatomical imaging will decrease as both examinations can be combined into one. Further research on this topic will be necessary to find the optimal scanning technique that provides both functional and anatomical information.

Quantification of blood vessels in dynamic images will also be a challenge. In this case the time dependence enhancement of blood vessels versus the static enhancement of the surrounding tissue is a new feature that could be used in a model-based approach to obtain more accurate diameter measurements. The increased availability of four dimensional images of blood vessels will likely inspire the development of more advance segmentation and quantification methods. This will be necessary to quantify the change of vessel diameter in time

as a consequence of the beating of the heart, which is expected to be an important parameter in the diagnosis of vessel pathologies.

Differentiation between anatomical structures will also be improved by the development of dual energy techniques. At the moment different technical approaches exist to obtain dual energy images. Energy separation can be achieved with energy selective detectors, by using two X-ray sources with different energy spectra or by using a single X-ray source with fast voltage switching. As described earlier, the first results of a dual energy technique on a dual source scanner for bone removal are promising, although it is not yet clear if the quality of the bone removal will be equal to the conventional techniques for the same dose. Dual energy techniques are likely to have implications for more clinical applications than bone removal alone, such as characterization of renal stones and differentiation of fatty masses in the liver.

Ultimately all advances in technology and in image processing methods in CT will enable radiologists to make more accurate and precise diagnoses on the health status of the vascular system of their patients.

REFERENCES

1   H. W. Venema, F.J.H. Hulsmans, K.P. Van Lienden and G.J. den Heeten, "CT angiography with 0.5 mm collimation of the circle of Willis and the intracranial part of the internal carotid arteries: maximum intensity projection (MIP) with matched mask subtraction.," Radiology 213 (P), 311 (1999).

2   H. W. Venema, F. J. Hulsmans and G. J. den Heeten, "CT angiography of the circle of Willis and intracranial internal carotid arteries: maximum intensity projection with matched mask bone elimination-feasibility study," Radiology 218 (3), 893-898 (2001).

3   M. Lell, B. F. Tomandl, K. Anders, U. Baum and E. Nkenke, "Computed tomography angiography versus digital subtraction angiography in vascular mapping for planning of microsurgical reconstruction of the mandible," European Radiology 15 (8), 1514-1520 (2005).

4   B. F. Tomandl, T. Hammen, E. Klotz, H. Ditt, B. Stemper and M. Lell, "Bone-subtraction CT angiography for the evaluation of intracranial aneurysms," American Journal of Roentgenology 27 (1), 55-59 (2006).

5   H. A. F. Gratama van Andel, 2008 (unpublished).

6   E. Siebert, G. Bohner, M. Dewey, C. Bauknecht and R. Klingebiel, "Dose related, comparative evaluation of a novel bone-subtraction algorithm in 64-row cervico-cranial CT angiography," European journal of radiology (2008).

7   D. Morhard, C. Fink, A. Graser, M. F. Reiser, C. Becker and T. R. Johnson, "Cervical and cranial computed tomographic angiography with automated bone removal: dual energy computed tomography versus standard computed tomography," Investigative radiology 44 (5), 293-297 (2009).

8   M. M. Lell, M. Kramer, E. Klotz, P. Villablanca and S. G. Ruehm, "Carotid computed tomography angiography with automated bone suppression: a comparative study between dual energy and bone subtraction techniques," Investigative radiology 44 (6), 322-328 (2009).

9   M. van Straten, H. W. Venema, G. J. Streekstra, C. B. Majoie, G. J. den Heeten and C. A. Grimbergen, "Removal of bone in CT angiography of the cervical arteries by piecewise matched mask bone elimination," Medical physics 31 (10), 2924-2933 (2004).

10 Evert van Velsen, Wiro Niessen, Thomas de Weert, Cécile de Monyé, Aad van der Lugt, Erik Meijering and Rik Stokking, "Evaluation of an improved technique for lumen path definition and lumen segmentation of atherosclerotic vessels in CT angiography," European Radiology 17 (7), 1738-1745 (2007).

11 R. D. Millan, L. Dempere-Marco, J. M. Pozo, J. R. Cebral and A. F. Frangi, "Morphological characterization of intracranial aneurysms using 3-D moment invariants," IEEE transactions on medical imaging 26 (9), 1270-1282 (2007).

12 H. Bouma, J. O. Bescos, A. Vilanova and F. A. Gerritsen, in Medical Imaging 2007: Image Processing (SPIE, San Diego, CA, USA, 2007), Vol. 6512, pp. 65122N-65131N.

13 M. van Straten, H. W. Venema, G. J. Streekstra, J. A. Reekers, G. J. den Heeten and C. A. Grimbergen, "Removal of arterial wall calcifications in CT angiography by local subtraction," Medical physics 30 (5), 761-770 (2003).

14 M. van Straten, H. W. Venema, J. Hartman, G. J. den Heeten and C. A. Grimbergen, "Reproducibility of multi-slice spiral computed tomography scans: an experimental study," Medical physics 31 (10), 2785-2786 (2004).

15 W. S. Smith, H. C. Roberts, N. A. Chuang, K. C. Ong, T. J. Lee, S. C. Johnston and W. P. Dillon, "Safety and feasibility of a CT protocol for acute stroke: combined CT, CT angiography, and CT perfusion imaging in 53 consecutive patients," Ajnr 24 (4), 688-690 (2003).

16   M. Wintermark, R. Meuli, P. Browaeys, M. Reichhart, J. Bogousslavsky, P. Schnyder and P. Michel, "Comparison of CT perfusion and angiography and MRI in selecting stroke patients for acute treatment," Neurology 68 (9), 694-697 (2007).

17   H. C. Roberts, T. P. Roberts, W. S. Smith, T. J. Lee, N. J. Fischbein and W. P. Dillon, "Multisection dynamic CT perfusion for acute cerebral ischemia: the "toggling-table" technique," Ajnr 22 (6), 1077-1080 (2001).

18   S. W. Youn, J. H. Kim, Y. C. Weon, S. H. Kim, M. K. Han and H. J. Bae, "Perfusion CT of the brain using 40-mm-wide detector and toggling table technique for initial imaging of acute stroke," Ajr 191 (3), W120-126 (2008).

19   E. Siebert, G. Bohner, M. Dewey, F. Masuhr, K. T. Hoffmann, J. Mews, F. Engelken, H. C. Bauknecht et al., (2009), Vol. 82, pp. 561-570.

20   E. Siebert, G. Bohner, M. Dewey, K. T. Hoffmann, J. Mews, F. Engelken, H. C. Bauknecht, C. Diekmann et al., "Letter to the editor concerning "320-slice CT neuroimaging: initial clinical experience and image quality evaluation" (Siebert E et al: Br J Radiol 2009;82:561-70)," The British journal of radiology 82 (979), 615 (2009).

SUMMARY

With computed tomography (CT) two dimensional cross-sectional images can be made of patients. To visualize the vascular system of a patient in CT images a contrast agent is administered before the CT scan. If the CT scan is made shortly after the administration, primarily the arterial vascular system will be visualized and the examination is called CT angiography (CTA). If the CT scan is made somewhat later, primarily the venous vascular system will visualized and the examination will be called CT venography (CTV). Image processing methods can be applied to CTA or CTV images to aid the diagnosis of vascular pathologies and/or vascular diseases.

In this thesis research has been performed on image processing methods on the following topics: (1) visualization of blood vessels, (2) quantification of the diameter of blood vessels and (3) combination of images from a CT perfusion examination to obtain CTA images.

In the visualization of blood vessels with a CT angiography examination three dimensional (3D) visualization techniques such as maximum intensity projection (MIP) or volume rendering (VR) are often used. These techniques help physicians to examine a whole vascular tree faster for pathologies and to give a better insight in the 3D structure. Bone in the CTA images hampers the visualization of the vessels in MIP images as the CT value of bone will be higher than that of the enhanced vessels. As a result the bone will overlay the vessels in the MIP images. In VR images a similar problem exists. Therefore for an unhindered visualization of vessels in areas with bone, like the head and neck region, bone has to be removed from the images.

In chapter 2 a method was described that aids visualization of blood vessels by automatically removing image voxels corresponding to bone. The method is a modification of a previous method, matched mask bone elimination (MMBE). A drawback of that method is that vessels adjacent to bone may be partly masked as well. In the modified method, multiscale MMBE, this problem is reduced by using images at two scales: a higher resolution than usually is used for image processing, and the usual resolution for visualization. This multiscale approach was compared with the original one in a phantom study and in clinical CTA data. In phantom

experiments it was shown that the width of a strip of soft tissue adjacent to bone that is masked erroneously is reduced without reducing the quality of the bone removal. Clinical scans show that vessels adjacent to bone are less affected and therefore better visible.

CT angiography is increasingly used for the visualization of intracranial aneurysms. In comparison with digital subtraction angiography (DSA), which is consider as the reference standard, CTA is faster, less invasive and offers three dimensional images. To be able to replace DSA with CTA in the diagnosis of intracranial aneurysms the diagnostic accuracy of CTA should be comparable. This was investigated in chapter 3 of this thesis. 108 patients with a clinical suspicion of subarachnoid hemorrhage underwent both CTA and DSA combined with three-dimensional rotational angiography (3DRA). The CTA images were post processed with the original MMBE method. Two neuroradiologists, independently, evaluated 27 predefined vessel locations in the images for the presence of an aneurysm. After a consensus reading, diagnostic accuracy of CTA was calculated per predefined location and per patient.

In the CTA images processed with MMBE all ruptured aneurysms were detected but one (1.2 %). From the unruptured aneurysms 10 aneuryms were not detected (29%), however these aneurysms were considerably smaller (9 aneurysms < 3mm), additional to a larger ruptured aneurysms and were not the cause of the subarachnoid hemorrhage (if present). CTA aided with MMBE was found to be an accurate method in detecting ruptured intracranial aneurysms in any projection without overprojecting bone. The results suggest that, after detection of a ruptured aneurysm with CTA, DSA and 3DRA can be limited to the vessel harboring the ruptured aneurysm prior to endovascular treatment.

Computed tomography venography has proven to be a reliable imaging method in the evaluation of cerebral venous thrombosis. For better visualization of veins and sinuses, bone is often removed from the images. In chapter 4 the quality of bone removal in CTV images by the original MMBE method was assessed. Furthermore, the interobserver variability in the evaluation of cerebral venous thrombosis with CTV was investigated. Scans of fifty patients with clinical suspicion of cerebral venous thrombosis were processed and the axial source images and maximum intensity projections were retrospectively evaluated by two neuroradiologists for quality of bone removal and for the presence or absence of thrombosis in 9 dural

sinuses and 5 deep cerebral veins. CTV aided with MMBE was found to be a robust technique for visualization of the intracranial venous circulation, removing bone effectively. CTV has high interobserver agreement for presence or absence of cerebral venous thrombosis.

The second topic of this thesis is quantification of the diameter of blood vessels in CTA images. Diameter measurements of blood vessels are used in the decisions on treatment of patients for a number of diseases. Therefore accurate and precise diameter measurements are required. As manual measurements give rise to inter- and intra-observer variations and systematic errors may be present as well, there has been an interest in automatic methods. To measure the diameter of a blood vessel two steps have to be taken: a) the center lumen line (CLL) has to be estimated, as measurements have to be performed perpendicularly to the vessel and b) the size of the cross-section of the lumen of the vessel has to be measured. An automated method for CLL definition was described in chapter 5. An automated method for the second step, measuring the cross-sections, was described in chapter 6.

Automated methods for center lumen line tracing typically run into problems when dealing with vessels with abnormalities but also when dealing with bifurcations, vessels of high curvature, and other nearby vessels and bone. In chapter 5 a method, called VAMPIRE, was presented based upon a method for the tracing of neurons in microscopic images. The resulting CLL tracings were compared with manual tracings of multiple observers and with tracings of another automated method. In comparison with the other automated method, CLL definitions obtained with VAMPIRE were considerably more successful in tracing the target vessel. Less problems occurred in finding a CLL in the area of stenoses, calcifications, multiple vessels and bone structures. In comparison to manual tracing, VAMPIRE was faster. However there appeared to be a bias in the VAMPIRE tracings. They tend to follow the inner curve of a vessel instead of the center of the vessel, something that needs improvement.

Methods for the second step, measuring the diameters of blood vessels, often show a bias. Underlying this bias is the blurring of the images, which is inherent in CT imaging. One can try to remove this bias by the use of a correction procedure or by a model-based approach. Until now, these methods have been applied only to vessels with circular cross-sections. To allow for non-circular shapes of vessels a new model-based method was implemented and investigated in chapter 6. To

describe the non-circular cross-sections Fourier descriptors were used. When calcifications are adjacent to the lumen of the vessel, both the vessel and the calcifications were modeled. In addition, prior knowledge was used in the fitting of the model at the site of the stenosis, where the SNR can be low. The validity of the approach for diameter measurements in CTA-images was evident from the results of measurements performed on a phantom. Accurate and precise diameter estimates were obtained from circular cross-sectional images of thin cylinders mimicking stenosed carotid sections in the neck down to a diameter of 0.4 mm. Measurements performed in the carotid artery of two patients with non-circular cross-sections and calcifications adjacent to the stenosis, showed the feasibility of the presented method, and the importance of the modelling of non-cylindrical arteries and background inhomogeneities. The accuracy of the size estimates in these patients could not be established unambiguously, because no gold standard was present.

The last topic of this thesis is the extraction of CTA images from a CT perfusion examination. Patients that receive a CT perfusion examination almost always also receive a CTA examination of the cerebral arteries at the same time. If CTA images would be obtained from the CTP image series, the CTA examinations could be eliminated decreasing radiation dose and contrast medium load to the patient. Individual images of a CTP examination, however, are too noisy to use for diagnostic purposes as a CTA study. In chapter 7 a method for weighted averaging of the whole sequence of CTP images was described in an attempt to create CTA-like images with sufficient quality. The resulting images were compared to real CTA images.

The quality of the weighted averaged images approaches that of CTA image, although the image quality of CTA was not quite reached. Additionally, it appeared to be possible to automatically differentiate veins from arteries in the CTP images. This feature was used to automatically mask the veins in the CTA images created from the CTP-series which improved the visualization of the arteries.

LIST OF PUBLICATIONS

Parts of this thesis have also been published elsewhere. An overview of these publications is given below.

Gratama van Andel HA, van Boven LJ, van Walderveen MA, Venema HW, van Rijn JC, Stam J, Grimbergen CA, den Heeten GJ, Majoie CB.
Interobserver Variability in the Detection of Cerebral Venous Thrombosis Using CT Venography with Matched Mask Bone Elimination.
Clin Neurol Neurosurg. 2009 Nov;111(9):717-23.

Gratama van Andel HA, Venema HW, Majoie CB, Grimbergen CA, den Heeten GJ, Streekstra GJ.
Intracranial CTA obtained from a cerebral CT perfusion examination.
Med. Phys. 2009 Apr;36(4):1074-85.

Romijn M, Gratama van Andel HA, van Walderveen MA, Sprengers ME, van Rijn JC, van Rooij WJ, Venema HW, Grimbergen CA, den Heeten GJ, Majoie CB.
Diagnostic accuracy of CTA with matched mask bone elimination for detection of intracranial aneurysms: comparison with DSA and 3DRA.
AJNR Am J Neuroradiol. 2008 Jan;29(1):134-9.

Gratama van Andel HA, Venema HW, Streekstra GJ, van Straten M, Majoie CB, den Heeten GJ, Grimbergen CA.
Removal of bone in CTA by multiscale matched mask bone elimination.
Med Phys. 2007 Oct;34(10):3711-23.

Gratama van Andel HA, Meijering E, van der Lugt A, Vrooman HA, de Monyé C, Stokking R.
Evaluation of an improved technique for automated center lumen line definition in cardiovascular image data.
Eur Radiol. 2006 Feb;16(2):391-8.

BEELDBEWERKING OP HET GEBIED VAN

VASCULAIRE COMPUTED TOMOGRAPHY

Met behulp van computed tomography (CT) kunnen twee-dimensionale doorsnedebeelden van een patiënt worden gemaakt, een zogenaamde CT-scan. Om met CT het vasculaire systeem van een patiënt af te beelden wordt aan de patiënt een contrastmiddel toegediend. Kort na toediening zal voornamelijk het arteriële vaatstelsel aankleuren; het onderzoek wordt dan CT-angiografie (CTA) genoemd. Als de CT-scan iets later wordt gemaakt, dan zal het veneuze vaatstelsel het meest aankleuren; de scan wordt dan CT-venografie (CTV) genoemd. Beeldbewerkingsmethoden kunnen worden toegepast op CTA- of CTV-beelden om het diagnosticeren van vaatafwijkingen of vasculaire ziekten te vergemakkelijken.

Daarnaast wordt er ook vaak CT-perfusieonderzoek (CTP) verricht, dat bestaat uit een serie CT-scans van de hersenen na contrasttoediening. Uit variaties in de aankleuring van het hersenweefsel kunnen verschillende parameters worden bepaald die de doorbloeding van het hersenweefsel beschrijven.

In dit proefschrift zijn beeldbewerkingsmethoden ontwikkeld op de volgende gebieden: (1) het zo goed mogelijk zichtbaar maken van bloedvaten, (2) het meten van bloedvatdiameters en (3) de extractie van CT-angiografiebeelden uit een CT-perfusieonderzoek.

Bij het zichtbaar maken van bloedvaten met een CT-angiografieonderzoek kunnen drie-dimensionale (3D) visualisatietechnieken worden toegepast, zoals maximale-intensiteitsprojectie (MIP) en "volume rendering" (VR). Deze technieken helpen artsen om het vasculaire stelsel sneller te kunnen beoordelen op afwijkingen en geven een beter inzicht in de driedimensionale structuur. Bot in de CTA beelden hindert de weergave van bloedvaten in MIP-beelden omdat de CT-waarden van bot hoger zijn dan die van aangekleurde bloedvaten. Als een resultaat hiervan wordt bot overgeprojecteerd op de bloedvaten in de MIP-beelden. In VR-beelden speelt een soortgelijk probleem. Voor een goed zicht op de bloedvaten met behulp van 3D-visualisatietechnieken in gebieden met bot, zoals het hoofd-halsgebied, zal het bot verwijderd moeten worden uit de CTA-beelden.

In hoofdstuk 2 is een methode beschreven die de weergave van bloedvaten kan

verbeteren door automatisch voxels te maskeren die corresponderen met bot. De methode is een modificatie van een eerder beschreven methode, "matched mask bone elimination" (MMBE). Een nadeel van die methode is dat bloedvaten die dichtbij bot liggen ook gedeeltelijk gemaskeerd worden. In de verbeterde methode, "multiscale"- MMBE, is dit probleem gereduceerd door gebruik te maken van beelden met twee verschillende scherptes: een grotere scherpte dan gebruikelijk voor de beeldbewerking, en de gebruikelijke scherpte voor de visualisatie. Deze multiscale-aanpak is vergeleken met de originele aanpak in een fantoomstudie en in CTA-beelden van patiënten. De fantoomstudie liet zien dat structuren die naast bot lagen minder werden gemaskeerd door de nieuwe methode terwijl de kwaliteit van de botverwijdering gelijk bleef. De patiëntenbeelden toonden dat de bloedvaten in de buurt van bot minder werden aangetast door de botverwijdering en daardoor beter zichtbaar waren.

CT-angiografie wordt steeds vaker toegepast voor het afbeelden van intracraniële aneurysma's. In vergelijking met digitale subtractie-angiografie (DSA), de referentiestandaard, is CTA sneller, minder invasief en biedt driedimensionale beelden. Om DSA te kunnen vervangen in het diagnosticeren van intracraniële aneurysma's moet de diagnostische waarde van CTA vergelijkbaar zijn. Dit is onderzocht in hoofdstuk 3 van dit proefschrift. Bij 108 patiënten die werden verdacht van een subarachnoïdale bloeding werd zowel een CTA- als een DSA-onderzoek verricht. De CTA-beelden werden bewerkt met de originele MMBE-methode om het bot te verwijderen en de bloedvaten beter zichtbaar te maken. Twee neuro-radiologen evalueerden, onafhankelijk van elkaar, 27 voorgedefinieerde vaatlocaties op de aanwezigheid van een aneurysma. Na het bereiken van consensus bij onderlinge meningsverschillen werd de diagnostische waarde van CTA berekend zowel per locatie als per patiënt.

Alle gescheurde aneurysma's, op één na, werden gedetecteerd (99%). Van alle intacte aneurysma's werden er 25 van de 35 gedetecteerd (71%). De tien gemiste aneurysma's waren echter aanzienlijk kleiner (9 kleiner dan 3mm), bevonden zich naast een groter gescheurd aneurysma, en vormden niet de oorzaak van de eventueel aanwezige subarachnoïdale bloeding. CTA in combinatie met MMBE werd geschikt bevonden voor de detectie van gescheurde intracraniële aneurysma's. De resultaten suggereren dat na detectie van een gescheurd aneurysma, het gebruik van DSA tijdens de endovasculaire behandeling beperkt kan blijven tot het vat met

het gescheurde aneurysma.

CT-venografie is een betrouwbare methode om cerebrale veneuze tromboses vast te stellen. Ook in dit geval wordt vaak het bot verwijderd uit de CT-beelden om een betere afbeelding van de venen en sinussen te verkrijgen.. In hoofdstuk 4 is de kwaliteit van de botverwijdering door de originele MMBE-methode onderzocht. Bovendien is ook de variatie in de beoordeling van cerebrale veneuze tromboses tussen twee verschillende beoordelaars bekeken. Scans van 50 patiënten met een klinische verdenking op een cerebrale veneuze trombose zijn met de MMBE-methode bewerkt. De doorsnedebeelden zijn samen met maximale-intensiteitsprojectiebeelden beoordeeld door twee neuro-radiologen op de kwaliteit van de botverwijdering en de eventuele aanwezigheid van een trombose in een van de 9 durale sinussen en 5 diep gelegen venen. CTV in combinatie met MMBE bleek een robuuste techniek om de intracraniële veneuze vaten te visualiseren zonder hinder van bot. Verder bleek dat de twee beoordelaars een hoge mate van overeenstemming hadden in het vaststellen of uitsluiten van een cerebrale veneuze trombose.

Het tweede onderwerp van dit proefschrift is het meten van diameters van bloedvaten in CTA-beelden. Diametermetingen worden gebruikt in beslissingen over therapie bij verschillende vaatziekten. Accurate en precieze diametermetingen zijn daarom van belang. Omdat handmatige diametermetingen leiden tot inter- en intra-observervariaties en omdat systematische fouten aanwezig kunnen zijn, is er een groeiende belangstelling voor automatische meetmethoden. Om een bloedvatdiameter te meten, moeten er twee stappen worden gezet: a) de centrale lumenlijn (CLL) moet worden vastgesteld, omdat metingen haaks op het bloedvat moeten worden gedaan en b) de oppervlakte van de dwarsdoorsnede van het bloedvat moeten worden gemeten. Een geautomatiseerde methode voor het vaststellen van de CLL is beschreven in hoofdstuk 5. Een geautomatiseerde methode om de oppervlakte van een dwarsdoorsnede van een bloedvat te meten is beschreven in hoofdstuk 6.

Automatische methoden voor het bepalen van de centrale lumenlijn hebben vaak problemen met afwijkingen in bloedvaten, maar ook met vertakkende bloedvaten, vaten met veel bochten en vaten die dichtbij andere bloedvaten of botstructuren liggen. In hoofdstuk 5 wordt een nieuwe methode, genaamd VAMPIRE, beschreven die gebaseerd is op een methode voor het volgen van

neuronen in microscopiebeelden. De hiermee verkregen CLL-bepalingen in CTA-beelden zijn vergeleken met handmatige bepalingen van meerdere beoordelaars en met een andere automatische methode. De lijnen verkregen met VAMPIRE volgden beter de loop van het bloedvat dan de lijnen verkregen met de andere automatische methode. VAMPIRE had minder problemen om een bloedvat te volgen in gebieden met vernauwingen, verkalkingen, en dichtbijgelegen bot of andere bloedvaten. In vergelijking met de handmatige bepalingen waren de bepalingen van VAMPIRE sneller. Echter, er bleek wel een systematische fout in de lijnen van VAMPIRE aanwezig te zijn. De lijnen volgden meestal de binnenbocht van een bloedvat in plaats van het centrum van het vat, iets dat nog verbeterd zal moeten worden.

De beschreven methoden voor de tweede stap in het bepalen van de diameter van bloedvaten, namelijk het meten van de oppervlakte van de dwarsdoorsnede, hebben vaak last van een systematische fout. Onderliggende oorzaak hiervan is de inherente onscherpte van CT-beelden. Men kan deze afwijking verminderen door gebruik te maken van een correctieprocedure of door middel van een modelgebaseerde aanpak. De huidige modelgebaseerde methoden zijn alleen geschikt voor bloedvaten met een cirkelvormige doorsnede. Een nieuwe modelgebaseerde methode, die ook geschikt is voor niet-circulaire doorsnedes, is beschreven en onderzocht in hoofdstuk 6. De niet-circulaire doorsnedes zijn hierin gemodelleerd met behulp van Fourier-descriptors. Wanneer verkalkingen aanwezig zijn, worden zowel vat als verkalking gemodelleerd. Verder wordt in de methode ook gebruik gemaakt van voorkennis van modelparameters in het gebied van een vaatvernauwing, waar de signaal-ruisverhouding laag is. Dat deze aanpak werkte, bleek uit de resultaten van een fantoomexperiment. Accurate en precieze metingen konden worden verkregen van cylinders met diameters tot op 0.4 mm, die bloedvaten moesten nabootsen. Metingen aan niet-circulaire doorsnedes van bloedvaten in twee patiënten lieten zien dat deze methode voor klinische beelden geschikt was en toonden het belang van het mee-modelleren van structuren zoals verkalkingen.

Het laatste onderwerp van dit proefschrift is de extractie van CTA-beelden uit de beelden van een CT-perfusiestudie. Patiënten die een CT-perfusiestudie moeten ondergaan, krijgen vaak ook een CTA-scan van de cerebrale vaten. Als CTA-beelden uit de CT-perfusiestudie kunnen worden verkregen, zou de CTA-scan overgeslagen kunnen worden. Het voordeel hiervan is dat een patiënt zou

minder aan ioniserende straling bloot hoeft te staan en minder contrastmiddel toegediend hoeft te krijgen. Individuele beelden uit de CT-perfusiestudie hebben echter te veel ruis om te kunnen dienen als CTA-studie. In hoofdstuk 7 is een methode beschreven waarin een gewogen gemiddelde gemaakt wordt van de reeks beelden uit de CT-perfusiestudie om CTA-achtige beelden te verkrijgen van voldoende kwaliteit. Om eventuele bewegingen tijdens het onderzoek zoveel mogelijk te elimineren worden de beelden voor de middeling eerst geregistreerd. De resulterende beelden zijn vergeleken met echte CTA-beelden.

De kwaliteit van de aldus verkregen beelden benaderde die van de CTA-beelden, alhoewel de beeldkwaliteit van de CTA niet volledig werd gehaald. Verder werd een methode ontwikkeld om automatisch te differentiëren tussen arteriën en venen in de CTP-beelden. Deze methode werd gebruikt om automatisch de venen te maskeren in de gewogen gemiddelde beelden, hetgeen de zichtbaarheid van de arteriën ten goede kwam.

DANKWOORD

Het is zo ver, het proefschrift is af. Hoe is me dit eigenlijk gelukt? Het schrijven gaat me niet gemakkelijk af en het onderwerp is heel wat natuurkundiger dan mijn opleiding was. Het antwoord ligt in goede begeleiding en hulp van heel wat mensen. Hierbij wil ik iedereen bedanken die aan dit proefschrift heeft bijgedragen. Een aantal mensen wil ik in het bijzonder bedanken en noem ik hieronder.

Als eerste mijn twee dagelijkse begeleiders, Henk Venema en Geert Streekstra. Henk, van jou heb ik geleerd dat er 'geen magie bij kan zitten'. Met jouw hulp waren verrassende uitkomsten uit experimenten te verklaren en waren fouten snel gevonden. Marcel van Straten heeft het al eens gezegd, maar je bent gewoon goud waard. Geert, maar al te vaak wist jij in een concept artikel aan te wijzen waar de tekst onduidelijk werd. Ook al hadden Henk en ik een reden voor elk woord en elke bijzin, als we jou als lezer verloren, dan was het duidelijk dat we weer aan de slag moesten. Bart Carelsen heeft het al eens geschreven, met jou erbij heb je een ijzersterk team. Ik heb ook goede herinneringen aan onze reizen naar de RSNA in Chicago.

Mijn promotoren Kees Grimbergen en Ard den Heeten. De voortgangs-besprekingen met jullie brachten altijd nieuwe inspiratie en zorgden voor het nodige overzicht van het onderzoek. Kees, je las mijn artikelen altijd met grote precisie en hebt gezorgd voor de goede randvoorwaarden om onderzoek te kunnen doen. Ard, je bent altijd vol met nieuwe ideeën. Ondanks dat we de voordelen van het door jou gepropageerde 'blinking' niet hebben kunnen onderzoeken, ben ik blij dat we er een goede toepassing voor hebben gevonden in het laatste hoofdstuk. Ik wens jullie veel succes met jullie gezamenlijke onderneming in de mammografie.

Charles Majoie, als een promovendus een derde co-promoter kon hebben dan was jij dit vast bij mij geweest. Met klinische vragen kon ik altijd bij je terecht en je wilt aan alles meewerken. Ik, op mijn beurt, heb jou gelukkig ook kunnen helpen met een aantal van jouw projecten. Hoeveel projecten kan jij tegelijkertijd aan?

De promotiecommissie: Prof. dr. M.B. van Herk, Marcel bedankt voor al jouw kritische vragen tijdens de maandagochtendsessies, je hield ons scherp. Dr. ir. M. van Straten, Marcel, jouw matchings-software vormt de basis van bijna alle methoden uit dit proefschrift. Door jou heb ik een goede start kunnen maken. Prof. dr. W.J. Niessen, prof. dr. ir. L.J. van Vliet, prof. dr. J.A. Reekers en dr. F. M. Vos hartelijk dank voor jullie interesse in mijn onderzoek en dat jullie willen opponeren.

Mijn kamergenoten Remmet Jonges en Bart Carelsen. Remmet, ik mis je gezelschap en onze discussies, vooral in de ochtend. We begonnen de dag altijd vroeg samen met koffie en dan kletsten we heel wat af. Ik hoop nog eens mee te maken dat de 2D-3D (of is het toch 3D-2D?) matching klinisch gebruikt gaat worden. Bart, je hebt mijn muziekkennis (smaak?) zeker doen verbreden. We hebben veel plezier gehad, o.a. op Berder, en niet te vergeten op de borrels in Café 83. Ik wens jou, je vrouw en je kinderschare veel plezier in Amerika.

De pols-groep, Iwan Dobbe, Martijn van de Giessen, Mahyar Foumani, Simon Strackee, Natallia Dvinskikh en Shixin Song, wil ik bedanken voor alle gezelligheid. Ik was wel eens jaloers op jullie gezamenlijke project. Dat zullen jullie wel weten want ik dacht graag met jullie mee, of moet ik zeggen 'bemoeide me er tegenaan'? Ik leende jullie maar al te graag even mijn hand voor een CT, 3-DRX,of MRI scan (gelukkig niet het Cryomicrotoom!) in ruil voor de lekkere NWO-etentjes. Ik wens jullie veel succes in de afronding van jullie projecten.

De afdeling radiologie ben ik ook veel dank verschuldigd. Verscheidende mensen hebben aan studies meegewerkt door scans te beoordelen of door te adviseren. Marianne van Walderveen en Leonard van Boven; zijn jullie, net als ik, ook de tel kwijt geraakt bij de revisies van het CTV stuk? Gelukkig wint de aanhouder. Marieke Romijn, Marieke Sprengers en Jeroen van Rijn bedankt voor jullie hulp aan het aneurysma stuk. Ik ben nog steeds onder de indruk van het grote aantal patiënten (en werk) die er in zitten. René van den Berg, het spijt me dat ik niet voor elkaar heb gekregen dat je die tweede scoringsronde in Barcelona mocht doen. Ludo Beenen, je zit vol met goede ideeën, jammer dat het niet gelukt is om nog samen iets te schrijven. Sandra Ferns, Joppe Schneiders en Pim van

Ooij succes met de Heroica en Unica studies. Verder wil ik nog alle laboranten bedanken voor hun medewerking en geduld als ik de CT weer eens nodig had. Martin Poulus, Marloes Thomassen-de Graaf, Robert Jongejan, Dominique Kauffman en Anieke Eikelenboom, jullie zorgden altijd voor een leuke sfeer bij de CTs.

Ook de heren van de ICT ben ik dankbaar, Jean-Paul Geerets, Martin Schrijnders, en Jan Wolters, sorry dat ik het PACS wel eens vervuilde. Jeroen Snel wil ik bedanken voor alle hulp bij het ontwikkelen van de MMBE server en Paul Groot wil ik succes wensen met het toekomstige onderhoud.

De medewerkers van de MTO (tegenwoordig MIO) wil ik ook bedanken. Ron van Driel, Morgan Shehata en Frits de Vries, jullie hebben erg je best gedaan om mij te voorzien van de benodigde fantomen. Ik hoop dat de rust ondertussen is teruggekeerd op de werkvloer na de reorganisatie, zodat jullie weer plezier in jullie werk kunnen krijgen.

Terug naar de mensen van de afdeling Biomedical Engineering & Physics. Deze is gegroeid door de fusie met het Lasercentrum en te groot geworden om bij iedereen stil te kunnen staan. We hebben heel wat lunches, borrels en feestjes gedeeld en ik vond het erg gezellig de afgelopen jaren. Naast de verschillen tussen de aandachtsgebieden op de afdeling bestaan er ook raakvlakken. Ik heb het leuk gevonden om mee te werken aan de druk- en flowmetingen in aneurysma's. Jos Spaan en Maria Siebes, bedankt voor dit kijkje in de keuken. Ed van Bavel bedankt voor het leuke uitstapje naar Barcelona. Ik heb Arjan daar onlangs nog eens opgezocht en ik kan je aanraden om er nog meer studenten naar toe te sturen. Verder wil ik Robert Numan, Jetty Stam, René ter Wee, Pepijn van Horssen en Jeroen van den Wijngaarden nog bedanken voor de broodnodige sociale afleiding.

Wat verder weg zijn er ook mensen in Rotterdam die ik wil bedanken. Tijdens mijn afstudeeronderzoek heb ik begeleiding gehad van Rik Stokking, Erik Meijering, Aad van der Lugt en Cecile de Monyé. Ik vind het leuk dat ons artikel over VAMPIRE zo goed in dit proefschrift past. Iemand die ik hier ook wil noemen is Karin Bol, ik heb jou mogen begeleiden tijdens je stage in het AMC. Ik wens je veel succes met je promotieonderzoek in Rotterdam.

Even further away there are some more people that I would like to thank. Alejandro Frangi, Arjan Geers, Catalina Tobon-Gomez and Hrvoje Bogunovic, I enjoyed visiting you in Barcelona and working with you. Luca Antiga, thank you very much for your software en your quick response on emails.

Vanaf mijn studie Medische Informatiekunde heb ik heel wat jaren in het AMC mogen rondlopen. Het was leuk om als promovendus onderwijs te mogen geven. Ik wens de MIK nog heel wat jaren en (meer) studenten toe. Twee docenten wil ik in het bijzonder nog noemen, Baas Louter en Oscar Estévez, bedankt voor jullie enthousiaste onderwijs en jullie interesse tijdens mijn promotie onderzoek.

Mijn vrienden Bart van der Zanden, Remko van der Togt en Marion Verduijn wil ook bedanken. Een goede vriendschap, dezelfde studie, allemaal in het onderzoek, maar wel andere richtingen, bijzonder! Bart en Remko, leuk dat jullie mijn paranimfen willen zijn.

Als laatste wil ik ook mijn familie en schoonfamilie bedanken voor alle steun en interesse. Anna en Britta, ik bof maar met jullie!

CURRICULUM VITAE

Hugo was born on August the 20th 1980 in Boskoop. The first three years of primary school were followed at the Vijverfluiter school and the last five years at the Koningin Wilhelmina school. At the age of twelve he moved to Alphen aan den Rijn. There he attended secondary school at the Groene Hart Lyceum and obtained his athenaeum diploma.

He studied medical informatics at the University of Amsterdam. In the years 1999 and 2001 he was elected in the student council of the Faculty of Medicine. A scientific training was performed at the Biomedical Imaging Group Rotterdam at the Erasmus MC under supervision of Rik Stokking. The subject was automated center lumen line definition of vessels in CT angiography images. In February 2004 he graduated *cum laude* in Amsterdam. For six months he worked as a research assistant at the department of Surgery in the Academic Medical Center in Amsterdam. In September 2004 Hugo became a PhD student under the supervision of Kees Grimbergen, Ard den Heeten, Henk Venema and Geert Streekstra at the department of Biomedical Engineering & Physics (previously called Medical Physics). In June 2009 he started as development engineer at MILabs in Utrecht where he is working on software for a micro-CT and micro-SPECT scanner.